Charge Carrier Trapping Processes and Deliberate Design of Afterglow Phosphors

Luo, Hongde

Important note
To cite this publication, please use the final published version (if applicable).
Please check the document version above.

Charge Carrier Trapping Processes and Deliberate Design of Afterglow Phosphors

Charge Carrier Trapping Processes and Deliberate Design of Afterglow Phosphors

Proefschrift

ter verkrijging van de graad van doctor
aan de Technische Universiteit Delft,
op gezag van de Rector Magnificus prof. ir. K.C.A.M. Luyben,
voorzitter van het College voor Promoties,
in het openbaar te verdedigen op
donderdag 19 oktober 2017 om 15:00 uur

door

Hongde LUO

Master of Science in Engineering, Shanghai Normal University,
geboren te Shanghai, China.

Dit proefschrift is goedgekeurd door de promotor:
Prof. dr. P. Dorenbos

Samenstelling promotiecommissie:
Rector Magnificus,   voorzitter
Prof. dr. P. Dorenbos,   Technische Universiteit Delft, Promotor

Onafhankelijke leden:
Prof. dr. P. Smet   Universiteit Gent
Prof. dr. C. Pappas   Technische Universiteit Delft
Prof. dr. H.T.J.M. Wolterbeek   Technische Universiteit Delft
Prof. dr. J. Wallinga   Universiteit Wageningen
Dr. H.T.J.M. Hintzen   Technische Universiteit Delft
Dr. A.J.J. Bos   Technische Universiteit Delft, overig lid

Dedicated to my parents and girlfriend Miss. Ren

致父母与女朋友任小姐

Table of Contents

1

Introduction

1.1 Introduction to afterglow

The aim of this thesis is to understand and control the trapping and detrapping processes of charge carries in afterglow phosphors in order to reach our goal of "deliberate design" of afterglow phosphors.

Afterglow, also called persistent luminescence or long-lasting phosphorescence, is a phenomenon whereby luminescence can last for a certain period of time (from seconds to hours) after the stoppage of the excitation[1].

An afterglow phosphor is an inorganic material that contains charge carrier recombination (luminescence) center(s) and trapping center(s). The material can be an ionic insulator or a wide-bandgap semiconductor consisting of cations and anions arranged in a periodic lattice. The recombination center, also called the luminescence center or activator, is where electrons and holes recombine and produce luminescence. The trapping center is a defect where charge carries can be trapped for a period of time and then be released.

The earliest record of using an afterglow material dates back to the Song dynasty of China (976-1279 A.D.)[2-3]. At that time, a monk called Wen-Yin recorded a story in his miscellaneous book *Xiang-Shan Ye-Lu* about a luminous painting from the period 140-88 B.C. In the painting there was a cow that was eating grass outside the pen during the daytime. At night, a glow-in-the-dark cow appeared that was resting in the pen[4]. Possibly, the ink used was the first man-made persistent luminescence material.

The earliest western record of such glow-in-the-dark material dates from 1603. The Italian shoemaker and alchemist Vincenzo Cascariolo found a barite stone ($BaSO_4$) from the outskirts of Bologna that emitted red light in the dark without any external excitation source after sintering under reducing condition[2-3]. In 1764, the British mixed sulphur with oyster and fired it to get a blueish-white emitting afterglow material[3]. It is still not clear which ions (luminescence centers) contribute to the afterglow in the above two materials but the host lattices were BaS and CaS, respectively.

In the 20th century, ZnS was synthesised and became one of the most important host lattices for luminescent materials[2]. Copper and radium were co-doped into ZnS to make a green luminous painting material, in which Cu^{2+} is the luminescence center and Ra co-dopant produces ionization radiation that excites Cu^{2+}. However, due to the radioactivity of radium, serious health issues occurred at that time and the most tragic story is that of the "radium girls"[5-6]. These ladies worked at a production line in the United States Radium factory in Orange, New Jersey, around 1917, and were told that the paints were safe and they ingested deadly amount of radium by licking of the paintbrush to keep it sharp. Later, the radium was replaced by the less harmful, but still radioactive tritium or promethium.

In August 1996, Matsuzawa developed $SrAl_2O_4:Eu^{2+},Dy^{3+}$ with higher brightness, significantly longer glow time and no radioactive elements that opened a new door for afterglow research[7]. Since then, dozens of afterglow materials were synthesized that show emission in different colors, for instance: $CaAl_2O_4:Eu^{2+},Dy^{3+}$ (blue)[8], $Sr_2SiO_4:Eu^{2+},Dy^{3+}$ (green)[9], $Y_2O_2S:Ti^{4+},Mg^{2+}$ (orange)[4], $Sr_2Si_5N_8:Eu^{2+},Tm^{3+}$ (red)[10], and $Zn_3Ga_2Ge_2O_{10}:Cr^{3+}$ (NIR)[11].
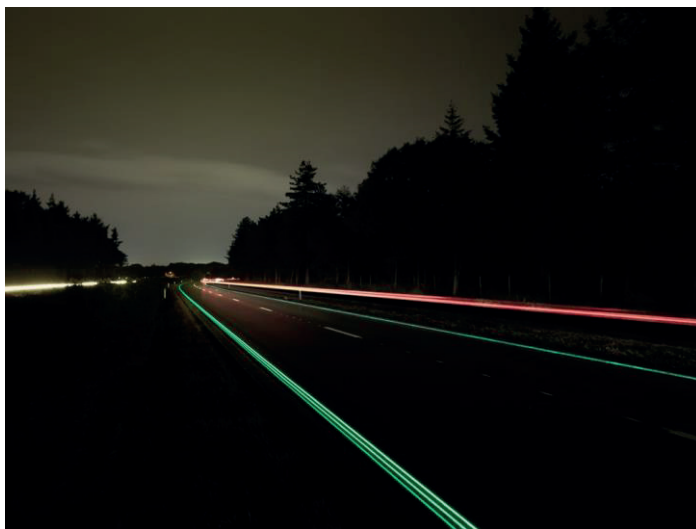
Figure 1.1. The glow-in-the-dark highway (N329) in the Netherlands. The figure is from Ref.12

The classical applications of afterglow phosphors are decorations, toys, safety signage, watch dials and displays. Recently, a 500 meter stretch of a highway (N329) near Amsterdam in the Netherlands was coated with green afterglow phosphors on the strips that illuminate the edges of the road[12]. This is the world's first glow-in-the-dark highway (see Figure 1.1). Another new afterglow application is in bio-labels for tracing cancer cells, since the near-infrared (NIR) afterglow materials emit in the biologically transparent window that significantly increases the signal-to-noise ratio and decreases photon-induced deterioration of analytes[13].

1.2 Fundamentals of afterglow phosphors

Afterglow phosphors contain defects that can capture charge carriers. The location of these defect levels in the forbidden gap is crucial to the afterglow properties since neither a too shallow nor a too deep trap will produce room temperature afterglow. In this thesis, we use the vacuum referred binding energy (VRBE) level diagram constructed from the semi-empirical chemical shift model[14-15] as a tool to investigate these metastable defect levels, which will be discussed in detail in the following section.

1.2.1 The vacuum referred binding energy level (VRBE) diagram

The vacuum referred binding energy (VRBE) is defined as the energy needed to extract an electron from a system and to bring it to the vacuum. The energy of an electron at rest in vacuum is defined as energy zero. This electron can be either from a host band state or from an impurity ground or excited state[14-15].

The aim for developing the VRBE diagram is to construct a diagram where the binding energy of an electron in lanthanide defect states and in the host valence band (VB) and conduction band (CB) states can be compared with respect to one and the same energy reference. Usually, like in XPS (X-ray photoelectron spectroscopy) and UPS (ultraviolet photoelectron spectroscopy) studies and in *ab initio* and first-principles calculations, energies are referred to the top of the VB which is then set as the zero of energy[16-17]. However, with such approach one cannot relate the binding energies in different compounds to a common reference of energy. There are only a few solutions to this problem. In the field of semiconductor science the valence band offset at the hetero-junction of two compounds can be determined[18-19]. In the field of electrochemistry, valence band energies can be related to the standard hydrogen potential[20-21]. In the field of

luminescence science, the chemical shift model was developed in 2012 to construct a vacuum referred binding energy (VRBE) diagram. Further details about the VRBE diagram can be found in Refs. 14 and 15.

In Figure 1.2 the VRBE diagram of the lanthanides in $SrAl_2O_4$ is provided as an example. At temperature lower than 923 K, $SrAl_2O_4$ crystallizes in a monoclinic structure (space group $P2_1$) that contains two nine fold coordinated Sr sites[22]. In constructing the scheme here we ignore the lanthanides site occupancy and we assume that the VRBE of doped lanthanides in different Sr sites are the same. However, one should be aware that the lanthanides VRBE levels at different sites might be at slightly different energies.
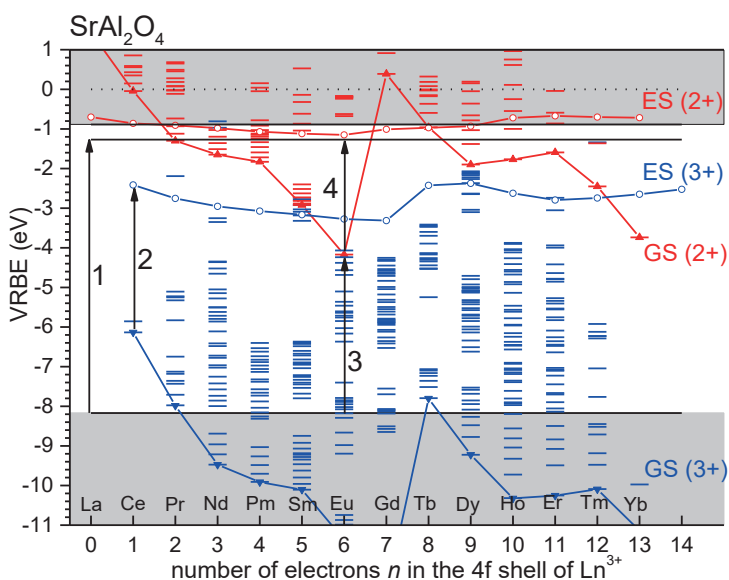
Figure 1.2. The VRBE diagram for $SrAl_2O_4$. Arrow 1 shows the the host exciton creation energy (E^{ex}). Arrow 2 is the 4f to $5d_1$ electron transitions in trivalent Ce. Arrow 3 indicates the charge transfer from O^{2-} to Eu^{3+}. Arrow 4 is the 4f to $5d_1$ electron transitions in divalent Eu. The horizontal bars represented the excited $4f^n$ levels from the Dieke diagram.

The zigzag curves labelled GS (3+) and GS (2+) connect the binding energies in the lowest $4f^n$ levels of the trivalent and the divalent lanthanides, respectively. The curve labelled ES (3+) and ES (2+) connect the binding energies in the $5d_1$ excited state of the trivalent and divalent lanthanides.

Arrow 1 shows the host exciton creation energy (E^{ex}). This energy can be determined from photoluminescence excitation (PLE) or diffuse reflection spectra (DRS) of the host lattice, which is around 6.9 eV[23]. The mobility band gap E_{VC}, or the energy between the bottom of CB and the top of VB, can be obtained from the host exciton creation energy by adding the exciton binding energy. For wide band gap compounds the exciton binding energy is estimated around 8% of the exciton creation energy.

Arrow 2 shows the 4f to $5d_1$ electron transitions in trivalent Ce. It means the energy needed to bring an electron from Ce^{3+} 4f ground state ($^2F_{5/2}$) to its first 5d excited state ($5d_1$). This energy can be determined from the photoluminescence excitation spectra, or diffuse reflection spectra, or first-principles calculation. In $SrAl_2O_4:Ce^{3+}$, the five 4f-$5d_i$ (i=1 to 5) transitions are all reported and the values are shown in Ref.22. With this information all the levels for the trivalent lanthanides can be drawn in the scheme.

Arrow 3 indicates the charge transfer (CT) from VB to Eu^{3+}, which is 4.0 eV (310 nm)[24]. During CT-band excitation electrons are excited from the VB to the Eu^{3+}, forming Eu^{2+} $4f^7(^8S_{7/2})$ ground state above the top of the VB. The VRBE of an electron in the Eu^{2+} $4f^7(^8S_{7/2})$ ground state obeys within the chemical shift model as the following equation[14]:

$$E_{4f}(7, 2+, A) = -24.92 + \frac{18.05 - U(6,A)}{0.777 - 0.0353U(6,A)} \qquad 1.1$$

where E_{4f} (7, 2+, A) stands for the VRBE in the Eu^{2+} ground state in a host lattice (A) and U(6, A) is the Coulomb repulsion energy for Eu. It means the energy difference between the ground state energy of Eu^{2+} and Eu^{3+}, which can be estimated by an empirical equation[25-26]:

$$U(6, A) = 5.44 + 2.834e^{-\epsilon_c(1,3+,A)/2.2} \qquad 1.2$$

where ϵ_c (1, 3+, A) represents the 5d centroid shift for Ce^{3+} in a host lattice. The centroid shift is defined as the lowering of the average energy of the Ce^{3+} 4f-5d transitions relative to the value for Ce^{3+} as a free ion (6.35 eV) [26]. Adopting the earlier mentioned Ce^{3+} 4f-$5d_{1-5}$ transition energies, the U(6,A) is calculated as 7.2 eV. From Eq. 1.1, $E_{4f}(7,2+,A)$ is fixed as -4.17 eV. Adopting the Eu^{3+} CT energy

6

and the host exciton creation energy, the VB maximum and CB minimum can be obtained.

Arrow 4 shows the electron transition from the Eu^{2+} 4f ground state to the $5d_1$ excited state. The energy difference (ΔE) between the Eu^{2+} $5d_1$ excited state and the CB bottom can be verified by fitting with the following equation through the data from the thermal quenching curve, the decay curve or photoconductivity curve as a function of temperature[27,28]:

$$I(T) = \frac{I(0)}{1 + C\exp(-\frac{\Delta E}{kT})} \qquad 1.3$$

Where *I(T)* and *I(0)* is the intensity at temperature T and the lowest temperature where the luminescence intensity is the maximum, *k* is the Boltzmann constant and *E* is called the activation energy, which is defined as the energy needed to active the thermal quenching. However, one should notice that there are two different ways of the thermal quenching process: *via* thermal ionziation to the CB or *via* the crossing point in the configuration coordinate diagram. In the case of quenching *via* thermal ionziation to the CB, this energy should be similar to the energy difference between the $5d_1$ level and the CB minimum. With this information, the divalent europium and the rest of divalent lanthanides $5d_1$ excited states can be confirmed in the diagram.

1.2.2 Electron trapping and electron release
We will use $SrAl_2O_4:Eu^{2+},Dy^{3+}$ as an example to illustrate the electron trapping and detrapping processes in the afterglow materials, as shown in Figure 1.3.

One observes from Figure 1.3 that after excitation the Eu^{2+} $5d_1$ excited state is close to but below the CB, which indicates that the electrons in the excited states can transfer to the CB at room temperature by thermal activation (Arrow 1). This phenomenon is called thermal ionization that contributes to the thermal quenching of Eu^{2+} or Ce^{3+} in luminescent materials[29-31]. The thermal ionization process was also confirmed recently by EXAFS measurements which showed that the concentration of trivalent europium increases after exposing the sample to UV light[32]. The released electrons move freely in the CB (Arrow 2) and will be captured by the electron-trapping center (Arrow 3) although the nature of the trap is still under debate. The trapped electrons are released slowly at room temperature

and recombine with Eu^{3+} and eventually generate Eu^{2+} emission centered at ~520 nm.
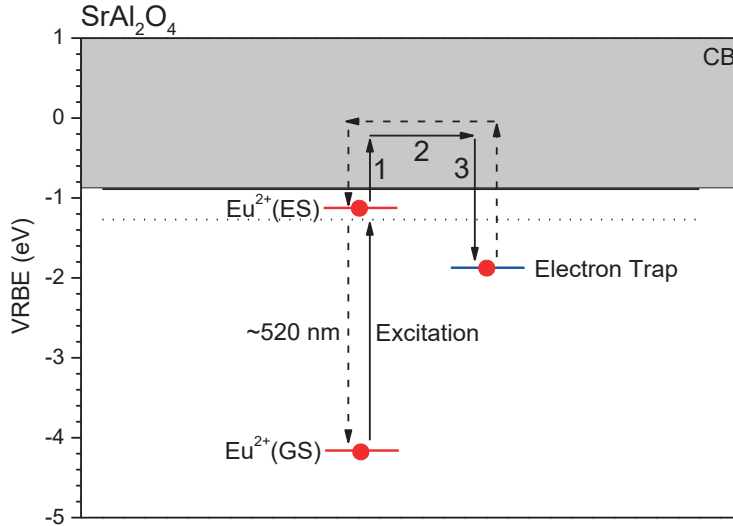
Figure 1.3. Illustration of the electron trapping (solid arrows) and detrapping (dashed arrows) processes in $SrAl_2O_4:Eu^{2+},Dy^{3+}$. The filled circles stand for electrons.

Another example is a blue-emitting afterglow phosphor: $CaAl_2O_4:Eu^{2+},Nd^{3+}$. By means of measuring thermoluminescence excitation (TLE) spectra, it was found that the TLE spectrum is very similar to the photoluminescence excitation spectrum. This means that the excitation of the 5d states of Eu^{2+} leads to electron release and electron-trapping[33]. The trapping centers in this case are attributed in Ref.34 to both oxygen vacancy (V_O^{2+}) and Nd^{3+} [34].

The type of electron-trapping center can be controlled by lanthanide co-doping. When the divalent lanthanide $4f^n$ ground state levels are below the CB the corresponding trivalent ions may act as electron-trapping centers and as function of type of lanthanide codopant there is a predictable variation in trap depth as given by the zigzag curve GS2+ in Figure 1.2.

This hypothesis was proposed by Dorenbos in 2005[35] and later it was experimentally confirmed by thermoluminescence (TL) studies of $YPO_4:Ce^{3+}$, Ln^{3+} (Ln = Pr, Nd, Sm, Dy, Ho, Er, Tm, and Yb) by Bos et al[36]. Here, Ce^{3+} acts as the hole-trapping center and the recombination (luminescence) center while the

selected lanthanide codopants are the electron-trapping centers that trap electrons during β-irradiation. During the TL readout, the trapped electrons are released and move freely in the CB to eventually recombine at Ce^{4+} to produce Ce^{3+} 5d-4f emission. Different lanthanide codopants have different TL glow peak maxima indicating different trap depth. In Figure 1.4 the glow peak maxima from thermoluminescence measurements are compared with the VRBE diagram prediction. The model predicts that Pr^{2+} has the shallowest trap depth while Eu^{2+} has the deepest trap depth. The glow peaks of the other Ln^{2+} ions also coincide with the VRBE prediction[36]. The trap depth in this case is the distance between divalent lanthanide ground state levels and the bottom of the CB.

The same phenomenon has been reported later in $Y_3Al_5O_{12}$: Ln^{3+},RE^{3+} (Ln= Ce^{3+}, Pr^{3+} and Tb^{3+}; RE= Eu^{3+} and Yb^{3+})[37], $Sr_3Al_xSi_{1-x}O_5$:Ce^{3+}, Ln^{3+} (Ln = Er, Nd, Sm, Dy and Tm)[38], and $GdAlO_3$:Ce^{3+}, Ln^{3+} (Ln= Pr, Er, Nd, Ho, Dy and Tm)[39]. The latter two will be discussed in detail in Chapter 3 and Chapter 5.
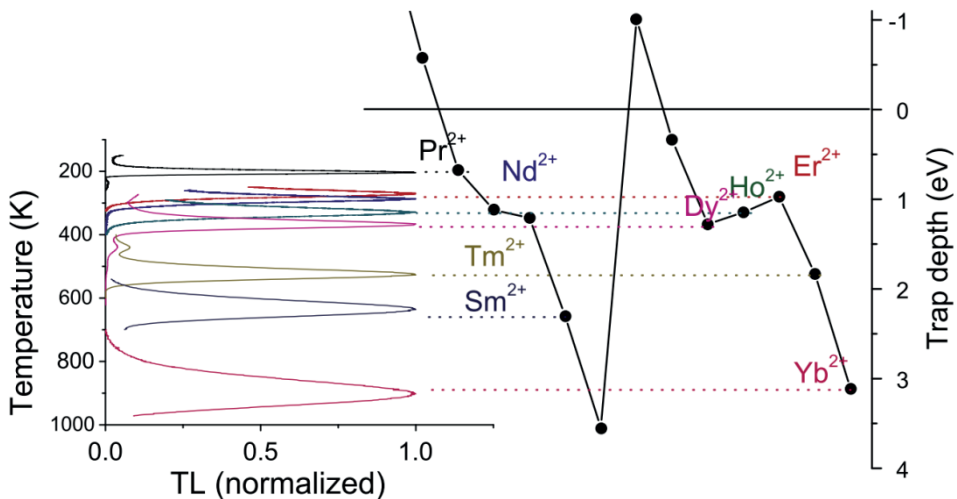
Figure 1.4. Comparison of predictions of the trap depth of the VRBE diagram and thermoluminescence measurements of YPO_4:Ce^{3+}, Ln^{3+}. The figure is taken from Ref. 36.

Another electron detrapping process is the quantum tunnelling recombination. In this situation, the trapped electrons do not recombine by thermal excitation to the CB but by a localized tunnelling process, which may occur between the traps and near excited state levels of the recombination centers. This is an attractive

alternative for afterglow research since the glow intensity is much less sensitive to the environment temperature, for instance, in the hot summer and the cold winter. The tunneling model is used to explain the Cr^{3+} afterglow mechanism in $Zn_3Ga_2Ge_2O_{10}$[11]. For lanthanides, it was investigated by Dobrowolska *et al*[40] in $YPO_4:Ce^{3+},Ln^{3+}$.

1.2.3 Hole trapping and hole release

Figure 1.5 illustrates the hole trapping process. When the charge carrier is created by the external radiation, the hole may be captured in a hole trapping center while the electron may be trapped in an electron trapping center. The holes can transport *via* the VB or as a migrating Vk center (a hole shared between two anions) just above the VB. When the thermal energy to release a trapped hole is less than to release a trapped electron ($E_1 < E_2$), the trapped hole will be released earlier than the electron and recombine in the electron trapping center and show luminescence.
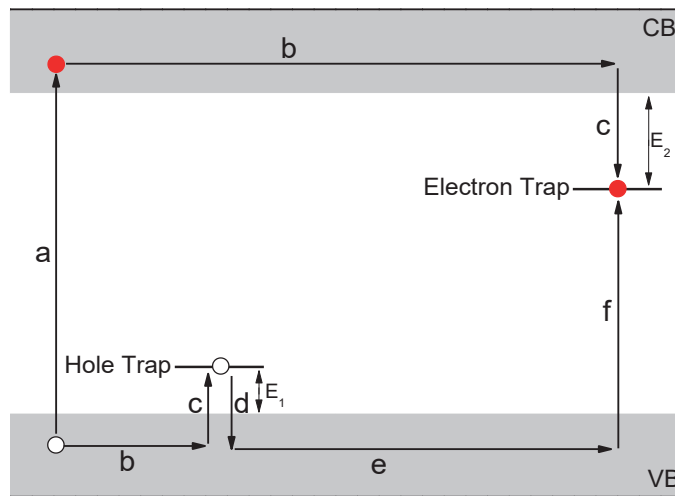
Figure 1.5. Illustration of the hole trapping and detrapping process: (a) charge carrier generation; (b) charge carrier transport; (c) charge carrier trapping; (d) hole release; (e) hole transport; (f) hole-electron recombination. The filled circles stand for electrons and the open circles stand for holes.

When the trivalent lanthanide 4f ground state levels are close above the VB (see GS3+ zigzag in Figure 1.2), these ions may act as hole-trapping centers.

10

Compared to the many reports on electron trapping and detrapping processes, there are much fewer reports that discuss hole trapping and detrapping processes. One of the few is by Chakrabarti et al in the 1980s who found that during UV irradiation of $MgS:Ce^{3+}$, Sm^{3+} the holes are captured by cerium and electrons by samarium. After hole release, they recombine with samarium producing Sm^{3+} characteristic emission during the TL readout[41]. The other example of hole detrapping was proposed by Bos et al. in $YPO_4:Tb^{3+}$, RE^{3+} (RE^{3+} = Nd, Ho and Dy) where Tb^{3+} is acting as a hole-trapping center and RE^{3+} as electron tapping center[36].

In Chapter 5, we will report other evidence that holes can be trapped in a lanthanide hole trapping center and then be released by studying the thermoluminescence of $GdAlO_3:Ln^{3+},RE^{3+}$ (Ln=Sm, Eu and Yb, RE= Ce, Pr and Tb). In this case, Sm^{3+}, Eu^{3+} and Yb^{3+} act as recombination centers, while Ce^{3+}, Pr^{3+} and Tb^{3+} act as hole-trapping centers. The trapped holes are released from Pr^{4+} or Tb^{4+} and recombine with the trapped electrons on Sm^{2+}, Eu^{2+} or Yb^{2+} and yield characteristic trivalent emission from Sm^{3+}, Eu^{3+} or Yb^{3+} at ~600 nm, ~617 nm or ~980 nm, respectively. The trap depth in this case is the distance between trivalent lanthanide ground state 4f levels and the top of the VB.

We will also confirm the hole trapping model in Chapter 6, where we studied the charge carrier trapping processes in RE_2O_2S (RE=La, Gd, Y and Lu) and revealed that the afterglow mechanism of $Y_2O_2S: Ti^{4+},Eu^{3+}$ is due to hole release from the host related hole-trapping centers. The released holes recombine with the trapped electrons on Ti^{3+} and Eu^{2+} to yield broad Ti^{4+} yellow-red charge transfer (CT) emission and characteristic Eu^{3+} 4f-4f emission.

1.2.4 Trap depth engineering
The trap depth can be controlled not only by selecting different lanthanide codopants but also by the bandgap engineering approach.

The electron trap depth can be adjusted by tailoring the VRBE of the CB bottom. One example is reported by Zhuang et al in $Zn(Ga_{1-x}Al_x)_2O_4:0.02Cr^{3+}$ near-infrared afterglow phosphor[44]. With substitution of Ga by Al (up to 0.04), the bottom of the CB moves up and shifts the TL glow curve to a higher temperature. Another example is from Ueda et at in $Y_3Al_{5-x}Ga_xO_{12}:Ce^{3+},Cr^{3+}$, where Ce^{3+} is the recombination center and Cr^{3+} is the electron-trapping center. By increasing the

content of Ga, the VRBE of the trapped electron in Cr^{2+} remains almost the same position while the bottom of the CB moves downwards, leading to TL glow curve shifts towards lower temperature[45].

Similarly, the hole trap depth can be adjusted by tailoring the VRBE of the VB top, which will be presented in Chapter 5. By increasing the content of lanthanum in $Gd_{1-x}La_xAlO_3$:Eu^{3+},Pr^{3+}/Tb^{3+}, the top of the VB moves upwards while the VRBE of the trapped hole in Tb^{4+} or Pr^{4+} remains almost the same. Therefore, the trap depth related to Pr or Tb decreases and the TL glow curve shifts to the lower temperature.

1.3 Outline

In Chapter 2, we will overview and explain the experimental techniques used.

In Chapter 3, we developed a UV excited yellow-emitting afterglow phosphor $Sr_{2.98}Al_{0.02}Si_{0.98}O_5$:$Ce^{3+}$,$Dy^{3+}$. The TL results confirm that Ce^{3+} is the recombination center and the lanthanide co-dopants like Er, Nd, Sm, Dy and Tm act as electron traps with different trap depths. The TLE spectrum reveals that the afterglow phosphor can only be charged by the near and deep UV excitation since the Ce^{3+} $5d_1$ excited state is too far below the CB which can be confirmed by the VRBE diagram.

In Chapter 4, we initially intended to develop an afterglow phosphor: $(Sr, Ca)_3(Y, Lu)_2Ge_3O_{12}$:$Ce^{3+}$,$Ln^{3+}$ with Ce^{3+} as the luminescence center and other trivalent lanthanides as electron-trapping centers since Ce^{3+} in garnet compounds emit in the green to red and have strong absorption of day light. However, it was found that this material turns out not to be a good persistent luminescence phosphor. To explain this we determined the electronic structure providing the location of the lanthanide levels within the bandgap by a combination of spectroscopy, first-principles calculation and the semi-empirical chemical shift model.

In Chapter 5, we studied the trapping and detrapping processes of charge carries in $GdAlO_3$. We found cerium is the recombination center and lanthanide co-dopants act as electron-trapping centers in $GdAlO_3$:Ce^{3+},Ln^{3+} (Ln= Pr, Er, Nd, Ho, Dy, Tm, Eu and Yb). Different lanthanide co-dopants generate different trap depths. We also found that Sm^{3+}, Eu^{3+} and Yb^{3+} act as recombination centers, while Ce^{3+}, Pr^{3+} and Tb^{3+} act as hole-trapping centers in $GdAlO_3$: Ln^{3+},RE^{3+} (Ln=Sm, Eu and Yb,

RE= Ce, Pr and Tb). The trapped holes are released from Pr^{4+} or Tb^{4+} and recombine with the trapped electrons on Sm^{2+}, Eu^{2+} or Yb^{2+} and yield characteristic trivalent emission from Sm^{3+}, Eu^{3+} or Yb^{3+} at ~600 nm, ~617 nm or ~980 nm, respectively. In the end, we used lanthanum to replace gadolinium to engineer the VB energy and change the hole trap depth in $Gd_{1-x}La_xAlO_3:Eu^{3+},Pr^{3+}$ and $Gd_{1-x}La_xAlO_3:Eu^{3+},Tb^{3+}$. The results show that the VB moves upwards and the trap depth related to Pr^{3+} or Tb^{3+} decreases.

In Chapter 6, based on the results of Chapter 5, we suspected that the afterglow mechanism of the red-emitting afterglow phosphor $Y_2O_2S:Eu^{3+},Ti^{4+}$ is based on the hole trapping and hole release model instead of the more common electron model shown in Chapter 3 and 4.

Therefore, in this chapter, we studied the charge carrier trapping processes in the RE_2O_2S (RE=La, Gd, Y and Lu) system by single doping with different lanthanides and titanium. For these dopants we found evidence that recombination is by means of hole release instead of electron release. The released holes recombine with the trapped electrons on Ti^{3+} and Eu^{2+} and yield broad Ti^{4+} yellow-red charge transfer (CT) emission and characteristic Eu^{3+} 4f-4f emission.

1.4 Reference

1. Van den Eeckhout, K.; Smet, P. F.; Poelman, D., Persistent Luminescence in Eu2+ Doped Compounds a Review. *Materials* **2010**, *3*, 2536-2566.

2. Smet, P. F.; Moreels, I.; Hens, Z.; Poelman, D., Luminescence in Sulfides: A Rich History and a Bright Future. *Materials* **2010**, *3*, 2834-2883.

3. Harvey, E. N., *A History of Luminescence from the Earliest Times until 1900*; American Philosophical Society, 1957; Vol. 44.

4. Kang, C.-C.; Liu, R.-S.; Chang, J.-C.; Lee, B.-J., Synthesis and Luminescent Properties of a New Yellowish-Orange Afterglow Phosphor Y2O2S:Ti,Mg. *Chemistry of Materials* **2003**, *15*, 3966-3968.

5. Wikipedia.Radium Girls. https://en.wikipedia.org/w/index.php?title=Radium_Girls&oldid=766100626.

6. Van den Eeckhout, K. Persistent Luminescence: Kinetics and Compounds. Ghent University, 2013.

7. Matsuzawa, T., A New Long Phosphorescent Phosphor with High Brightness, SrAl2O4:Eu2+, Dy3+, *Journal of Electrochem Society* **1996**, *143*, 2670-2683.

8. Hölsä, J.; Jungner, H.; Lastusaari, M.; Niittykoski, J., Persistent Luminescence of Eu2+ Doped Alkaline Earth Aluminates, MAl2O4:Eu2+. *Journal of Alloys and Compounds* **2001**, *323*, 326-330.

9. Lakshminarasimhan, N.; Varadaraju, U., Luminescence and Afterglow in Sr2SiO4: Eu2+, RE3+ [Re= Ce, Nd, Sm and Dy] Phosphors—Role of Co-Dopants in Search for Afterglow. *Materials Research Bulletin* **2008**, *43*, 2946-2953.

10. Li, Y. Q.; van Steen, J. E. J.; van Krevel, J. W. H.; Botty, G.; Delsing, A. C. A.; Disalvo, F. J.; de With, G.; Hintzen, H. T., Luminescence Properties of Red-Emitting M2Si5N8:Eu2+ (M = Ca, Sr, Ba) Led Conversion Phosphors. *Journal of Alloys and Compounds* **2006**, *417*, 273-279.

11. Pan, Z.; Lu, Y.-Y.; Liu, F., Sunlight-Activated Long-Persistent Luminescence in the near-Infrared from Cr3+-Doped Zinc Gallogermanates. *Nature Materials* **2012**, *11*, 58-63.

12. Stinson, L. Awesome Glowing Roads That Could Be the Highways of the Future. Https://www.wired.com/2014/11/awesome-glowing-roads-highways-future/.

13. Li, Y.; Gecevicius, M.; Qiu, J., Long Persistent Phosphors-from Fundamentals to Applications. *Chemical Society Reviews* **, 2016**,*45*, 2090-2136

14. Dorenbos, P., Modeling the Chemical Shift of Lanthanide 4f Electron Binding Energies. *Physical Review B* **2012**, *85*,16510701-16510710

15. P.Dorenbos, A Review on How Lanthanide Impurity Levels Change with Chemistry and Structure of Inorganic Compounds. *ECS Journal of Solid State Science and Technology* **2013**, 3001-3011

16. Huang, B., Native Point Defects in Cas: Focus on Intrinsic Defects and Rare Earth Ion Dopant Levels for up-Converted Persistent Luminescence. *Inorganic Chemistry* **2015**.*54*, 11423–11440

17. De Vos, A.; Lejaeghere, K.; Vanpoucke, D. E. P.; Joos, J. J.; Smet, P. F.; Hemelsoet, K., First-Principles Study of Antisite Defect Configurations in ZnGa2O4:Cr Persistent Phosphors. *Inorganic Chemistry* **2016**, *55*, 2402-2412.

18. Caldas, M. J.; Fazzio, A.; Zunger, A., A Universal Trend in the Binding Energies of Deep Impurities in Semiconductors. *Applied Physics Letters* **1984**, *45*, 671-673.

19. Wei, S.-H.; Zunger, A., Role of D Orbitals in Valence-Band Offsets of Common-Anion Semiconductors. *Physical Review Letters* **1987**, *59*, 144-147.

20. Xiaobo Chen, S. S., Liejin Guo, and Samuel S. Mao, Semiconductor-Based Photocatalytic Hydrogen Generation. *Chemical Reviews* **2010**, *110*, 6503–6570.

21. Van de Krol, R.; Liang, Y.; Schoonman, J., Solar Hydrogen Production with Nanostructured Metal Oxides. *Journal of Materials Chemistry* **2008**, *18*, 2311-2320.

22. Shi, R.; Qi, M.; Ning, L.; Pan, F.; Zhou, L.; Zhou, W.; Huang, Y.; Liang, H., Combined Experimental and Ab Initio Study of Site Preference of Ce3+ in SrAl2O4. *The Journal of Physical Chemistry C* **2015**, *119*, 19326-19332.

23. Kamada, M.; Murakami, J.; Ohno, N., Excitation Spectra of a Long-Persistent Phosphor SrAl2O4 : Eu, Dy in Vacuum Ultraviolet Region. *Journal of Luminescence* **2000**, *87–89*, 1042-1044.

24. Ayvacıklı, M.; Ege, A.; Yerci, S.; Can, N., Synthesis and Optical Properties of Er3+ and Eu3+ Doped SrAl2O4 Phosphor Ceramic. *Journal of Luminescence* **2011**, *131*, 2432-2439.

25. Rogers, E. G.; Dorenbos, P., Vacuum Referred Binding Energy of the Single 3d, 4d, or 5d Electron in Transition Metal and Lanthanide Impurities in Compounds. *ECS Journal of Solid State Science and Technology* **2014**, *3*, R173-R184.

26. Dorenbos, P., Ce3+ 5d-Centroid Shift and Vacuum Referred 4f-Electron Binding Energies of All Lanthanide Impurities in 150 Different Compounds. *Journal of Luminescence* **2013**, *135*, 93-104.

27. Ueda, J.; Meijerink, A.; Dorenbos, P.; Bos, A. J. J.; Tanabe, S., Thermal Ionization and Thermally Activated Crossover Quenching Processes for 5d-4f Luminescence in Y3Al5-xGaxO12:Pr3+. *Physical Review B* **2017**, *95*, 014303.

28. Bierwagen, J.; Yoon, S.; Gartmann, N.; Walfort, B.; Hagemann, H., Thermal and Concentration Dependent Energy Transfer of Eu2+ in SrAl2O4. *Optical Materials Express* **2016**, *6*, 793-803.

29. Van der Kolk, E.; Dorenbos, P.; de Haas, J.; van Eijk, C., Thermally Stimulated Electron Delocalization and Luminescence Quenching of Ce Impurities in GdAlO3. *Physical Review B* **2005**, *71*. 04512101-04512105

30. Ueda, J.; Tanabe, S.; Nakanishi, T., Analysis of Ce Luminescence Quenching in Solid Solutions between Y3Al5O12 and Y3Ga5O12 by Temperature Dependence of Photoconductivity Measurement. *Journal of Applied Physics* **2011**, *110*, 53102-531026.

31. Dobrowolska, A.; Dierre, B.; Fang, C. M.; Hintzen, H. T.; Dorenbos, P., Thermal Quenching of Eu2+ Emission in Ca- and Sr-Ga2S4 in Relation with Vrbe Schemes. *Journal of Luminescence* **2017**, *184*, 256-261.

32. Korthout, K.; Van den Eeckhout, K.; Botterman, J.; Nikitenko, S.; Poelman, D.; Smet, P. F., Luminescence and X-Ray Absorption Measurements of Persistent SrAl2O4:Eu,Dy Powders: Evidence for Valence State Changes. *Physical Review B* **2011**, *84*.085140-08514007

33. Bos, A. J. J.; van Duijvenvoorde, R. M.; van der Kolk, E.; Drozdowski, W.; Dorenbos, P., Thermoluminescence Excitation Spectroscopy: A Versatile Technique to Study Persistent Luminescence Phosphors. *Journal of Luminescence* **2011**, *131*, 1465-1471.

34. Qu, B.; Zhang, B.; Wang, L.; Zhou, R.; Zeng, X. C., Mechanistic Study of the Persistent Luminescence of CaAl2O4:Eu,Nd. *Chemistry of Materials* **2015**, *27*, 2195-2202.

35. Dorenbos, P., Valence Stability of Lanthanide Ions in Inorganic Compounds. *Chemistry of Materials* **2005**, *17*, 6452-6456.

36. Bos, A. J. J.; Dorenbos, P.; Bessière, A.; Lecointre, A.; Bedu, M.; Bettinelli, M.; Piccinelli, F., Study of Tl Glow Curves of YPO4 Double Doped with Lanthanide Ions. *Radiation Measurements* **2011**, *46*, 1410-1416.

37. You, F.; Bos, A. J. J.; Shi, Q.; Huang, S.; Dorenbos, P., Thermoluminescence Investigation of Donor Ce3+, Pr3+, Tb3+ Acceptor Eu3+, Yb3+ Pairs in Y3Al5O12. *Physical Review B* **2012**, *85*, 115101.

38. Luo, H.; Bos, A. J. J.; Dobrowolska, A.; Dorenbos, P., Low-Temperature Vuv Photoluminescence and Thermoluminescence of Uv Excited Afterglow Phosphor Sr3AlxSi1-xO5:Ce3+,Ln3+ (Ln = Er, Nd, Sm, Dy and Tm). *Physical Chemistry Chemical Physics* **2015**, *17*, 15419-15427.

39. Luo, H.; Bos, A. J. J.; Dorenbos, P., Controlled Electron–Hole Trapping and Detrapping Process in GdAlO3 by Valence Band Engineering. *The Journal of Physical Chemistry C* **2016**, *120*, 5916-5925.

40. Dobrowolska, A.; Bos, A. J. J.; Dorenbos, P., Electron Tunnelling Phenomena in YPO4:Ce,Ln (Ln = Er, Ho, Nd, Dy). *Journal of Physics D: Applied Physics* **2014**, *47*, 335301-335310.

41. Chakrabarti, K.; Mathur, V.; Rhodes, J. F.; Abbundi, R., Stimulated Luminescence in Rare-Earth-Doped MgS. *Journal of Applied Physics* **1988**, *64*, 1363-1366.

42. Hajime Yamamoto; Matsuzawa, T., Mechanism of Long Phosphorescence of SrAl2O4:Eu2+, Dy3+ and CaAl2O4:Eu2+, Nd3+. *Journal of Luminescence* **1997**, *72*, 287-289.

43. Dorenbos, P., Mechanism of Persistent Luminescence in Eu2+ and Dy3+ Codoped Aluminate and Silicate Compounds. *Journal of the Electrochemical Society* **2005**, *152*, H107-H110

44. Zhuang, Y.; Ueda, J.; Tanabe, S., Tunable Trap Depth in Zn(Ga1-xAlx)2O4:Cr,Bi Red Persistent Phosphors: Considerations of High-Temperature Persistent Luminescence and Photostimulated Persistent Luminescence. *Journal of Materials Chemistry C* **2013**, *1*, 7849-7855.

45. Ueda, J.; Dorenbos, P.; Bos, A.; Kuroishi, K.; Tanabe, S., Control of Electron Transfer between Ce3+ and Cr3+ in Y3Al5-xGaxO12 Host by Conduction Band Engineering. *Journal of Materials Chemistry C* **2015**, *3*, 5642-5651

2

Experimental Techniques

Luminescence research is a comprehensive chemical-physics study with different techniques. In this chapter the setups for the afterglow research conducted on this thesis are briefly overviewed and described.

2.1 Photoluminescence

Figure 2.1 shows the photoluminescence spectrometer. The spectrometer is constituted by an UV/vis branch (right part) and a VUV/UV branch (left part). The UV/vis branch consists of a 500W Hamamatsu CW Xe lamp (1) and a Gemini 180 double-grating monochromator (2). The VUV/UV branch uses a Hamamatsu L1835 deuterium lamp (3) with an ARC VM502 vacuum monochromator (4). The emission from the sample is dispersed with a Princeton Acton Instruments SP2300 monochromator (5) and detected by the Perkin Elmer MP-1993 photomultiplier tube (6). The detector can be changed to the Hamamatsu C9100-13 EM-CCD Camera (7) or the Hamamatsu H10330A-75 NIR PMT (8).

A SHI-APD, DE-204SLFF liquid helium cryostat can be mounted on the sample chamber to perform the photoluminescence measurements below room temperature (minimum 10 K). Thermal quenching measurements (10 to 350 K) were performed by the same cryostat connected to a LakeShore Model 331 temperature controller.
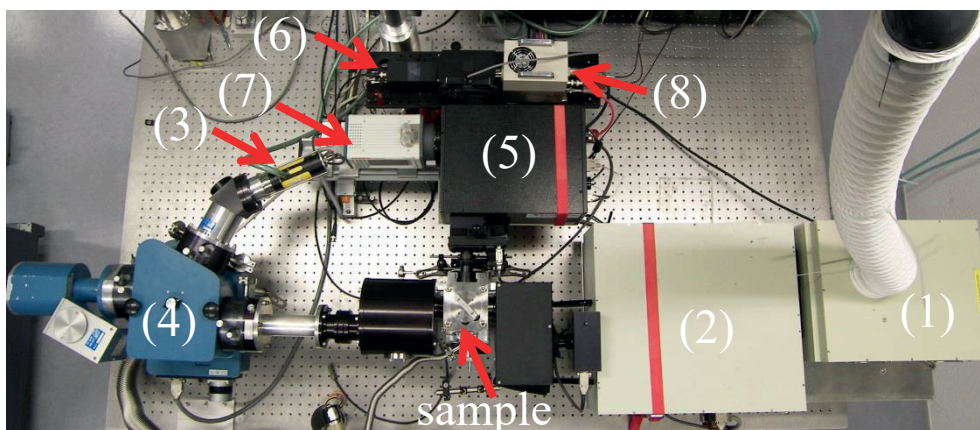
Figure 2.1. The photoluminescence spectrometer.

2.2 Thermoluminescence

Thermoluminescence (TL), which actually should be called as thermally stimulated luminescence, is a luminescence phenomenon of an insulator or semiconductor which can be observed when the solid is thermally stimulated[1].

Figure 2.2a shows the scheme of a TL reader. After the sample has been irradiated (the irradiation can be monochromatic photons or ionizing radiation) for a certain time, it is heated in a controlled way with a constant heating rate. A filter can be inserted between the sample and the PMT to select a particular luminescence recombination center or to block the blackbody radiation[4]. When the luminescence intensity is plotted as a function of temperature, we get a so-called "thermoluminescence glow curve". Three typical glow curves are shown in Figure 2.2b. The temperature where the TL glow curve appears is approximately proportional to the trap depth. A deeper trap requires more energy to release the captured charge carrier which causes the TL glow curve to appear at a higher temperature.
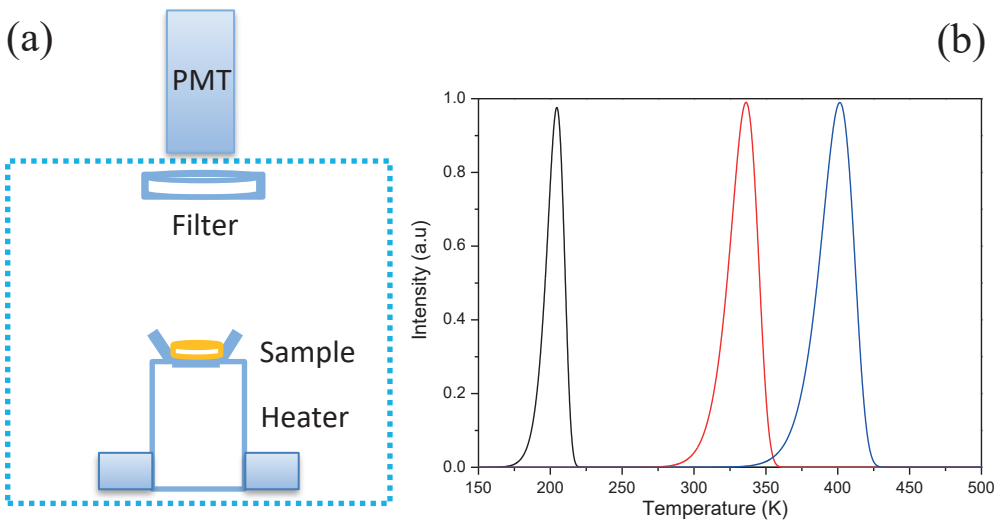
Figure 2.2. (a) scheme of a thermoluminescence reader. The schematic is replotted from the Ref.4. (b) thermoluminescence glow curves at different temperatures.

2.2.1 Low-temperature thermoluminescence

Figure 2.3 shows the low-temperature thermoluminescence (LTTL) setup. The LTTL measurements (90-450 K) were recorded with a sample chamber (1) operating under vacuum (P = 10^{-7} mbar). A ^{90}Sr/^{90}Y radioactive source was used as the beta irradiation source (2) with dose rate of ~0.4 mGys^{-1} and a Perkin-Elmer channel PM tube (MP-1393) (3) was used as the detector. A filter (4) can be placed between the sample and the PMT. Liquid nitrogen was used as a cooling medium[2].
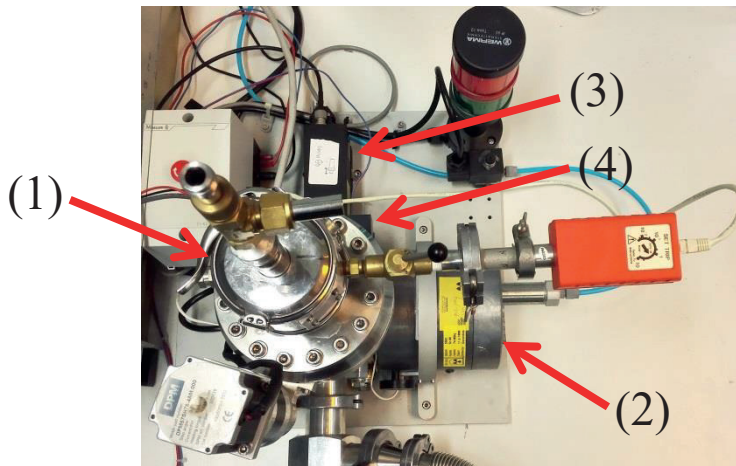
Figure 2.3. The low-temperature thermoluminescence setup.

2.2.2 High-temperature thermoluminescence

High-temperature thermoluminescence was performed using a RISØ TL/OSL reader (Figure 2.4) model DA-15 (1) and a controller model DA-20 (2). The heating rate under thermal stimulation can be varied from 0.01K/s up to 20 K/s and the heating can be performed from room temperature up to 700°C in N_2 or air atmosphere. Samples were irradiated with a ^{90}Sr/^{90}Y beta source (3) with a dose rate of 0.7 mGys^{-1}.
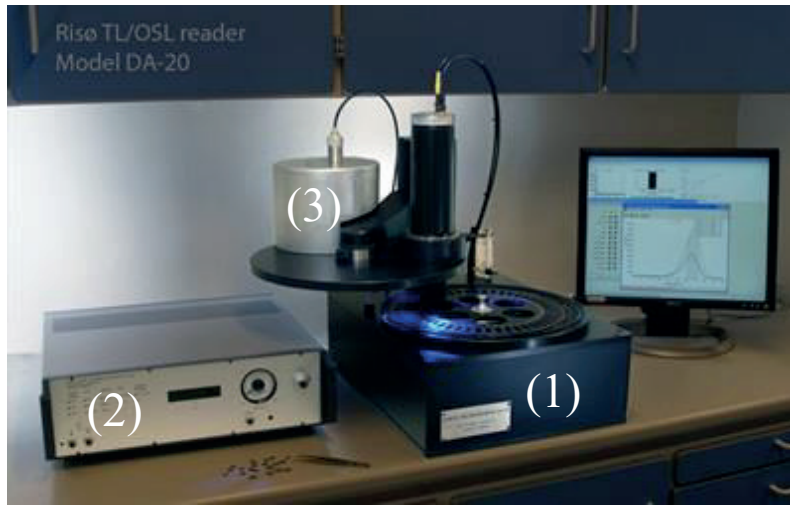
Figure 2.4. The RISØ TL/OSL thermoluminescence reader. The picture was taken from: http://www.nutech.dtu.dk/english/Products-and-Services/Dosimetry/Radiation-Measurement-Instruments/TL_OSL_reader/.

2.2.3 Thermoluminescence emission

The thermoluminescence (TLEM) emission spectra were measured by the above (Figure 2.4) RISØ TL/OSL reader by connecting it to a UV to vis spectrometer (Ocean Optics, QE65000) or a NIR spectrometer (Ocean Optics, NIRQ512) with a HR composite grating (300 lines/mm) and an entrance aperture of 100 µm resulting in a 3.3 nm (FWHM) wavelength resolution (Figure 2.5). The spectral range is 200 to 900 nm for QE65000 and 900 to 1700 nm for NIRQ512.
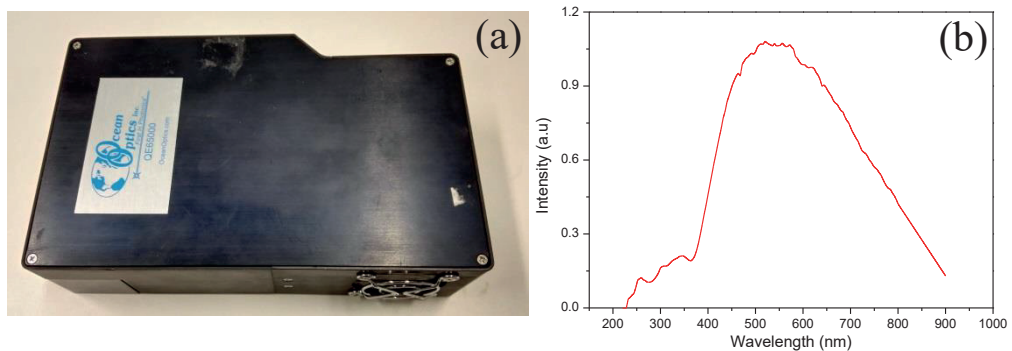
Figure 2.5. (a) The Ocean Optics QE65000 UV/vis fiber spectrometer. (b) The detector response curve of QE65000 spectrometer.

Samples were irradiated with a ^{60}Co gamma source before measuring[3]. The dose rate of the ^{60}Co source, that has been calibrated every year, was around 1.50, 1.32, 1.15 and 1.01 kGy/h in December of 2013, 2014, 2015 and 2016, respectively.

2.2.4 Thermoluminescence excitation

Figure 2.6 shows the setup for thermoluminescence excitation (TLE) spectra measurements, and Figure 2.7 shows the schematic of the setup to measure the TLE spectra.

The TL excitation spectra (TLE) were measured by first illuminating the samples with monochromatic photons from a 150 W Xenon arc lamp (1) (Hamamatsu L2273) filtered by a 1/8 monochromator (2) (Oriel Cornerstone 130) with wavelength resolution of 0.8 nm/0.1 mm slit width. Next, the system is programmed by LabVIEW to record all the TL glow curves from room temperature to the higher temperature for excitation wavelengths between 200 nm up to 1000 nm. The intensity of the photon beam at the exit of the fiber was measured and calibrated by a Si photodiode. To prevent over exposure of the PMT, a shutter between the sample and PMT is installed. The shutter was controlled by LabVIEW software to be closed during the illumination and to be opened during the TL readout[4].
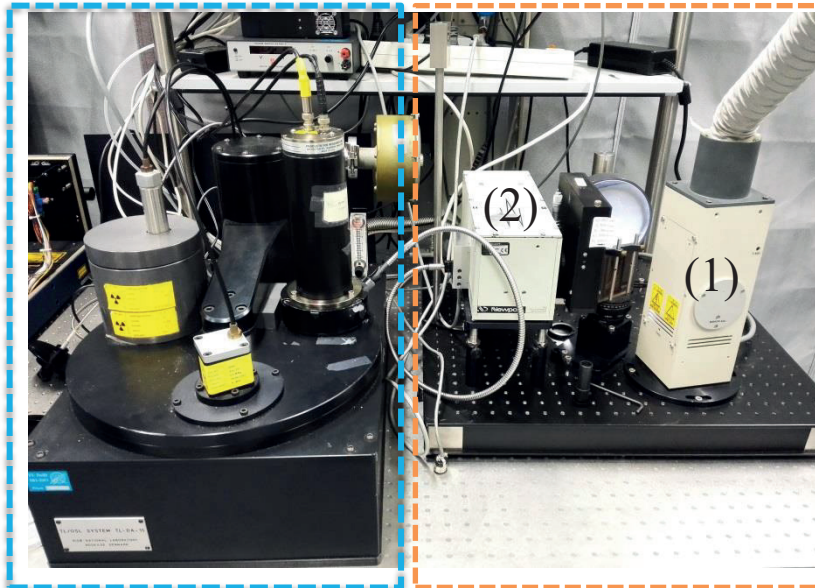
Figure 2.6. The setup to measure the TLE spectra. The right part is the home-made optical unit and the left part is the RISO reader.

A plot of the integrated TL glow peak intensity versus the excitation wavelength is called a TL excitation spectrum. The TL spectra were all recorded by a RISØ TL/OSL reader model DA-15 and a controller model DA-20. A filter can be placed between the sample and PMT to select a particular luminescence recombination center or to block the blackbody radiation[4].
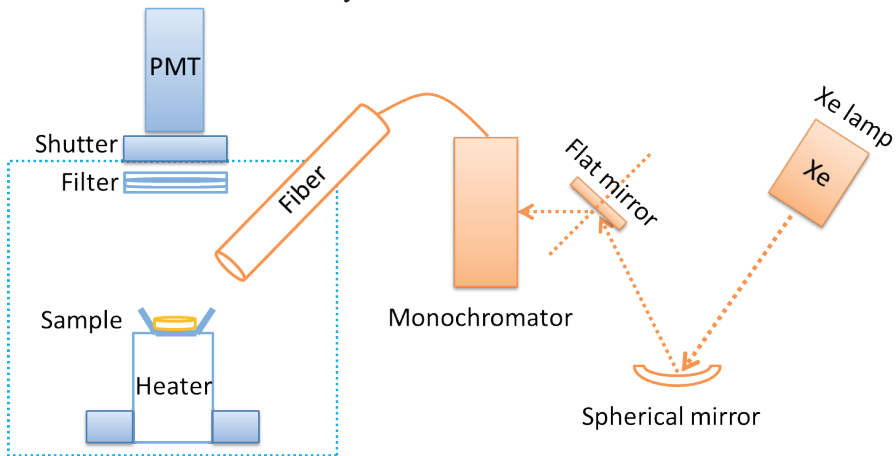
Figure 2.7. The schematic of the setup to measure the TLE spectra. The schematic is replotted from Ref.4.

2.3 Reference

1. Bos, A. J. J., Theory of Thermoluminescence. *Radiation Measurements* **2006**, *41, Supplement 1*, S45-S56.

2. Dobrowolska, A.; Bos, A. J. J.; Dorenbos, P., Electron Tunnelling Phenomena in YPO4:Ce,Ln (Ln = Er, Ho, Nd, Dy). *Journal of Physics D: Applied Physics* **2014**, *47*, 335301.

3. Bos, A. J. J.; Dorenbos, P.; Bessière, A.; Lecointre, A.; Bedu, M.; Bettinelli, M.; Piccinelli, F., Study of Tl Glow Curves of YPO4 Double Doped with Lanthanide Ions. *Radiation Measurements* **2011**, *46*, 1410-1416.

4. Bos, A. J. J.; van Duijvenvoorde, R. M.; van der Kolk, E.; Drozdowski, W.; Dorenbos, P., Thermoluminescence Excitation Spectroscopy: A Versatile Technique to Study Persistent Luminescence Phosphors. *Journal of Luminescence* **2011**, *131*, 1465-1471.

3

Low-Temperature VUV Photoluminescence and Thermoluminescence of UV Excited Afterglow Phosphor $Sr_3Al_xSi_{1-x}O_5$:Ce^{3+}, Ln^{3+} (Ln=Er, Nd, Sm, Dy and Tm)

3.1 Abstract

Low-temperature (10 K) photoluminescence excitation and emission spectra of undoped Sr_3SiO_5 as well as Ce^{3+} and Eu^{3+} single doped Sr_3SiO_5 have been investigated. They show the host exciton band and the O^{2-} to Eu^{3+} charge transfer band at 5.98 eV (207 nm) and 3.87 eV (320 nm) respectively. Low-temperature thermoluminescence measurements are reported for Ce^{3+} and lanthanides (Er, Nd, Sm, Dy, Er and Tm) codoped $Sr_3Al_xSi_{1-x}O_5$. The results show that Ce^{3+} is the recombination center and Nd, Sm, Dy and Tm work as electron traps with trap depths 0.95 eV, 1.89 eV, 1.02 eV, and 1.19 eV, respectively. Thermoluminescence excitation spectra of $Sr_{2.98}Al_{0.02}Si_{0.98}O_5:0.01Ce^{3+}$, $0.01Dy^{3+}$ show that the traps can be charged by 260 nm UV excitation.

3.2 Introduction

The afterglow, also called persistent luminescence, is a phenomenon whereby luminescence can last for certain time (from seconds to hours) after the stoppage of the excitation[1]. The afterglow phosphors have attracted great attention in different fields such as emergency signs, glow in the darkness road and in bio imaging [2-3]. Until now, dozens of persistent luminescence materials have been reported such as $Sr_4Al_{14}O_{25}:Eu^{2+},Dy^{3+}$ [4], $Sr_2MgSi_2O_7:Eu^{2+},Dy^{3+}$ [5], $Ca_2Si_5N_8:Eu^{2+},Tm^{3+}$ [6], $Y_3Al_2Ga_3O_{12}:Ce^{3+},Cr^{3+}$ [7]. The most widely used afterglow phosphor is still $SrAl_2O_4:Eu^{2+},Dy^{3+}$, which was developed in 1996 by Matsuzawa et al [8].

Lanthanide doped silicon based afterglow phosphors are of interest because of their chemical and physical stability and high luminescence efficiency. Ce^{3+} doped silicates as afterglow phosphors are much less studied than Eu^{2+} doped ones. One reason is that the emission of Ce^{3+} is normally in the UV or blue region in silicates[9], which does not fit with the human eye response curve very well.

Cerium doped Sr_3SiO_5, which has a tetragonal structure with the space group P4/*ncc*, shows a yellow emission (~530 nm) when excited by 410 nm visible light, that has attracted attention because a yellow Ce^{3+} emission in silicates is seldom seen, except for cerium doped silica garnets[10-12] and γ-$Ca_2SiO_4:Ce^{3+}$ [13-14]. The charge imbalance between Ce^{3+} and Sr^{2+} ions in Sr_3SiO_5 can be compensated by codoping Li^+ into the Sr^{2+} site[15] or Al^{3+} into the Si^{4+} site[16], to increase the

luminescence intensity. Because of the yellow emission and possibility to excite with visible light (day light), Ce^{3+} doped Sr_3SiO_5, is an interesting study material as afterglow phosphor.

Previous reports on afterglow properties of Sr_3SiO_5 were almost all focused on Eu^{2+} doped ones, and long persistent phosphorescence in $Sr_3SiO_5:Ce^{3+}$ has not been reported yet. Next to the luminescence center, the nature of the charge carrier traps plays a crucial role in the afterglow intensity and the afterglow time duration in persistent luminescence materials[17]. Thermoluminescence (TL) is a versatile technique to identify the traps as well as the trap depth. In previous reports, high-temperature TL measurement of Eu^{2+} and Dy^{3+} codoped Sr_3SiO_5 were reported by Sun *et al.*[18]. It showed that Dy^{3+} works as an electron trap and increases the afterglow duration. Later, Xu *et al.* reported that codoping with Nd^{3+}, Er^{3+} or Dy^{3+} into Eu^{2+} doped Sr_3SiO_5 prolongs the afterglow compared to $Sr_3SiO_5:Eu^{2+}$. There is no information about the TL glow curves of Sr_3SiO_5 below room-temperature.

This work will be divided into two parts. Firstly the low-temperature VUV photoluminescence spectroscopy for the undoped Sr_3SiO_5 and Sr_3SiO_5 single doped with Ce^{3+} or Eu^{3+} are presented. Results are used to construct the energy level diagram of Sr_3SiO_5 showing the location of the lanthanide states within the bandgap. In the second part the low-temperature thermoluminescence (TL), TL emission spectra, and TL excitation spectra of the cerium and lanthanide codoped samples are reported. Finally, all results are used to propose the UV excited persistent luminescence mechanism.

3.3 Experimental

All starting materials were purchased from Sigma-Aldrich and used without further treatment. We used a typical synthesizing procedure. The appropriate stoichiometric mixture of $SrCO_3$ (99.999%), SiO_2 (quartz sand, 99.99%), Al_2O_3 (99.99%), Eu_2O_3 (99.99%), CeO_2 (99.99%), Nd_2O_3 (99.99%), Sm_2O_3 (99.99%), Dy_2O_3 (99.99%), Er_2O_3 (99.99%) and Tm_2O_3 (99.99%) were weighted according to the chemical formula and milled homogeneously. Then the powders were synthesized at 1450°C for 8 hours in a corundum crucible in air. The as-prepared materials were grinded again and synthesized at 1550°C for 8 hours in a reducing atmosphere of N_2/H_2 (N_2:93%, H_2:7%). After that, obtained compounds were

cooled down to room temperature. The sample single doped with Eu ($Sr_{2.975}Al_{0.025}Si_{0.975}O_5:0.025Eu^{3+}$) was synthesized in air with the above procedures. All powders were checked with a PANalytical XPert PRO X-ray diffraction system with Co Kα (λ = 0.178901 nm) x-ray tube (45 kV, 40 mA). The photoluminescence excitation (PLE) and photoluminescence emission (PL) measurement were measured with a set-up that consists of an UV/vis branch with a 500W Hamamatsu CW Xe lamp and Gemini 180 monochromator and a VUV/UV branch using a deuterium lamp with an ARC VM502 vacuum monochromator. The Perkin Elmer MP-1913 photomultiplier was exploited as a detector connected with Princeton Acton SP2300 monochromator. The sample holder is a custom built vacuum sample chamber.

TL measurements above room temperature (25-450 °C) were performed with a RISØ TL/OSL reader model DA-15 and a controller model DA-20. Samples were irradiated with a $^{90}Sr/^{90}Y$ beta source with a dose rate of 0.7 mGys^{-1}. Low temperature TL measurements (90-450 K) were recorded with a sample chamber operating under vacuum (P = 10^{-7} mbar), a $^{90}Sr/^{90}Y$ beta irradiation source having a dose rate of ∼0.4 mGys^{-1} and a Perkin-Elmer channel PM tube (MP-1393). Liquid nitrogen was used as a cooling medium[19].

TL emission spectra (TLEM) were measured using an UV to vis spectrometer (Ocean Optics, QE65000) with a HR composite grating (300 lines/mm) and an entrance aperture of 100 μm resulting in a 3.3 nm (FWHM) wavelength resolution in the 200 to 900 nm spectral range. Samples were irradiated with a ^{60}Co gamma source to an absorbed dose of 2.5 kGy.

The TL excitation spectra (TLE) were measured by first illuminating the sample during 300 s with a monochromatic photon beam produced with a 150 W Xenon arc lamp (Hamamatsu L2273) filtered by a 1/8 monochromator (Oriel Cornerstone 130) with wavelength resolution of 0.8 nm/0.1 mm slit width. Next, the system is programmed to record all the TL glow curves from room temperature to 450 °C with changing illumination wavelength. The plot of the integration of all the TL glow curves *versus* illumination wavelength is called TL excitation spectra. In case of TL and TLE measurements, a 2 mm Hoya BG 39 filter transmitting from about 380 nm to 650 nm is placed between the samples and PMT in order to block the blackbody radiation.

30

3.4 Results and discussion

3.4.1 Low-temperature VUV photoluminescence and energy level diagram of Sr_3SiO_5

Figure 3.1 shows XRD patterns of Ce^{3+} single doped Sr_3SiO_5 and Ce^{3+} and Al^{3+} codoped Sr_3SiO_5. Both samples are of single phase and match very well with the Sr_3SiO_5 reference card JCODF No.26-0984.
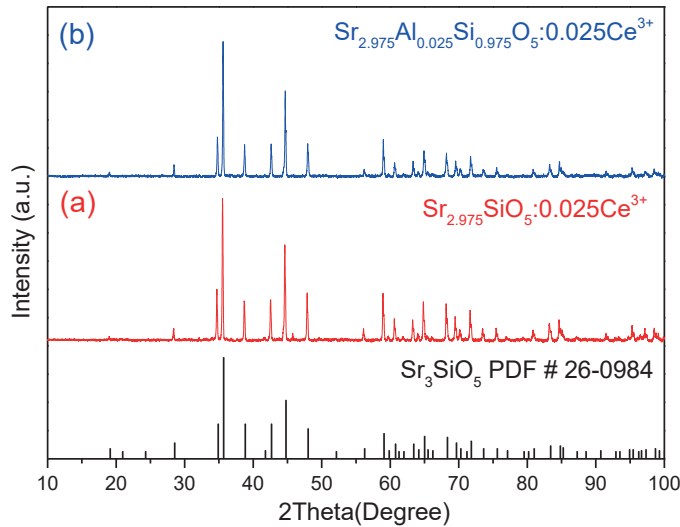
Figure 3.1. XRD patterns of the as-prepared samples of (a) Ce^{3+} single doped Sr_3SiO_5 and (b) Ce^{3+} and Al^{3+} codoped Sr_3SiO_5.

Figure 3.2 shows the low temperature PLE and PL spectra of $Sr_{2.975}Al_{0.025}Si_{0.975}O_5$:$0.025Ce^{3+}$. The excitation spectra (Figure 3.2b) ranging from 150 to 500 nm are composed of six bands. The most intense band is at 410 nm and due to the characteristic Ce^{3+} excitation from the $4f(^2F_{5/2})$ ground state to the first 5d state $5d_1$. The excitation bands located at 345 nm and 316 nm are due to excitation to the $5d_2$ and $5d_3$ levels. At room temperature, the $5d_2$ and $5d_3$ bands broaden and merge into one broad band centered at 330 nm [15-16]. The emission spectrum in Figure 3.2b is composed of the two unresolved $5d_1$-$^2F_{5/2}$ and $5d_1$-$^2F_{7/2}$ emission bands. We estimate the short wavelength band near 520 nm and the longer wavelength band at 2000 cm^{-1} lower energy near 580 nm. The Stokes shift is then estimated to be around 5200 cm^{-1}.

31
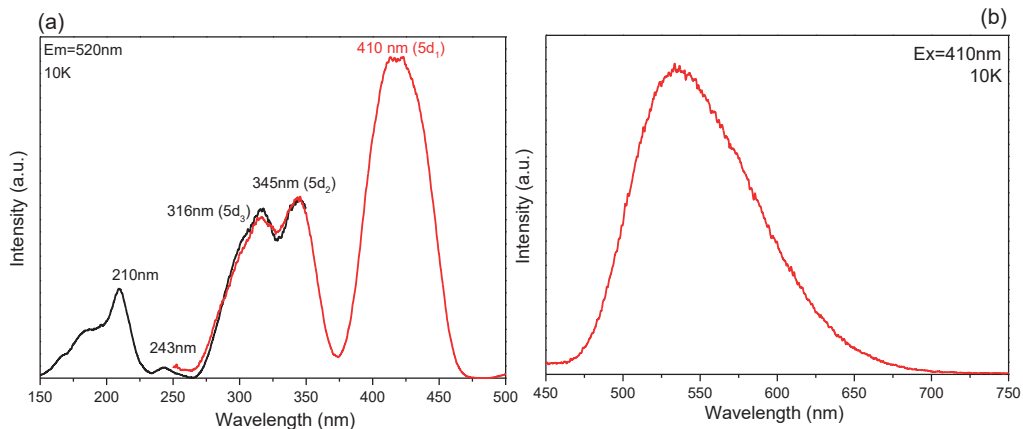
Figure 3.2. PLE (a) and PL spectra (b) of $Sr_{2.975}Al_{0.025}Si_{0.975}O_5:0.025Ce^{3+}$. The excitation spectrum from 150 to 350 was measured by deuterium lamp excitation (black line). The excitation spectrum from 250 nm to 500 nm was measured by Xe lamp excitation (red line). All measurements were performed at 10 K.

The excitation and emission spectra of undoped Sr_3SiO_5 are displayed in Figure 3.3. When the sample is excited by 207 nm UV irradiation, one broad emission band peaked at 440 nm with a shoulder centered at 350 nm is observed. The excitation spectrum monitored at 440 nm emission shows peaks around 207 nm, 223 nm, and 237 nm. Those at 207 nm and 237 nm are very close to the 210 nm and 243 nm bands observed for Ce^{3+} doped Sr_3SiO_5 in Figure 3.2a. It implies that those excitation bands cannot be attributed to the $5d_5$ and $5d_4$ excited states of Ce^{3+}. Instead, the band at 207 nm is attributed to host exciton creation and the one at 237-243 nm to unknown defects.
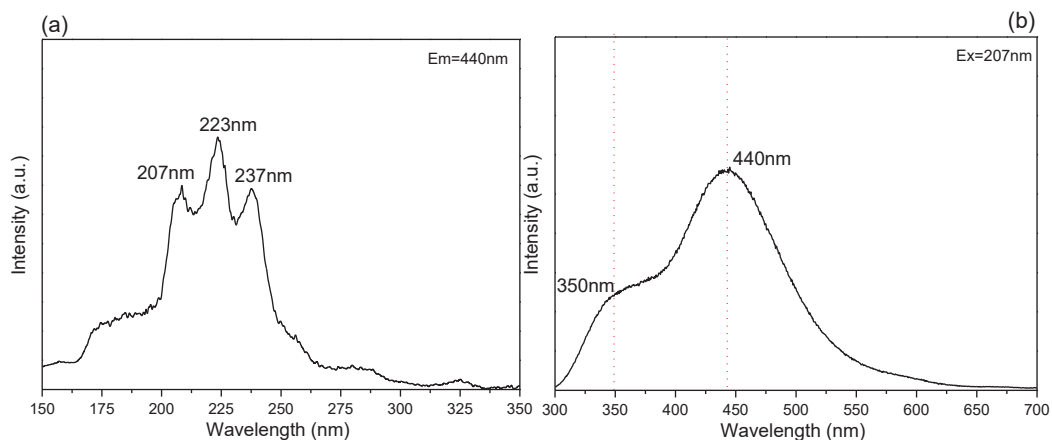
Figure 3.3. PLE (a) and PL spectra (b) of undoped Sr_3SiO_5, the excitation spectra were measured from 100 to 350 nm by using a Deuterium lamp and monitoring 440 nm emission. The emission spectrum was measured under 207 nm excitation. All spectra were measured at 10 K.

To explain the anomalous yellow emission of Ce^{3+} and to construct a vacuum referred binding energy scheme it is of much help to know the centroid shift and total crystal field splitting of the 5d-configuration. The centroid shift ε_c is defined as the lowering of the average energy of the five 4f-5d$_i$ transitions in a certain compound compared to the value of 6.35 eV that applies to the free Ce^{3+} ion. The total crystal field splitting is defined as the energy difference between the highest energy 4f-5d$_5$ and lowest energy 4f-5d$_1$ transition. Because the 5d$_5$ and 5d$_4$ bands of Ce^{3+} cannot be identified from the photoluminescence spectra, both the 5d-centroid shift and the 5d crystal field splitting cannot be derived from the photoluminescence excitation spectra and we need to use predictive methods.

The 5d centroid shift $\epsilon_c(1,3+,A)$ for Ce^{3+} in a specific host lattice (A) is related to[20-21]

$$U(6,A) = 5.44 + 2.834e^{-\epsilon_c(1,3+,A)/2.2} \qquad 3.1$$

where $U(6,A)$ is the Coulomb repulsion energy for Eu, which is defined as

$$U(6,A) \equiv E_{4f}(7,2+,A) - E_{4f}(6,3+,A) \qquad 3.2$$

It means that the energy difference between the ground state energy of Eu^{2+} and Eu^{3+} [22], which can be estimated by comparison with established values for other silicate compounds as 6.7 eV in Sr_3SiO_5 [21].

Using the value of 6.7 eV of $U(6,A)$, the centroid shift can be calculated as 1.75 eV (14000 cm^{-1}). From the centroid shift and the known energies of 5d$_1$, 5d$_2$ and 5d$_3$ bands the average energy of 5d$_5$ and 5d$_4$ bands is estimated as 6.24 eV (198 nm). This is at shorter wavelength than the host exciton creation band which then explains why those two bands were not observed in the excitation spectra of Figure 3.2.

The total crystal field splitting becomes at least 3.22 eV (26000 cm^{-1}), which is a typical value for Ce^{3+} in an octahedral site in oxides compounds [23]. The Stokes shift

of 5200 cm^{-1} in $Sr_3SiO_5:Ce^{3+}$ is almost twice compared to that in $YAG:Ce^{3+}$ and $Lu_2CaMg_2Si_3O_{12}:Ce^{3+}$. Evidently the yellow emission of Ce^{3+} doped Sr_3SiO_5 is due to the combination of a large crystal field splitting and Stokes shift.

Table.1.1   Spectroscopic properties for various Ce^{3+} doped yellow-red oxides

Compound	Centroid Shift (cm^{-1})	Crystal Field Splitting (cm^{-1})	Stokes Shift (cm^{-1})	Ref
Sr_3SiO_5	14000 (estd)	>26000 (estd)	5200	This work
$Y_3Al_5O_{12}$	14700	27000	2700	10, 23
$Lu_2CaMg_2Si_3O_{12}$	13300	29000-30500	2550	10

Figure 3.4 shows low temperature PLE and PL spectra for $Sr_{2.975}Al_{0.025}Si_{0.975}O_5:0.025Eu^{3+}$. The excitation spectrum shows a very broad band with FWHM 0.96 eV and centered at 313 nm (3.96 eV) which is attributed to the O^{2-} to Eu^{3+} charge transfer band.
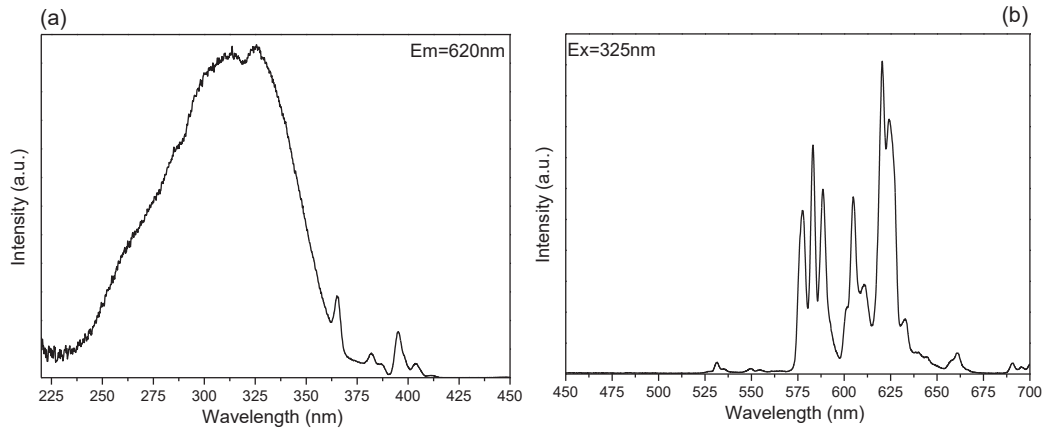
Figure 3.4. PLE (a) and PL (b) spectra of $Sr_{2.975}Al_{0.025}Si_{0.975}O_5:0.025Eu^{3+}$. The excitation spectrum was measured from 225 to 450 nm by a Xe lamp monitoring 620 nm emission. The emission spectrum was measured under 325 nm excitation. All the measurements were carried out at 10 K.

The 3.96 eV energy defines the relative position of the Eu^{2+} $4f^7$ ($^8S_{7/2}$) ground state level above the top of the valence band. A vacuum referred binding energy (VRBE) diagram shows electron binding energies in lanthanide and host band

states relative to the vacuum, i.e. the energy of an electron at rest in vacuum. The VRBE of an electron in the Eu^{2+} $4f^7(^8S_{7/2})$ ground state can be calculated as following equation [22].

$$E_{4f}(7,2+,A) = -24.92 + \frac{18.05 - U(6,A)}{0.777 - 0.0353U(6,A)} \qquad 3.3$$

Adopting 6.7 eV for $U(6,A)$, $E_{4f}(7,2+,A)$ is calculated as -3.93 eV. The VRBE Ev at the top of valence band is then at -7.89 eV. The mobility band gap E_{VC}, or the energy between the bottom of CB E_C and E_V, can be obtained from the host exciton creation energy of 5.98 eV (207 nm) by adding the exciton binding energy. For wide band gap compounds like the silicates it is estimated around 8% of the exciton creation energy, resulting in E_{VC} = 6.45 eV[22].

Figure 3.5 displays the obtained VRBE scheme for Sr_3SiO_5. The zigzag curves labelled GS (3+) and GS (2+) connect the binding energies in the ground state levels of the trivalent and the divalent lanthanides, respectively. The curve labelled ES (3+) connects the binding energies in the $5d_1$ excited state of the trivalent lanthanides to which spin allowed transitions from the $4f^n$ ground state can take place. The $5d_1$ state of Ce^{3+} is located at -2.26 eV, which is 0.88 eV below the conduction band. The average VRBE in the $5d_5$ and $5d_4$ levels of Ce^{3+} are far above the bottom of the conduction band. The ground states of divalent Nd, Sm, Eu, Dy, Ho, Tm and Yb are below the conduction band which indicates that the corresponding trivalent ions can work as electron traps.
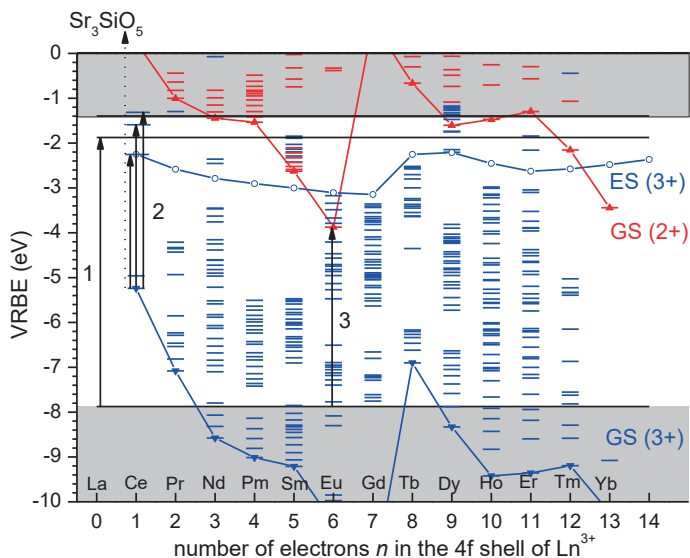
Figure 3.5. Low temperature vacuum referred binding energy level diagram for Sr_3SiO_5. Arrow 1 shows the inter band transitions from the valence to conduction band. Arrow 2 is the 4f to $5d_1$, $5d_2$ and $5d_3$ electron transitions in trivalent Ce. Arrow 3 indicates the charge transfer from O^{2-} to Eu^{3+}.
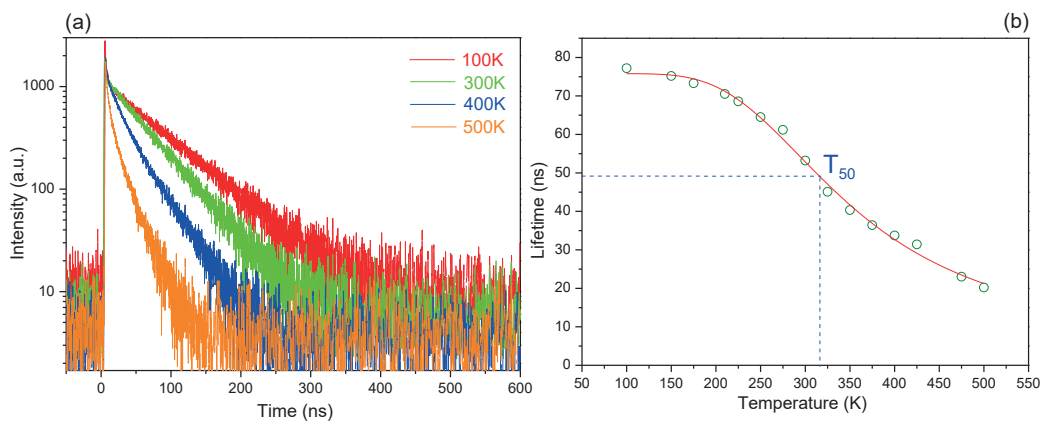
Figure 3.6. A decay curves as function of temperature and (b) temperature dependence of the life time of Ce^{3+} emission in $Sr_{2.975}Al_{0.025}Si_{0.975}O_5:0.025Ce^{3+}$. The solid curve through the data in (b) is a fitted curve.

By studying the temperature dependence of the Ce^{3+} $5d_1$ emission decay, the activation energy for thermal quenching can be determined. 5d-4f decay time curves are shown in Figure 3.6a, which were fitted by a single exponential.

$$I = I_0\exp(-\frac{t}{\tau}) \qquad 3.4$$

where I is the luminescence intensity, I_0 is the intensity at time 0, t is the time, and τ is the life time or decay time constant.

Figure 3.6b shows the lifetime of $Sr_{2.975}Al_{0.025}Si_{0.975}O_5$:$0.025Ce^{3+}$ as function of temperature. At low temperature it is about 75 ns and at the quenching temperature T_{50}=315 K it has reduced to 50% of that value. The activiation energy for thermal quenching can be derived from [24]:

$$\tau(T) = \frac{\tau(0)}{1+C\exp(-\frac{E}{kT})} \qquad 3.5$$

Where τ (T) and τ (0) is the life time at temperature T and 0. A fit through the data in Figure 3.6b, as indicated by the solid curve provides E = 0.12 eV, C=36.97. In case of quenching via thermal ionziation to the conduction band or via an impurity trapped exciton state, $i.e.$ Ce^{4+} plus an electron orbiting around it in conduction band derived states, this energy should be similar to the energy difference between the $5d_1$ level and E_C or E_X. However, Figure 3.5 reveals the energy difference of 0.88 eV and 0.40 eV which is quite different from the activation energy derived from Eq. 3.5. Considering the large Stokes shift of Ce^{3+} emission, we propose that thermal quenching of Ce^{3+} emission can also be due to the thermal relaxation from the 5d to 4f ground state via the so-called crossing point in the configuration coordinate diagram [25].

3.4.2 Thermoluminescence and afterglow properties of Ce^{3+} and lanthanides codoped Sr_3SiO_5

Figure 3.7 shows low temperature TL glow curves of Sr_3SiO_5 doped with different rare earth ions ($Sr_{2.98}Al_{0.02}Si_{0.98}O_5$:$0.01Ce^{3+}$, $0.01RE^{3+}$). All samples except that with Nd^{3+} show the most intense peak at around 250 K. It is attributed to a host defect related glow peak. The samples codoped with Al^{3+}, which works as a charge compensator, all show a peak around 200 K which is absent in glow curve (f) of the non-codoped sample. For the Dy^{3+} codoped sample, glow curve (a), an

additional peak appears near 310 K that is absent in glow curve (f). Also for the samples codoped with Tm^{3+}, curve (c) or Sm^{3+} curve (g) additional peaks appear at 375 K and 589 K, respectively. For the Nd^{3+} codoped sample, an additional peak appears at 295 K. No TL glow peaks were observed related to Yb in the Yb codoped samples.
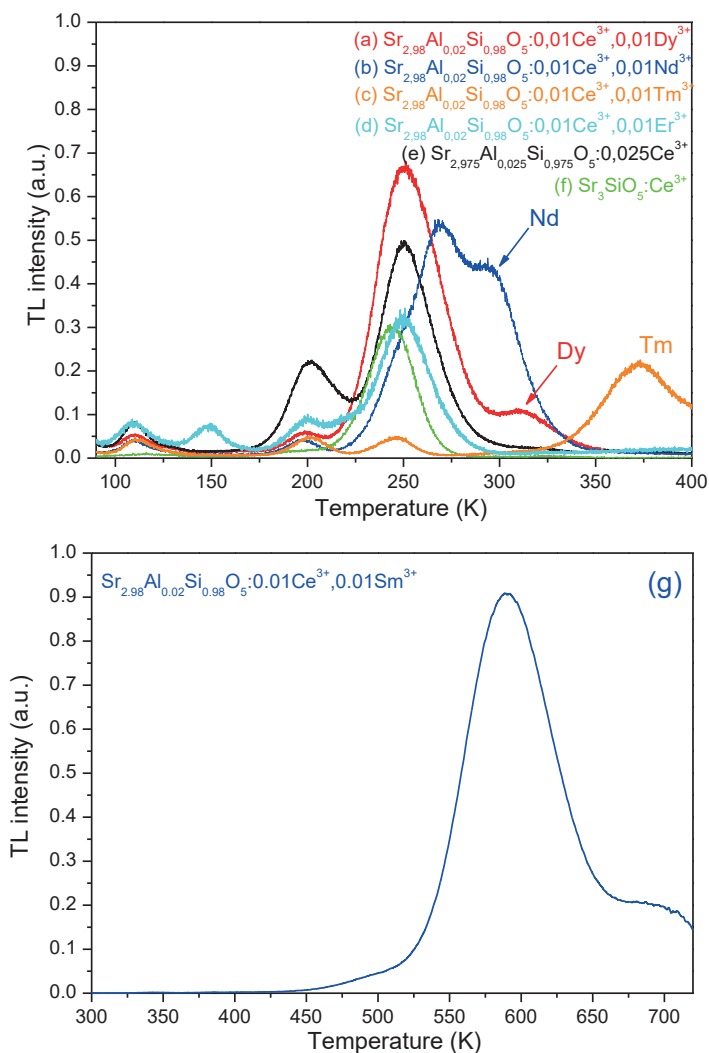
Figure 3.7. Low-Temperature thermoluminescence (LTTL) glow curves of Sr_3SiO_5 doped with different lanthanide ions. Glow curves (a) to (f) were measured by the low-

temperature TL setup from 90 to 400K with 100s irradiation by its β source. Figure 3.7(g) was recorded by the RISØ TL-reader from 300 to 725K with 100s irradiation by its β source. The heating rate was 0.1K/s for all TL-recordings.
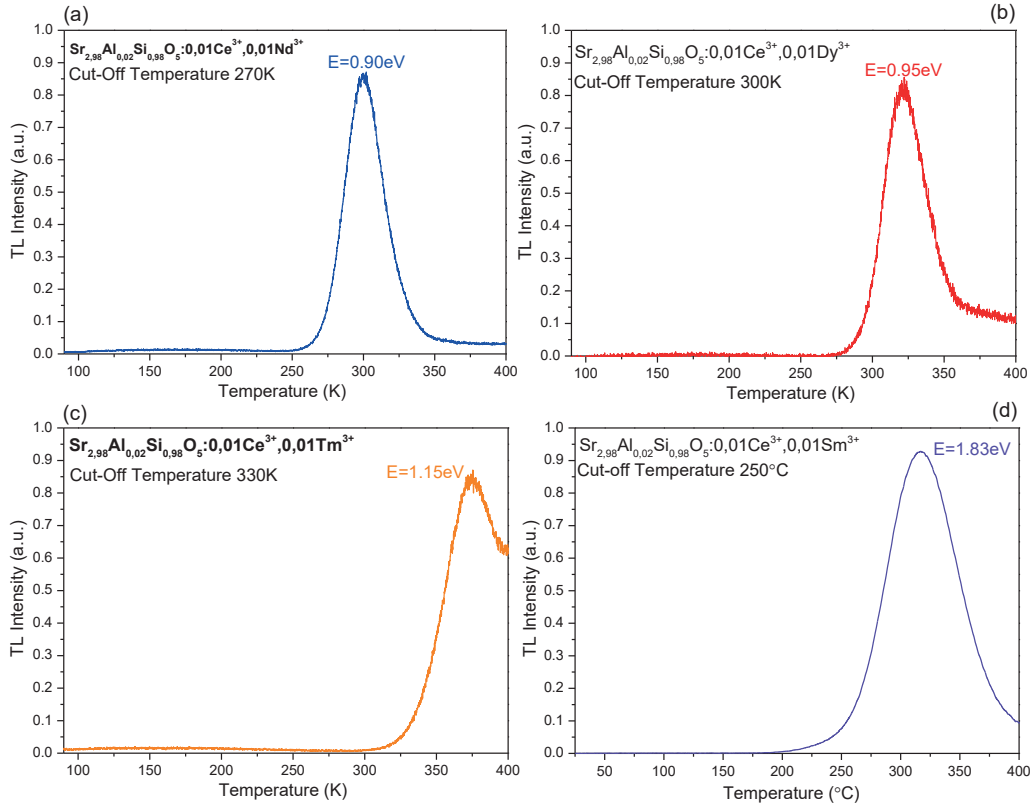
Figure 3.8. Thermoluminescence glow curves of (a) $Sr_{2.98}Al_{0.02}Si_{0.98}O_5$:$0.01Ce^{3+}$,$0.01Nd^{3+}$, (b) $Sr_{2.98}Al_{0.02}Si_{0.98}O_5$:$0.01Ce^{3+}$,$0.01Dy^{3+}$, (c) $Sr_{2.98}Al_{0.02}Si_{0.98}O_5$:$0.01Ce^{3+}$,$0.01Tm^{3+}$, (d) $Sr_{2.98}Al_{0.02}Si_{0.98}O_5$:$0.01Ce^{3+}$,$0.01Sm^{3+}$ after different cut-off temperature. The cut-off temperature is 270K, 300K, 330K and 523K for (a), (b), (c) and (d), respectively. The heating rate for read out is 0.1 K/s for all samples.

The additional glow peaks observed in the Dy, Tm, Sm, and Nd, codoped samples are attributed to the release of electrons trapped in the lanthanide. Their trapping depths E (eV) are determined using Eq. 3.6[26]

$$\frac{\beta E}{kT_m^2} = s\exp(-\frac{E}{kT_m}) \qquad 3.6$$

39

where β is the heating rate, k is Boltzman constant (eV/K), s (s^{-1}) the frequency factor, and T_m is the temperature (K) of the glow curve peak maximum. To calculate the trap depth we need to know s and $T_{m.}$. The frequency factor, which is related to the host lattice vibrational mode of the $[SiO_4]^{4-}$ group, is calculated using the vibrational energy for $[SiO_4]^{4-}$ group of 1000 cm^{-1} [26] and is found to be 3.0×10^{13} s^{-1} and is assumed to be the same for all samples. A more reliable value for T_m is found after thermal peak cleaning. Figure 3.8 shows the four TL glow curves after such cleaning procedure. With T_m and the mentioned s value the trap depth of Nd^{3+}, Dy^{3+}, Tm^{3+} and Sm^{3+} is calculated with Eq. 3.6 and found to be 0.90 eV, 0.95 eV, 1.15 eV and 1.83 eV, respectively.
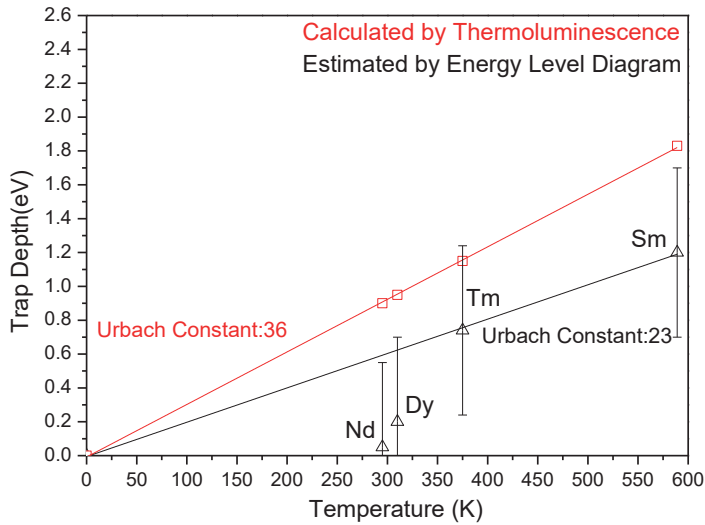
Figure 3.9. Comparison of the trap depths derived from the TL glow curves and the energy level diagram.

Figure 3.9 shows the trap depth calculated with Eq. 3.6 and the depth predicted from the VRBE scheme of Figure 3.5 against T_m. Data can be well fitted with a linear function

$$E = CkT_m \qquad 3.7$$

where E is the trap depth, c is the so called Urbach Constant, k is Boltzmann constant, and T_m is the temperature at the peak maximum. The Urbach Constant, which is 36, is proportional to the natural logarithm of the ratio of the frequency

40

factor (s) and the heating rate (β), that is normally between 18 to 44 for s/β between 10^8 and 10^{18}, respectively. Similar proportional relation was reported for lanthanides in YPO_4 [27] and $CaSO_4$[28] with the value of 40.8 and 37.1, respectively. The trap depths derived from the VRBE scheme show that data on Tm and Sm follow a proportional relation with the constant 23. It is clear that the two lines in Figure 3.9 deviate. However, taking into account the error bars and realizing that there is an uncertainty in the slope of the line based on TL measurements as well, the trend is in agreement.

It shows that the ground state of Nd^{2+}, Dy^{2+}, Tm^{2+} and Sm^{2+} are all below the conduction band and the corresponding trivalent lanthanides can then work as the electron traps. The charge carriers generated by β source irradiation can move freely through the conduction and valence band. Electrons are then trapped by those lanthanides and the holes can be trapped on Ce or other defects. Figure 3.5 predicts that Sm has the deepest trap depth among the above four codopants (Nd, Dy, Tm and Sm), resulting in its TL glow curve at the highest temperature. Nd has the shallowest trap depth, and its TL glow curve is at the lowest temperature. The ground state energy of divalent Er is 0.15 eV lower than Nd according to Figure 3.5. From the proportional relationship of TL maximum temperature to trap depth in Figure 3.9, one can estimate that the Er related glow curve peak is at 252 K, which has a great overlap with the peak at 250 K, causing it cannot be observed. Therefore, the peak at 150 K is from some unknown defect not related to Er. On the other hand Yb can also act as electron trap with a trap depth of 0.87 eV deeper than that of Sm, which is 1.83 eV + 0.9 eV = 2.73 eV. Considering the calculated trap depth of Sm to be 1.83 eV (Figure 3.8), the TL glow peak temperature of that trap can be estimated at around 870 K. At such a high temperature, the emission of Ce will be totally quenched. This can explain the reason why no TL glow peak is observed for the Yb codoped sample.

So far, we concentrated on the nature of the electron-trapping center. TL emission (TLEM) spectra above room temperature have been recorded to establish the nature of the hole-trapping and recombination center. Figure 3.10a and 3.10b show that both of the single Ce doped samples contain two main recombination centers. The 363 K TL glow peak with emission centered at around 530 nm is due to recombination at Ce^{3+} and higher temperature glow peaks between 523 K and 723 K have 400 nm emission attributed to host lattice defect recombination centers.

The codoping by Al^{3+} generates other glow peaks in the range of 393 K to 473 K connect to host defect emission as shown in Figure 3.10b. Figure 3.10c shows that the glow curve of the Tm^{3+} codoped sample shifts to 423 K. For Sm^{3+} codoping the dominant glow peak at 623 K has its main emission at 380 nm in Figure 3.10d and also some of the recombination seems to occur on Ce^{3+}. No emission from Tm^{3+} or Sm^{3+} is monitored, which means that Tm^{3+} and Sm^{3+} do not work as recombination centers.
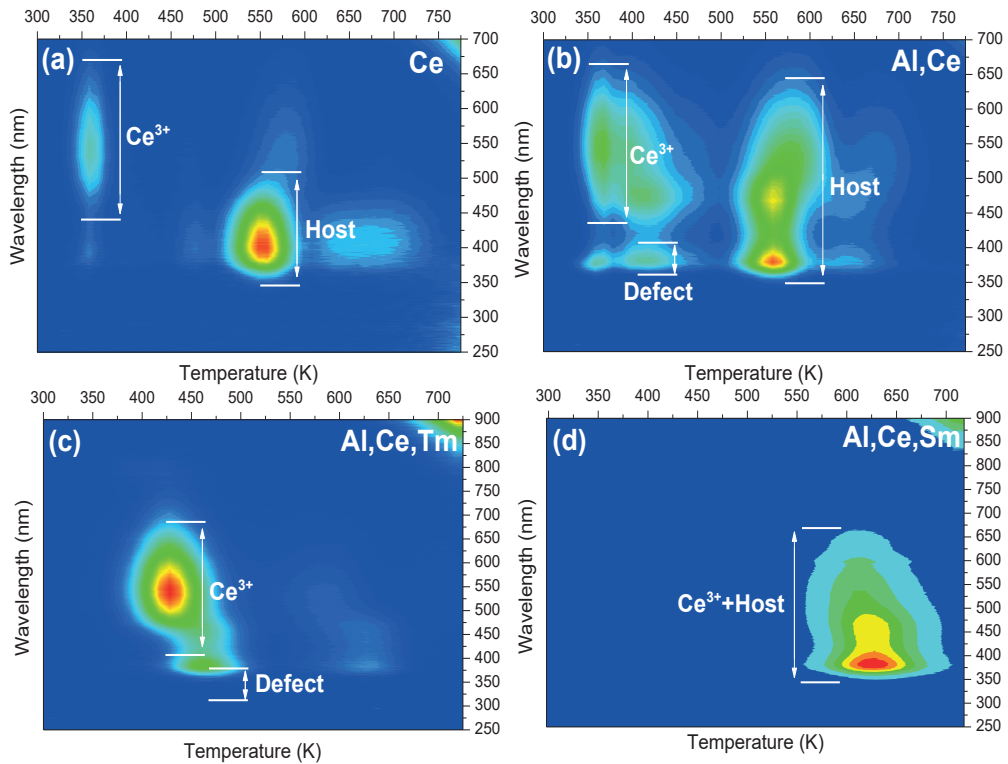
Figure 3.10. The thermoluminescence emission (TLEM) spectra of (a) $Sr_{2.975}SiO_5{:}0.025Ce^{3+}$, (b) $Sr_{2.975}Al_{0.025}Si_{0.975}O_5{:}0.025Ce^{3+}$, (c) $Sr_{2.98}Al_{0.02}Si_{0.98}O_5{:}0.01Ce^{3+}$, $0.01Tm^{3+}$, (d) $Sr_{2.98}Al_{0.02}Si_{0.98}O_5{:}0.01Ce^{3+}$, $0.01Sm^{3+}$. The heating rate for all of these samples is 5 K/s after exposure to irradiation of 2.5 kGy from a ^{60}Co source.

The TLEM and LTTL measurements show that the glow peaks in $Sr_{2.98}Al_{0.02}Si_{0.98}O_5{:}0.01Ce^{3+}$, $0.01Tm^{3+}$ and $Sr_{2.98}Al_{0.02}Si_{0.98}O_5{:}0.01Ce^{3+}$, $0.01Sm^{3+}$ samples are well above room temperature, and therefore they are not suitable as afterglow phosphors. Figure 3.11 shows the iso-thermal decay spectra. It indicates

that the Nd^{3+} codoped sample has the best initial intensity. After about 150 s, the luminescence intensity of the Dy^{3+} codoped sample is higher than that of the Nd^{3+} codoped one, indicating that Dy^{3+} has a longer decay time than Nd^{3+}. The reason is the 0.13 eV less shallow trap depth for Nd^{3+} codoped sample as compared to the 0.95 eV trap depth for the the Dy^{3+} codoped sample.
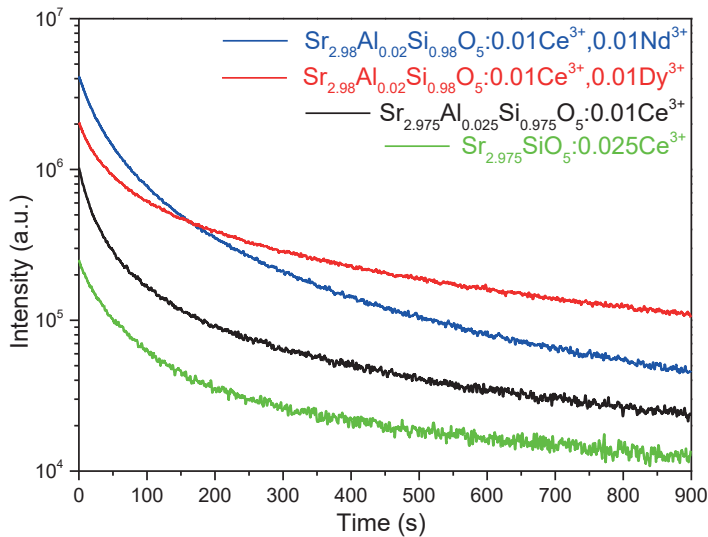
Figure 3.11. The room temperature iso-thermal decay spectra of $Sr_{2.975}SiO_5:0.025Ce^{3+}$, $Sr_{2.975}Al_{0.025}Si_{0.975}O_5:0.025Ce^{3+}$, $Sr_{2.98}Al_{0.02}Si_{0.98}O_5:0.01Ce^{3+}$, $0.01Nd^{3+}$, (d) $Sr_{2.98}Al_{0.02}Si_{0.98}O_5:0.01Ce^{3+}$, $0.01Dy^{3+}$. All the samples were irradiated by β source for 100s.

Figure 3.12. (a) is the thermoluminescence excitation spectra of $Sr_{2.98}Al_{0.02}Si_{0.98}O_5$:$0.01Ce^{3+}$, $0.01Dy^{3+}$. The samples have been excited by a Xe lamp from 200 to 500 nm for 300 s before measuring. (b) The thermoluminescence glow curves of $Sr_{2.98}Al_{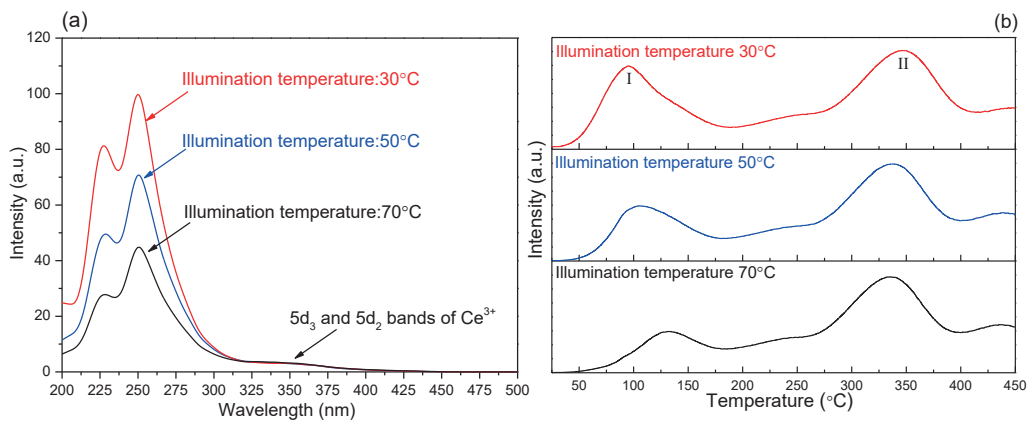0.02}Si_{0.98}O_5$:$0.01Ce^{3+}$, $0.01Dy^{3+}$ illuminated by 260 nm UV light with different illumination temperature. The thermoluminescence excitation spectra were obtained by plotting the integrated TL from 25 to 220 °C as function of the excitation wavelength.

Figure 3.12a shows the TLE spectrum of $Sr_{2.98}Al_{0.02}Si_{0.98}O_5$:$0.01Ce^{3+}$, $0.01Dy^{3+}$ at temperatures of 30, 50, and 70 degrees. It shows three peaks at around 220, 260 and 350 nm. There is no response of the sample when the wavelength is longer than 400 nm, which is different with the PLE spectrum shown in Figure 3.2a. Apparently there is no charging of TL traps from the $5d_1$ level of Ce which indicates that the $5d_1$ excited state is too far away from the conduction band to have significant thermal ionization. A broad band can be observed around 350 nm demonstrating a similar structure as the Ce^{3+} PLE spectra in Figure 3.2a. This suggests that electrons in $5d_3$ and $5d_2$ excited states of Ce^{3+} can be ionized into the conduction band to fill the available traps. This all agrees with the scheme of Figure 3.5 where the $5d_3$ level is in the conduction band and the $5d_2$ level is 0.17 eV below the conduction band. The most intense TLE peak is observed at around 260 nm, which is not observed in the excitation spectrum of Figure 3.2a. Apparently there is an unknown charging defect. Charging might be via its excited state located within the conduction band or via a direct transition from its ground state to the CB. The ground state level is then at most 4.75 eV (260 nm) below the conduction band. Possibly the same defect is responsible for the 380 nm defect emissions in Figure 3.10. The intensity of the 260 nm excitation band decreases with increasing the temperature during the illumination and charging phase from 30 to 70 °C. Figure 3.12b displays the TL spectra after 260 nm illumination. The Tl-spectra are almost the same as in samples without Dy codoping like shown in Figure 3.10b. Peak I relates to Ce^{3+} emission and peak II to host emission. The intensity of peak I to that of peak II decreases with increasing the illumination temperature which is explained by thermal quenching of Ce^{3+} emission (see Figure 3.6b).

3.4 Summary and conclusions

The Sr_3SiO_5 based luminescent materials have been successfully prepared through high temperature solid state reaction. The low temperature photoluminescence has

been used to study the spectroscopy of $Sr_{2.975}Al_{0.025}Si_{0.975}O_5:0.025Ce^{3+}$, $Sr_{2.975}Al_{0.025}Si_{0.975}O_5:0.025Eu^{3+}$ as well as Sr_3SiO_5 host lattice. The results show that the $5d_3$, $5d_2$ and $5d_1$ bands can be observed at 316 nm, 345 nm and 410 nm. Although the $5d_5$ and $5d_4$ bands cannot be confidently assigned in excitation spectra, the average energy of them has been calculated as 198 nm by estimating the centroid shift. After that, the vacuum referred energy level diagram of Sr_3SiO_5 has been derived by using the charge transfer energy of Eu^{3+} and exciton creation energy, which are 3.96 eV and 6.0 eV, respectively. With the help of the VRBE diagram, Nd, Sm, Dy and Tm have been selected as codopants to act as electron traps. The second part discussed the thermoluminescence properties of lanthanides codoped $Sr_{2.98}Al_{0.02}Si_{1-x}O_5:0.01Ce^{3+}$ (lanthanides = Er, Nd, Sm, Dy and Tm). The thermoluminescence glow curves display that Nd^{3+}, Sm^{3+}, Dy^{3+} and Tm^{3+} can work as electron traps and the trap depths for the corresponding divalent ions are 0.90 eV, 1.83 eV, 0.95 eV and 1.15 eV respectively. The thermoluminescence emission spectra reveal that Ce^{3+} acts as the luminescence (recombination) center. $Sr_{2.98}Al_{0.02}Si_{0.98}O_5:0.01Ce^{3+}$, $0.01Dy^{3+}$ appears the sample with the longest afterglow decay time as was demonstrated by the iso-thermal decay spectra. Finally, the thermoluminescence excitation spectra were presented and it was found that the electron traps in $Sr_{2.98}Al_{0.02}Si_{0.98}O_5:0.01Ce^{3+}$, $0.01Dy^{3+}$ can be efficiently charged by 260 nm UV light.

3.5 Acknowledgements

3.6 Reference

1. Van den Eeckhout, K.; Smet, P. F.; Poelman, D., Persistent Luminescence in Eu2+ Doped Compounds a Review. *Materials* **2010**, *3*, 2536-2566.

2. Maldiney, T., et al., The in Vivo Activation of Persistent Nanophosphors for Optical Imaging of Vascularization, Tumours and Grafted Cells. *Nature Material* **2014**, *13*, 418-426.

3. Van den Eeckhout, K.; Poelman, D.; Smet, P., Persistent Luminescence in Non-Eu2+-Doped Compounds: A Review. *Materials* **2013**, *6*, 2789-2818.

4. Lin, Y.; Tang, Z.; Zhang, Z.; Nan, C. W., Anomalous Luminescence in Sr4Al14O25:Eu, Dy Phosphors. *Applied Physics Letters* **2002**, *81*, 996-998.

5. Dorenbos, P., Mechanism of Persistent Luminescence in Sr2MgSi2O7:Eu2+, Dy3+. *Physica Status Solidi (b)* **2005**, *242*, R7-R9.

6. Miyamoto, Y.; Kato, H.; Honna, Y.; Yamamoto, H.; Ohmi, K., An Orange-Emitting, Long-Persistent Phosphor, Ca2Si5N8:Eu2+,Tm3+. *Journal of the Electrochemical Society* **2009**, *156*, J235-J241.

7. Ueda, J.; Kuroishi, K.; Tanabe, S., Bright Persistent Ceramic Phosphors of Ce-Cr-Codoped Garnet Able to Store by Blue Light. *Applied Physics Letters* **2014**, *104*, 101904-101907.

8. Matsuzawa, T., A New Long Phosphorescent Phosphor with High Brightness, SrAl2O4:Eu2+, Dy3+. *Journal of Electrochem Society* **1996**, *143*, 2670-2673.

9. Dorenbos, P., The 5d Level Positions of the Trivalent Lanthanides in Inorganic Compounds. *Journal of Luminescence* **2000**, *91*, 155-176.

10. Setlur, A. A.; Heward, W. J.; Gao, Y.; Srivastava, A. M.; Chandran, R. G.; Shankar, M. V., Crystal Chemistry and Luminescence of Ce3+-Doped Lu2CaMg2(Si,Ge)3O12 and Its Use in Led Based Lighting. *Chemistry of Materials* **2006**, *18*, 3314-3322.

11. Jiang, Z.; Wang, Y.; Wang, L., Enhanced Yellow-to-Orange Emission of Si-Doped Mg3Y2Ge3O12:Ce3+ Garnet Phosphors for Warm White Light-Emitting Diodes. *Journal of the Electrochemical Society* **2010**, *157*, J155-J158.

12. Shimizu, T.; Ueda, J.; Tanabe, S., Optical and Optoelectronic Properties of Ce3+ Doped Mg3Y2(Ge,Si)3O12 Inverse Garnet. *Physica Status Solidi (c)* **2012**, *9*, 2296-2299.

13. Yellow Emitting Γ-Ca2SiO4:Ce3+, Li+ Phosphor for Solid State Lighting Luminescent Properties,Electronic Structure, and White Light-Emitting Diode Application. *Optics Express* **2014**, 20, 2761-2771

14. Kalaji, A.; Mikami, M.; Cheetham, A. K., Ce3+ Activated Γ-Ca2SiO4 and Other Olivine Type Abxo4phosphors for Solid State Lighting. *Chemistry of Materials* **2014**, *26*, 3966-3975.

15. Jang, H. S.; Jeon, D. Y., Yellow-Emitting Sr3SiO5:Ce3+,Li+ Phosphor for White-Light-Emitting Diodes and Yellow-Light-Emitting Diodes. *Applied Physics Letters* **2007**, *90*, 041906-041909.

16. Luo, H.; Liu, J.; Zheng, X.; Han, L.; Ren, K.; Yu, X., Enhanced Photoluminescence of Sr3SiO5:Ce3+ and Tuneable Yellow Emission of Sr3SiO5:Ce3+,Eu2+ by Al3+ Charge Compensation for W-Leds. *Journal of Materials Chemistry* **2012**, *22*, 15887-15893.

17. Bos, A. J. J., Theory of Thermoluminescence. *Radiation Measurements* **2006**, *41, Supplement 1*, S45-S56.

18. Li, Y.; Li, B.; Ni, C.; Yuan, S.; Wang, J.; Tang, Q.; Su, Q., Synthesis, Persistent Luminescence, and Thermoluminescence Properties of Yellow Sr3SiO5:Eu2+,Re3+ (Re=Ce, Nd, Dy, Ho, Er, Tm, Yb) and Orange-Red Sr3-xBaxSiO5:Eu2+, Dy3+ Phosphor. *Chemistry – An Asian Journal* **2014**, *9*, 494-499.

19. Dobrowolska, A.; Bos, A. J. J.; Dorenbos, P., Electron Tunnelling Phenomena in YPO4:Ce,Ln (Ln = Er, Ho, Nd, Dy). *Journal of Physics D: Applied Physics* **2014**, *47*, 335301-335310.

20. Rogers, E. G.; Dorenbos, P., Vacuum Referred Binding Energy of the Single 3d, 4d, or 5d Electron in Transition Metal and Lanthanide Impurities in

Compounds. *ECS Journal of Solid State Science and Technology* **2014**, *3*, R173-R184.

21. Dorenbos, P., Ce3+ 5d-Centroid Shift and Vacuum Referred 4f-Electron Binding Energies of All Lanthanide Impurities in 150 Different Compounds. *Journal of Luminescence* **2013**, *135*, 93-104.

22. Dorenbos, P., Modeling the Chemical Shift of Lanthanide 4f Electron Binding Energies. *Physical Review B* **2012**, *85*.165107-165117

23. Dorenbos, P., 5d-Level Energies of Ce3+ and the Crystalline Environment. Iv. Aluminates and "Simple" Oxides. *Journal of Luminescence* **2002**, *99*, 283-299.

24. Lee, S. P.; Huang, C. H.; Chan, T. S.; Chen, T. M., New Ce3+ Activated Thiosilicate Phosphor for Led Lighting-Synthesis, Luminescence Studies, and Applications. *ACS Appl Mater Interfaces* **2014**, *6*, 7260-7267.

25. Ueda, J.; Aishima, K.; Tanabe, S., Temperature and Compositional Dependence of Optical and Optoelectronic Properties in Ce3+-Doped Y3Sc2Al3-xGaxO12 (x=0, 1, 2, 3). *Optical Materials* **2013**, *35*, 1952-1957.

26. Heinz, W. S., Raman Spectra of Gases. In *Handbook of Raman Spectroscopy*, CRC Press: 2001.

27. Bos, A. J. J.; Dorenbos, P.; Bessière, A.; Lecointre, A.; Bedu, M.; Bettinelli, M.; Piccinelli, F., Study of Tl Glow Curves of YPO4 Double Doped with Lanthanide Ions. *Radiation Measurements* **2011**, *46*, 1410-1416.

28. Nambi, K. S. V.; Bapat, V. N.; Ganguly, A. K., Thermoluminescence of CaSO4 Doped with Rare Earths. *Journal of Physics C: Solid State Physics* **1974**, *7*, 4403-4415.

48

4

Electronic Structure and Site Occupancy of Lanthanide-Doped (Sr, Ca)₃(Y, Lu)₂Ge₃O₁₂ Garnets: A Spectroscopic and First-Principles Study

4.1 Abstract

Photoluminescence excitation (PLE) and emission spectra (PL) of undoped (Sr, Ca)$_3$(Y, Lu)$_2$Ge$_3$O$_{12}$ as well as Eu^{3+} and Ce^{3+} doped samples have been investigated. The PL spectra show that Eu^{3+} enters into both dodecahedral (Ca, Sr) and octahedral (Y, Lu) sites. Ce^{3+} gives two broad excitation bands in the range of 200-450 nm. First-principles calculations for Ce^{3+} on both dodecahedral and octahedral sites provide sets of 5d excited level energies that are consistent with the experimental results. Then the vacuum referred binding energy diagrams for (Sr, Ca)$_3$(Y, Lu)$_2$Ge$_3$O$_{12}$ have been constructed with the lanthanide dopant energy levels by utilizing spectroscopic data. The Ce^{3+} 5d excited states are calculated by first-principles calculations. Thermoluminescence (TL) glow curves of (Ce^{3+}, Sm^{3+}) codoped (Sr, Ca)$_3$(Y, Lu)$_2$Ge$_3$O$_{12}$ samples show a good agreement with the prediction of lanthanide trapping depths derived from the energy level diagram. Finally, the energy level diagram is used to explain the low thermal quenching temperature of Ce^{3+} and the absence of afterglow in (Sr, Ca)$_3$(Y, Lu)$_2$Ge$_3$O$_{12}$.

4.2 Introduction

The spectroscopic properties of lanthanide-doped phosphors depend not only on the energy differences between 4f and 5d states but also on the location of these states relative to the electronic states of the host, i.e. the conduction band (CB) and the valence band (VB) [1].

Lanthanide energy levels are of great interest both for an application and for a theoretical point of view. Thermal quenching of 5d-4f emission occurs when the electron in the 5d excited state like in Ce^{3+} or Eu^{2+} transfers to the conduction band [2-4]. This is not beneficial to LED phosphors since such thermal ionization will dramatically reduce the efficiency of the phosphors at the LED working temperature [5] (~150°C). On the other hand, afterglow phosphors need a relatively low thermal quenching temperature to spontaneously ionize sunlight-excited 5d electrons to the conduction band to be captured by the traps [6-8].

The lanthanide trap depths can be predicted and analyzed by locating the ground state 4f^n levels relative to the host bands [9]. When divalent lanthanide 4f^n ground state levels are close to the CB the corresponding trivalent ions may act as electron-

trapping centers. Bos *et al* confirmed this hypothesis by studying the thermoluminescence of YPO_4:Ce^{3+},Ln^{3+} (Ln= Pr, Nd, Sm, Dy, Ho, Er, Tm and Yb) samples and found that for each lanthanide codopant there is a different trap depth[10]. The trap depth in this case is the distance between divalent lanthanide ground state $4f^n$ levels and the bottom of the CB.

The trivalent lanthanide $4f^n$ ground state levels can be close above the VB, which means that these ions may act as hole-trapping centers. Chakrabarti[11] *et al* reported that samarium acts as a recombination center and cerium as the trapping centre that capture holes after UV irradiation in MgS:Ce^{3+},Sm^{3+}. Recently, Luo[12] *et al* systematically studied the hole trapping and hole release processes in $GdAlO_3$:Ln^{3+}, RE^{3+} (Ln=Sm, Eu and Yb, RE= Ce, Pr and Tb), and found that RE codopants act as the hole-trapping centers where the trap depth relates to the distance between trivalent lanthanide 4f lowest states to the top of the VB.

Initially (Sr, Ca)$_3$(Y, Lu)$_2$Ge$_3$O$_{12}$ garnets doped with Ce^{3+} as the luminescence center and other trivalent lanthanides as electron-trapping center were selected for study with the aim to develop persistent luminescence phosphors. Ce^{3+} in garnet compounds emit in the green to red and have strong absorption of daylight[13-15]. However, the materials turn out not to be good persistent luminescence phosphors. To explain this we determined the electronic structure providing the location of the lanthanide levels within the band gap.

The materials share a normal garnet structure $A_3B_2C_3O_{12}$ (cation occupy 24 c, 16 a, and 24 d), where A, B and C denote dodecahedral (point symmetry 222), octahedral (point symmetry $\bar{3}$) and tetrahedral (point symmetry $\bar{4}$) coordination, respectively[16-17]. The crystal chemistry of garnets is discussed in detail by S. Geller, which covers more than hundreds of garnet compounds[18]. However, few reports are found for this family of garnets. Uhlich *et al* reported that the Eu^{3+} enters the octahedral Y site with an O^{2-}-Eu^{3+} charge transfer band at ~240 nm[19]. Kalaji *et al* studied the room-temperature spectroscopy of Ce^{3+} doped (Sr, Ca)$_3$(Y, Lu)$_2$Ge$_3$O$_{12}$ garnets and concluded that Ce^{3+} enters the dodecahedral site instead of the octahedral one[20]. Kaminskii *et al* mentioned that in the two-cation garnets the RE^{3+} dopant mainly enters the dodecahedral site and in some cases it can also enter the octahedral site[21].

Obviously, something is still not fully clear in this type of materials. For instance, what is the site occupancy of Eu^{3+} and Ce^{3+} in $(Sr, Ca)_3(Y, Lu)_2Ge_3O_{12}$ garnets? Second, where are the Ce^{3+} ground states and the 5d excited states in $(Sr, Ca)_3(Y, Lu)_2Ge_3O_{12}:Ce^{3+}$ with respect to the host valence and conduction bands? Third, how does the bandgap change by replacing the Sr or Y by the smaller Ca or Lu ions and how does this influence the Ce^{3+} 5d bands and Eu^{3+} charge transfer energy?

The objective of this study is to systematically reveal the lanthanide levels in $(Sr, Ca)_3(Y, Lu)_2Ge_3O_{12}$ garnets to answer the above questions. First-principles calculations and the empirical chemical shift model are combined to determine the electronic structure and construct the energy level diagrams showing the lanthanide levels within the band gap[9]. The electronic structures of $(Sr, Ca)_3(Y, Lu)_2Ge_3O_{12}$ host lattices are calculated by using the hybrid density functional theory (DFT) method. The $4f_1$ and $5d_1$ energy levels of Ce^{3+} are calculated by a wave-function-based multireference approach. The low-temperature VUV photoluminescence excitation and emission spectra for the undoped $(Sr, Ca)_3(Y, Lu)_2Ge_3O_{12}$ host lattices and the photoluminescence for Ce^{3+} or Eu^{3+} doped samples are presented. The experimental results for Ce^{3+} doped samples are used to compare with theoretical calculations to identify the Ce^{3+} site occupancy and the 5d levels. Low-temperature thermoluminescence measurements are carried out for (Ce^{3+}, Sm^{3+}) codoped samples to locate the Sm^{2+} ground state. Results are used to construct the energy level diagram of $(Sr, Ca)_3(Y, Lu)_2Ge_3O_{12}$ showing the locations of the lanthanide states within the band gap.

4.3 Experimental and theoretical methods

4.3.1 Experimental details
All starting materials were purchased from Sigma-Aldrich and used without further treatment. The appropriate stoichiometric mixture of GeO_2 (99.99%), $SrCO_3$ (99.99%), $CaCO_3$ (99.99%) and rare earth oxides with the purity of 5 N (99.999%) were weighed according to the chemical formula and milled homogeneously with the help of acetone. Then the powders were synthesized at 1300 °C for 12 h in a corundum crucible in an atmosphere of N_2. After cooling, the as-prepared materials were grinded again and synthesized at 1300 °C for another 12 h in the same atmosphere. Finally, the obtained compounds were cooled to room temperature.

All powders were checked with a PANalytical XPert PRO X-ray diffraction system with a Co Kα (λ = 0.178901 nm) X-ray tube (45 kV, 40 mA). The photoluminescence excitation (PLE) and photoluminescence emission (PL) measurements were measured with a setup that consists of an UV/vis branch with a 500 W Hamamatsu CW Xe lamp and Gemini 180 monochromator and a VUV/UV branch using a deuterium lamp with an ARC VM502 vacuum monochromator. The PerkinElmer MP-1913 photomultiplier was exploited as a detector connected at the exit slit of a Princeton Acton SP2300 monochromator. The sample was placed in an evacuated sample chamber.

Low-temperature thermoluminescence (LTTL) measurements (90-450 K) were recorded with a sample chamber operating under vacuum (P = 10^{-7} mbar), a ^{90}Sr/^{90}Y beta irradiation source having a dose rate of ∼0.4 mGy s^{-1} and a PerkinElmer channel PM tube (MP-1393). Liquid nitrogen was used as a cooling medium. A 490 nm bandpass filter (490FS10-50) was placed between the sample and PMT during the measurements to select only Ce^{3+} emission. The peak intensities were corrected for mass differences.

4.3.2 Computational details

The Ce-doped $Sr_3Y_2Ge_3O_{12}$ and $Ca_3Y_2Ge_3O_{12}$ crystals were modeled by using a unit cell containing 160 atoms, in which one of the 16 Y atoms or one of the 24 Sr or Ca atoms was replaced by a Ce. The lattice parameters and atomic coordinates of the doped unit cell were optimized by periodic DFT calculations using a hybrid exchange-correlation functional in the PBE0 scheme, as implemented in the VASP code[22-23]. The excess charge of Ce^{3+} on the Sr^{2+} or Ca^{2+} site was compensated by introducing a uniform background charge density, and the spurious Coulomb interaction in charged supercells is expected to be small due to the large size of the supercells[24]. The electrons of Ce ($5s^25p^64f^15d^16s^2$), Ca ($3s^23p^64s^2$), Sr ($4s^24p^64s^2$), Y ($4s^24p^64d^15s^2$), Ge ($4s^24p^2$) and O ($2s^22p^4$) were treated as valence electrons, and their interactions with the respective cores were described by the projected augmented wave (PAW) method[25]. The geometry optimizations were performed until the total energies and the Hellmann−Feynman forces on the atoms converged to 10^{-6} eV and 0.01 eV Å^{-1}, respectively. Due to the large size of the systems and the high computational cost of hybrid DFT with plane wave basis, only one k-point (Γ point) was used to sample the Brillouin zone, with a cutoff energy of 530 eV for the plane wave basis.

The $4f_1$ and $5d_1$ energy levels of Ce^{3+} were computed with a wave-function-based embedded cluster approach. On the basis of the atomic structures optimized by hybrid DFT, the Ce-centered clusters were constructed, each comprising the central Ce^{3+}, the oxygen ions in the first coordination shell, and the closest Ge^{4+} ions in the second coordination shell. Their immediate surroundings within a sphere of radius 10.0 Å were represented by several hundreds of *ab initio* model potentials (AIMPs)[26] and the remainder of the surroundings were simulated by tens of thousands of point charges at lattice sites, which are generated with Lepetit's method[27]. Wave-function-based CASSCF/CASPT2 calculations with the spin-orbit effect were then carried out to obtain the $4f^1$ and $5d^1$ energy levels of Ce^{3+} by using the program MOLCAS[28]. In the CASSCF calculations, a [4f, 5d, 6s] complete active space was adopted, and in the CASPT2 calculations, the dynamic correlation effects of the Ce^{3+} 5s, 5p, 4f, 5d electrons and the O^2 2s, 2p electrons were considered. Further details about the basis sets can be found in Refs. 29-31.

4.4 Results

4.4.1 X-Ray diffraction and photoluminescence spectroscopy of $(Sr, Ca)_3(Y, Lu)_2Ge_3O_{12}$

XRD patterns of synthesized $(Sr, Ca)_3(Y, Lu)_2Ge_3O_{12}$ phosphors are shown in Figure 4.1. All samples are of single phase and match very well with the $Sr_3Y_2Ge_3O_{12}$ reference card (No. 1408217) due to their same crystal structure (space group: Ia-3d). A slight shift of the XRD peaks can be observed in Figure 4.1b due to different lattice parameters among the as-prepared materials.
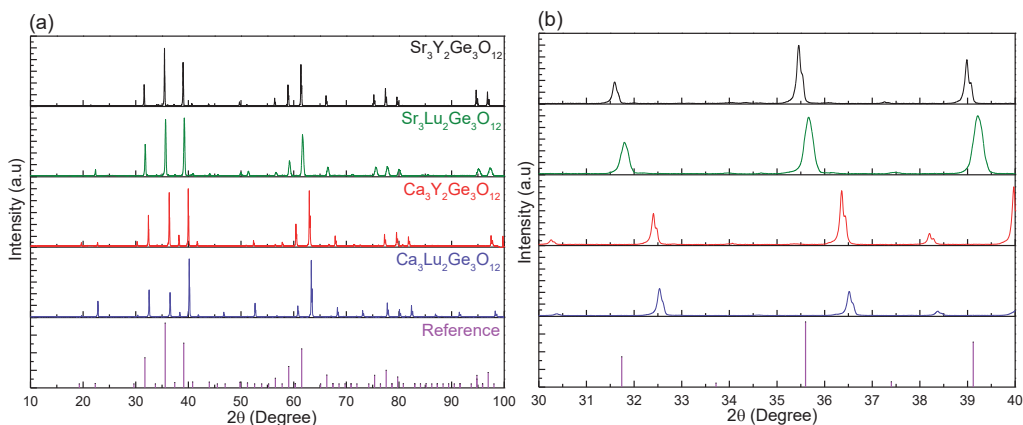
Figure 4.1. (a) XRD patterns of the as-prepared samples of $Sr_3Y_2Ge_3O_{12}$, $Sr_3Lu_2Ge_3O_{12}$, $Ca_3Y_2Ge_3O_{12}$ and $Ca_3Lu_2Ge_3O_{12}$. (b) Detailed XRD patterns in the range from 30 to 40°.

Figure 4.2 shows the low-temperature VUV excitation and emission spectra of $(Sr, Ca)_3(Y, Lu)_2Ge_3O_{12}$ host lattices. The host excitation maxima of $Sr_3Y_2Ge_3O_{12}$ and $Sr_3Lu_2Ge_3O_{12}$ are both reached at 5.9 eV (210 nm) indicating that they have the same bandgap. The reason is that $Sr_3Y_2Ge_3O_{12}$ and $Sr_3Lu_2Ge_3O_{12}$ samples have very close lattice parameters, and it can be observed from Figure 4.1b that the XRD peak positions for these two samples are at almost the same position. For the $Ca_3Y_2Ge_3O_{12}$ and $Ca_3Lu_2Ge_3O_{12}$, the exciton creation energy is 6.1 eV (200 nm). The emissions from 300 to 400 nm of the $(Sr, Ca)_3(Y, Lu)_2Ge_3O_{12}$ host lattices shown in Figure 4.1b are all from a sort of charge transfer emission like host exciton or defect-trapped exciton emission. However, the precise origin is unknown.
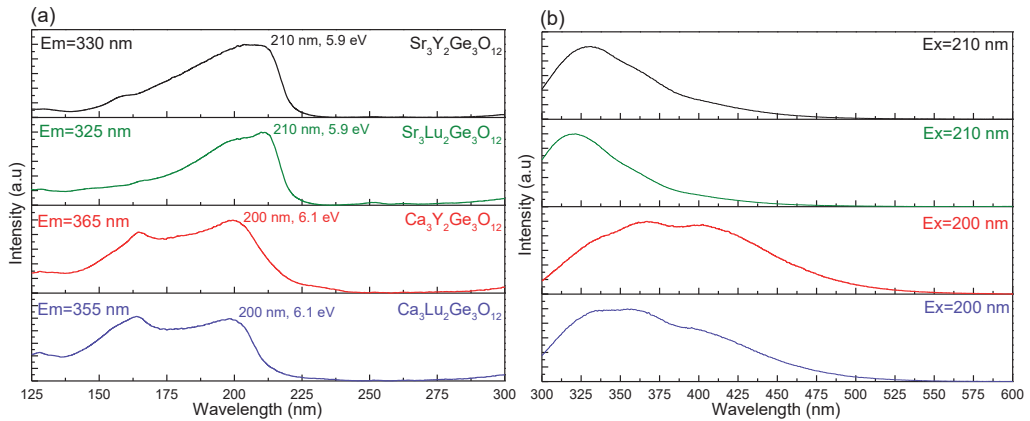
Figure 4.2. (a) PLE and (b) PL spectra of $Sr_3Y_2Ge_3O_{12}$, $Sr_3Lu_2Ge_3O_{12}$, $Ca_3Y_2Ge_3O_{12}$ and $Ca_3Lu_2Ge_3O_{12}$ host lattices. The spectra were measured by deuterium lamp excitation. The excitation spectra were recorded at the emission bands maximum and the emission spectra were excited at the excitation maxima, which are shown in the figure legend. All measurements were performed at 10 K.

Figure 4.3 shows the photoluminescence excitation and emission spectra of Eu^{3+} single doped $Sr_3Y_2Ge_3O_{12}$. There are two different excitation bands at 280 nm (hereafter referred as the charge transfer band CT) and 235 nm (hereafter referred as the near defect exciton band NDE) when monitored at 610 nm and 597 nm emission, respectively. The reasons for assignments will become clear in the

Discussion section. Typical Eu^{3+} line emission with different $^5D_0$-$^7F_1$ and $^5D_0$-$^7F_2$ relative intensity is found with different excitation energy. The $^5D_0$-$^7F_2$ hypersensitive forced electronic-dipole transition is dominating when excited by 280 nm UV irradiation. This indicates that the Eu^{3+} ions are at a non-inversion symmetry site[32]. On the other hand, the $^5D_0$-$^7F_1$ magnetic-dipole transition is dominating when excited by 235 nm UV light, indicating the Eu^{3+} ions at an inversion symmetry site[32].
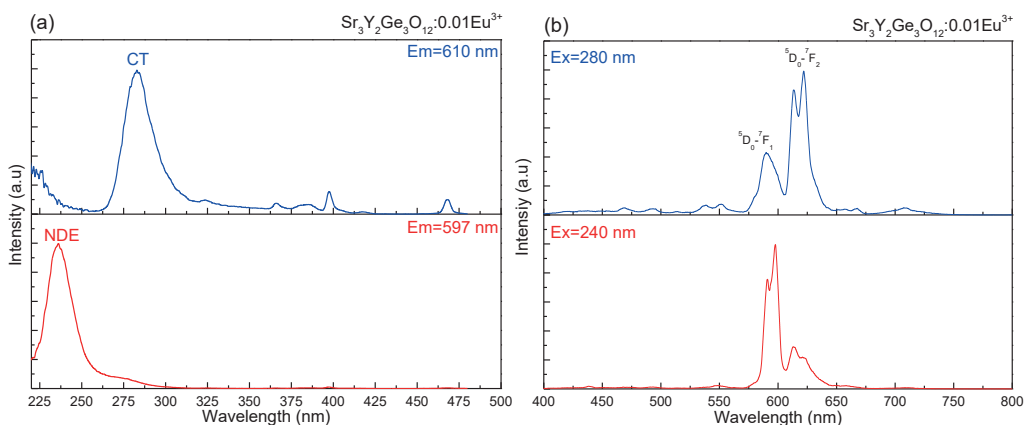
Figure 4.3. Site-selective excitation (a) and emission (b) spectra of $Sr_3Y_2Ge_3O_{12}$:0.01Eu^{3+}. All measurements were performed at RT.

Figures S4.1, S4.2, and S4.3 show the two excitation and emission spectra for the other three garnet compounds. They also indicate that the Eu^{3+} dopants are at two different sites. Table 4.1 lists the wavelength maxima of the CT and NDE bands. We observe that the CT band shifts to higher energy from $Sr_3Y_2Ge_3O_{12}$ to $Ca_3Lu_2Ge_3O_{12}$, while the NDE band stays at almost the same position.

Table 4.1 The excitation band maxima of Eu^{3+} single doped samples

	CT-band	NDE-band
$Sr_3Y_2Ge_3O_{12}$:Eu^{3+}	280 (4.43 eV)	235 (5.27 eV)
$Sr_3Lu_2Ge_3O_{12}$:Eu^{3+}	265 (4.68 eV)	232 (5.34 eV)
$Ca_3Y_2Ge_3O_{12}$:Eu^{3+}	260 (4.77 eV)	235 (5.27 eV)
$Ca_3Lu_2Ge_3O_{12}$:Eu^{3+}	255 (4.86 eV)	233 (5.32 eV)

Figures 4.4 and 4.5 show the PLE and PL spectra of Ce^{3+} single-doped $(Sr, Ca)_3(Y, Lu)_2Ge_3O_{12}$ phosphors recorded at 10 K. The PLE and PL spectra of $Sr_3Y_2Ge_3O_{12}:Ce^{3+}$ measured at room temperature are displayed in Figure S4.4, and they do not show much difference from the low-temperature spectra.
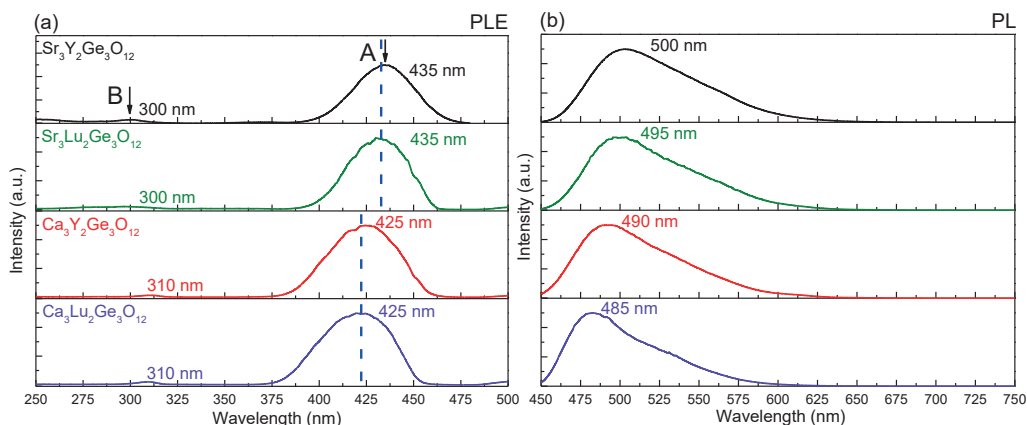
Figure 4.4. (a) PLE and (b) PL spectra of $Sr_3Y_2Ge_3O_{12}:0.01Ce^{3+}$, $Sr_3Lu_2Ge_3O_{12}:0.01Ce^{3+}$, $Ca_3Y_2Ge_3O_{12}:0.01Ce^{3+}$, and $Ca_3Lu_2Ge_3O_{12}:0.01Ce^{3+}$. The excitation spectra were recorded at the emission peak maxima, and the emission spectra were excited at the Band A peak maxima. All the measurements were carried out at 10 K.
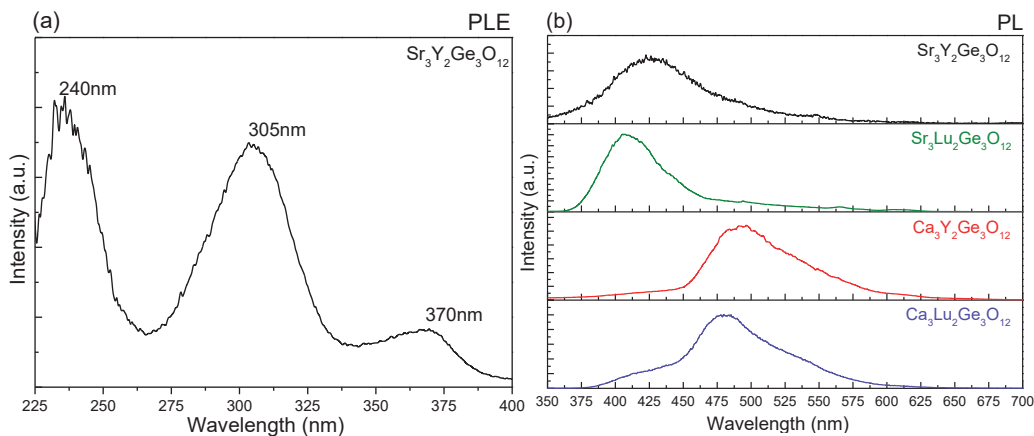
Figure 4.5. (a) PLE spectrum of $Sr_3Y_2Ge_3O_{12}:0.01Ce^{3+}$ monitored at 425 nm. (b) PL spectra of $Sr_3Y_2Ge_3O_{12}:0.01Ce^{3+}$, $Sr_3Lu_2Ge_3O_{12}:0.01Ce^{3+}$, $Ca_3Y_2Ge_3O_{12}:0.01Ce^{3+}$ and $Ca_3Lu_2Ge_3O_{12}:0.01Ce^{3+}$ excited by 300 nm UV irradiation. All the measurements were carried out at 10 K.

The excitation spectra in Figure 4.4 ranging from 250 to 500 nm are composed of two bands: one intense band in the blue range (420-435 nm, Band A) and one weak band in the UV range (300-315 nm, Band B). A broad emission band centered at ~500 nm can be observed for all the samples when excited at Band A maxima, and it is composed of the two unresolved Ce^{3+} $5d_1$-$^2F_{5/2}$ and $5d_1$-$^2F_{7/2}$ emission bands. When excited by 300 nm UV irradiation, a new band centered at ~ 425 nm appears for all samples shown in Figure 4.5b. A representative excitation spectrum of $Sr_3Y_2Ge_3O_{12}$:Ce^{3+} monitored at 425 nm emission is shown in Figure 4.5a. It seems that Ce^{3+} occupies two different sites.
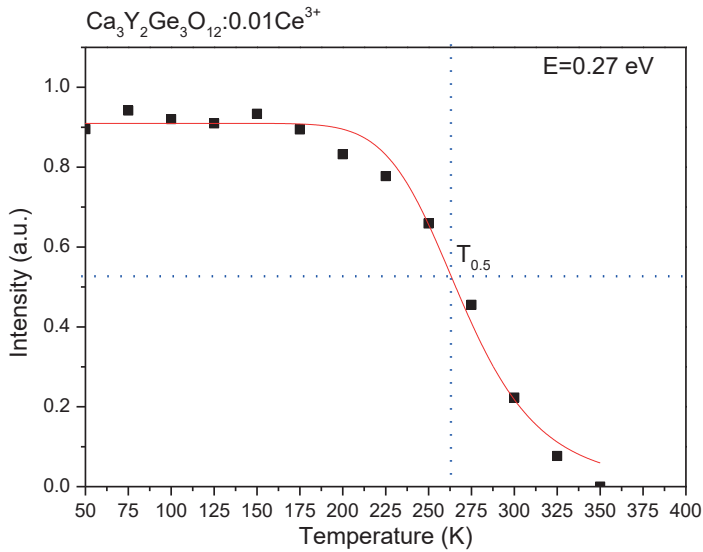
Figure 4.6. Temperature dependence of $Ca_3Y_2Ge_3O_{12}$:$0.01Ce^{3+}$. The excitation monometer was set as 425 nm. The solid curve through the data is a fitted curve. The measurement was carried out by a liquid helium cryostat.

Figure 4.6 shows the thermal quenching curve of $Ca_3Y_2Ge_3O_{12}$:$0.01Ce^{3+}$ from 50 to 350 K. The quenching temperature ($T_{0.5}$) where intensity has reduced by 50% is at ~265 K. The activiation energy for thermal quenching can be derived from[33]:

$$I(T) = \frac{I(0)}{1 + C\exp(-\frac{E}{kT})} \qquad 4.1$$

Where $I(T)$ and $I(0)$ is the intensity at temperature T and 50 K, k is the Boltzmann constant. A fit through the data in Figure 4.6, as indicated by the solid curve provides $E = 0.27$ eV, which is indicative for the energy difference between the $5d^1$ state and the bottom of the CB.

4.4.2 Thermoluminescence glow curves of $(Sr, Ca)_3(Y, Lu)_2Ge_3O_{12}:Ce^{3+},Sm^{3+}$
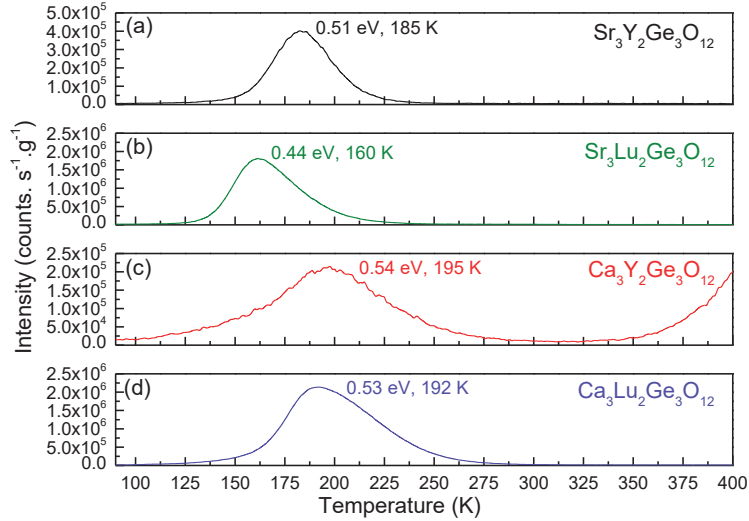
Figure 4.7. Low-temperature thermoluminescence (LTTL) glow curves of (a) $Sr_3Y_2Ge_3O_{12}:0.01Ce^{3+},0.01Sm^{3+}$, (b) $Sr_3Lu_2Ge_3O_{12}:0.01Ce^{3+},0.01Sm^{3+}$, (c) $Ca_3Y_2Ge_3O_{12}:0.01Ce^{3+},0.01Sm^{3+}$ and (d) $Ca_3Lu_2Ge_3O_{12}:0.01Ce^{3+},0.01Sm^{3+}$. All measurements were carried out with the low-temperature TL setup from 90 to 450 K after 1600 s irradiation by its β source. The heating rate was 1 K s^{-1} for all TL-recordings. The TL glow curves were measured with a 490 nm bandpass filter (490FS10-50) to transmit the 5d-4f Ce^{3+} emission (at ~ 500 nm).

In Figure 4.7 the calibrated LTTL glow curves from Ce^{3+} 5d-4f emission in (Ce^{3+}, Sm^{3+}) co-doped $(Sr, Ca)_3(Y, Lu)_2Ge_3O_{12}$ are shown. Several co-doping combinations of (Ce^{3+}, Sm^{3+}), (Ce^{3+}, Eu^{3+}), (Ce^{3+}, Tm^{3+}) and (Ce^{3+}, Yb^{3+}) were tried but only the (Ce^{3+}, Sm^{3+}) combination gives TL within this measurement range. The temperature T_m where TL is maximum depends on the host lattice and ranges from 160 K for $Sr_3Lu_2Ge_3O_{12}$: Ce^{3+}, Sm^{3+} to 200 K for $Ca_3Y_2Ge_3O_{12}$: Ce^{3+}, Sm^{3+}.

The trap depth E of the Sm^{3+} trapping center in (Ce^{3+}, Sm^{3+}) codoped (Sr, Ca)$_3$(Y, Lu)$_2$Ge$_3$O$_{12}$ was determined using the T_m from Figure 4.7 and employing[34]

$$\frac{\beta E}{kT_m^2} = s \exp(-\frac{E}{kT_m}) \qquad\qquad 4.2$$

where β = 1 K s^{-1} is the heating rate; k is the Boltzmann constant; and s is the frequency factor[34]. The frequency factor s, which is related to the host lattice vibrational mode, is estimated using the most intense vibrational energy for trigonal GeO$_2$ ($P3_221$) of 444 cm^{-1} (1.3×10^{13} s^{-1})[35-36], where Ge has the same coordination number as in (Sr, Ca)$_3$(Y, Lu)$_2$Ge$_3$O$_{12}$ (for both CN=4). We assumed a similar value for our samples due to a similar [GeO$_4$]$^{4-}$ group present. The estimated trap depth values can be found in Figure 4.7.

4.4.3 First principle calculations

The atomic structures of the representative pure Sr$_3$Y$_2$Ge$_3$O$_{12}$ and Ca$_3$Y$_2$Ge$_3$O$_{12}$ unit cells were optimized using hybrid DFT with the standard PBE0 functional containing 25% HF exchange. The calculated lattice constants were compared with the experimental ones reported in the literature (Table S4.1)[37-38].

On the basis of the optimized atomic structures, the band gaps were calculated by using the same DFT functional with a modified PBE0 hybrid functional. The percentage of HF exchange was changed until optimal correspondences with the experimental values are obtained, with 32% HF exchange[39-40]. The modified PBE0 functional gives band gap values of 6.33 eV for Sr$_3$Y$_2$Ge$_3$O$_{12}$ and 6.53 eV for Ca$_3$Y$_2$Ge$_3$O$_{12}$, to be compared with the experimental values (6.37 for Sr$_3$Y$_2$Ge$_3$O$_{12}$ and 6.60 eV for Ca$_3$Y$_2$Ge$_3$O$_{12}$). Those experimental values are from the exciton creation peaks in Figure 4.2. To account for the exciton binding energy, a mobility band gap of 1.08*E$_{ex}$ was assumed [9].

Figure 4.8 shows the total and orbital-projected densities of states (DOSs) for the Sr$_3$Y$_2$Ge$_3$O$_{12}$ and Ca$_3$Y$_2$Ge$_3$O$_{12}$ unit cells. The Fermi levels at the top of the valence band are set at 0 eV. The VB of both samples is formed primarily by O 2p orbitals. The bottom of the conduction band for both compounds is composed of discrete peaks, for which an enlarged view is shown in the insets. The CB edge state is constituted by a small peak at 6.33 eV for Sr$_3$Y$_2$Ge$_3$O$_{12}$ and 6.53 eV for Ca$_3$Y$_2$Ge$_3$O$_{12}$, which is mainly derived from s-character states of Ge and O atoms

and d-character states of Y and Sr/Ca atoms. The other discrete peaks have additional contributions from p-character states of O and Ge atoms. Above these, the conduction band consists mainly of Y d, Sr/Ca d, and O p states.

Relative to the DOS at the energy of the deeper Y 4s states (below -40 eV) in $Sr_3Y_2Ge_3O_{12}$, we observe that the valence band of $Ca_3Y_2Ge_3O_{12}$ moves downward by 0.13 eV, while the conduction band moves upward by 0.07 eV, giving rise to a 0.2 eV larger band gap.
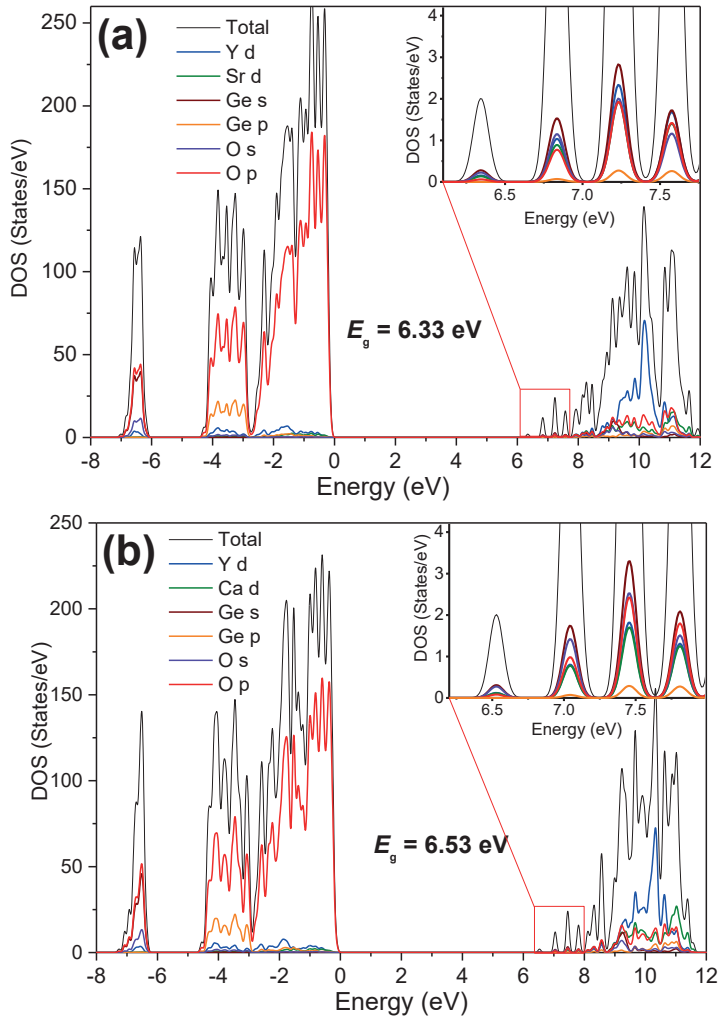
Figure 3.8. Total and orbital-projected DOSs for the (a) $Sr_3Y_2Ge_3O_{12}$ and (b) $Ca_3Y_2Ge_3O_{12}$ unit cells calculated by DFT with the PBE0 hybrid functional containing 32% HF exchange and a 2×2×2 k-point grid to sample the Brillouin zone. The enlarged views of the DOS for the edge of the conduction bands are shown in the inset.

Table 4.2. Calculated energy levels of $4f^1$ and $5d^1$ configurations for the Ce^{3+} in $Sr_3Y_2Ge_3O_{12}$ and $Ca_3Y_2Ge_3O_{12}$ at different sites. All the units are wavenumber (cm^{-1}).

	$Sr_3Y_2Ge_3O_{12}$				$Ca_3Y_2Ge_3O_{12}$			
	Ce_{Sr}	5d->4f intensities	Ce_Y	5d->4f intensities	Ce_{Ca}	5d->4f intensities	Ce_Y	5d->4f intensities
$4f_1$	0		0		0		0	
$4f_2$	124		1151		204		1204	
$4f_3$	881		1276		879		1283	
$4f_4$	2263		2378		2370		2372	
$4f_5$	2380		3558		2384		3586	
$4f_6$	2866		3669		2882		3735	
$4f_7$	3668		4293		3844		4356	
$5d_1$	26423	1.00	24446	1.00	26830	1.00	23828	1.00
$5d_2$	33791	0.09	25049	0.84	32437	0.44	24443	0.54
$5d_3$	43869	1.07	26124	0.05	46196	1.16	25797	0.14
$5d_4$	48218	0.11	58522	0.20	48478	0.26	58728	0.15
$5d_5$	51756	0.28	58530	0.25	51763	0.22	58870	0.26
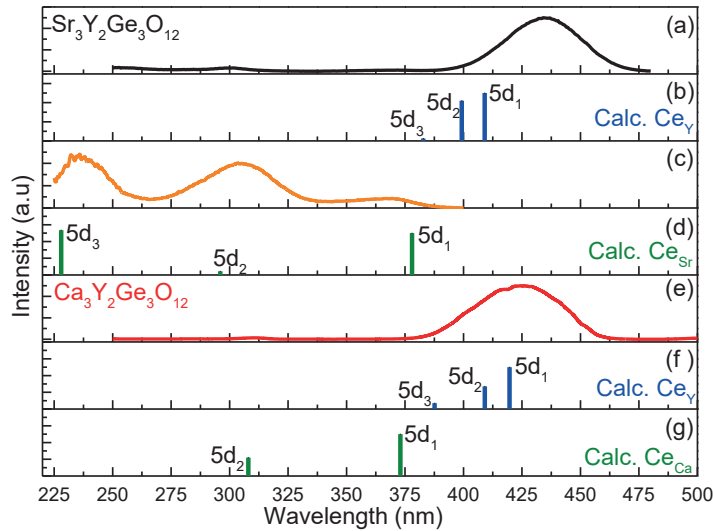
Figure 4.9. Schematic representation of the calculated energies of the 4f-5d transitions of Ce^{3+} on the octahedral (Y) and the dodecahedral site (Sr/Ca) sites for $Sr_3Y_2Ge_3O_{12}$ and $Ca_3Y_2Ge_3O_{12}$. (a) PLE spectrum of $Sr_3Y_2Ge_3O_{12}$:$0.01Ce^{3+}$ monitored at 500 nm. (b) Calculated Ce^{3+} 5d levels for $Sr_3Y_2Ge_3O_{12}$:$0.01Ce^{3+}$ at the Y site. (c) PLE spectrum of $Sr_3Y_2Ge_3O_{12}$:$0.01Ce^{3+}$ monitored at 425 nm. (d) Calculated Ce^{3+} 5d levels for $Sr_3Y_2Ge_3O_{12}$:$0.01Ce^{3+}$ at the Sr site. (e) PLE spectrum of $Ca_3Y_2Ge_3O_{12}$:$0.01Ce^{3+}$ monitored at 490 nm. (f) Calculated Ce^{3+} 5d levels for $Ca_3Y_2Ge_3O_{12}$:$0.01Ce^{3+}$ at the Y site. (g) Calculated Ce^{3+} 5d levels for $Ca_3Y_2Ge_3O_{12}$:$0.01Ce^{3+}$ at the Ca site.

The Ce^{3+} $4f \rightarrow 5d_{1-5}$ transition energies were calculated by wave-function-based CASSCF/CASPT2 functions with spin-orbit coupling. The relative intensity of the 5d-4f transitions are calculated by RASSI−SO wave functions and the energies at the spin-orbit level[41]. Calculations were performed for Ce on the dodecahedral Sr and Ca site and for Ce on the octahedral Y site. The results are listed in Table 4.2, and a comparison with experimental data from Figure 4.4a and 4.5a are shown in Figure 4.9. For Ce^{3+} in octahedral and dodecahedral sites, the two sets of calculated energy levels are quite different both for 4f and 5d level energies.

4.5 Discussion

We will first deal with the question raised in the Introduction regarding the site occupancy followed by the questions regarding location of the lanthanide levels with respect to the host bands and how that changes with type of host garnet.

4.5.1 Eu^{3+} charge transfer band and the site occupancy

The Eu^{3+} charge transfer (CT) energy defines the energy to transfer an electron from the top of the valence band to Eu^{3+} which then becomes divalent[42]. Therefore, the Eu^{3+} CT energy provides the location of the Eu^{2+} ground state above the VB[43]. The vacuum referred electron binding energy in the Eu^{2+} ground state appears within the chemical shift model always near -4 eV in oxides [39, 40]. This means that the Eu^{3+} CT energy gives direct information about the position of the VB maximum. The first principle calculation showed that the VB of $Ca_3Y_2Ge_3O_{12}$ moves downward by 0.13 eV with respect to that of $Sr_3Y_2Ge_3O_{12}$ if aligned by the Y 4s states. This calculation is consistent with Table 4.1 where the excitation bands in column 2 shift toward about 0.1-0.2 eV higher energy when Sr is replaced by the smaller Ca or Y by the smaller Lu. Therefore, we assign the 280 nm band in Figure 3.3 as the CT band and the same for Figure S4.1, S4.2 and S4.3. The excitation

band in column three of Table 4.1 that remains at almost the same position is assigned to a near defect exciton (NDE) band.

For Eu^{3+} we found evidence in Figure 4.3 and S4.1-S4.3 for emission from a site with and without inversion symmetry. In the $(Sr, Ca)_3(Y, Lu)_2Ge_3O_{12}$ host lattice, the dodecahedral site is the noninversion site (due to the 222 point symmetry) while the octahedral site is the site with the inversion symmetry (due to the $\bar{3}$ point symmetry). This explains the difference relative intensity of $^5D_0$-$^7F_1$ and $^5D_0$-$^7F_2$ transition. On the other hand, when the trivalent Eu^{3+} enters into the divalent site, intrinsic charge compensation is needed. The extra positive charge introduced by Eu^{3+} may generate defects like interstitial oxygen or cation vacancies (V_{Sr} or V_Y) that will change the Sr (Ca)-O bond length and the polyhedral shape surrounding Sr (Ca), leading to a noninversion symmetry environment.

4.5.2 Ce^{3+} 4f-5d excited levels and site occupancy

Kalaji et al[20] attribute the excitation bands in the UV and blue regions as shown in Figure 4.4 to the transitions from the $^2F_{5/2}$ ground state to the lowest two 5d excited states from Ce^{3+} assumed to be located at the dodecahedral site. This was motivated by the observation that replacing Y^{3+} with Lu^{3+} barely affects the excitation spectrum and only slightly blue shifts the emission[20]. The one-site occupancy hypothesis cannot explain the extra emission band centered at ~425 nm when excited by 300 nm UV light (Figure 4.5). We attribute the 300 nm excitation band and the blue emission bands to a second Ce^{3+} site. In order to confirm this, the theoretical Ce^{3+} 5d excited states were calculated to analyze the Ce^{3+} site occupancy and excitation spectra.

Table 4.2 compiles the calculated Ce^{3+} 5d energies at the two different sites and Figure 4.9 visualizes it. From the correspondence between experiment and calculations we attribute the lowest broad energy excitation band (Band A) observed experimentally to the triplet $4f_1 \rightarrow 5d_{1-3}$ transitions of Ce^{3+} located at the octahedral site. The three 4f $\rightarrow$ 5d transitions merge into one single broad excitation band. The crystal field splitting between the $5d_1$ and $5d_5$ level for Ce^{3+} at this site is calculated as about 34100 cm^{-1} (4.22 eV) and 35050 cm^{-1} (4.34 eV) for $Sr_3Y_2Ge_3O_{12}$ and $Ca_3Y_2Ge_3O_{12}$. We note that discrepancies exist between the calculated and experimental $4f_1 \rightarrow 5d_{1-3}$ transitions of Ce^{3+}, which could be due to errors in the calculated local structure of Ce^{3+} at the Y^{3+} site of $Sr_3Y_2Ge_3O_{12}$.

64

The weak higher energy excitation band (Band B) in Figure 4.4 cannot be assigned to the doublet e-band for Ce^{3+} on an octahedral site which is predicted at much higher energy according to the calculation (Table 4.2). Next to band B, Figure 4.5a reveals two other excitation bands when monitoring emission at 425 nm in $Sr_3Y_2Ge_3O_{12}$:Ce^{3+}. Based on the agreement with the calculated energies for the 4f-5d bands for Ce on the dodecahedral site in Figure 4.9c and 4.9d all three excitation bands and the ~425nm emission band are attributed to Ce^{3+} on the dodecahedral site. The calculated data explain why the Ce^{3+} 4f → $5d_{4-5}$ transitions for Ce^{3+} on both sites are not experimentally observed because excitation energies are higher than the bandgap energy.

In Figure 4.4, the $5d_1$ band for Ce in the octahedral site blue shifts from 435 to 425 nm, while the $5d_2$ band for Ce in the dodecahedral site red shifts from 300 to 310 nm for $Sr_3Y_2Ge_3O_{12}$:Ce^{3+} and $Ca_3Y_2Ge_3O_{12}$:Ce^{3+}. Applying the empirical crystal field splitting equation, $\varepsilon_{cfs}=\beta_{poly}R^{-2}$, where β_{poly} refers to the type of polyhedron that surrounds Ce^{3+} and R means the average bond length of Ce^{3+} to the nearby bonded anions (O^{2-} here)[44]. We know that for a certain polyhedron type, the shorter the bond length the larger the crystal field splitting will be. Table S4.2 shows that the bond length of Y-O in $Ca_3Y_2Ge_3O_{12}$ (2.3330 Å) is longer than that in $Sr_3Y_2Ge_3O_{12}$ (2.2494 Å). This suggests that the Ce^{3+} CFS at the octahedral site in $Ca_3Y_2Ge_3O_{12}$ will be smaller than in $Sr_3Y_2Ge_3O_{12}$, leading the blue shift of the A band. The Ca (Ce)-O average bond length in $Ca_3Y_2Ge_3O_{12}$ (2.5150 Å) is shorter than of Sr (Ce)-O (2.6174 Å), and apparently a stronger CFS leads to the red shift of the B band.

4.5.3 Energy level diagrams of $(Sr, Ca)_3(Y, Lu)_2Ge_3O_{12}$

We intend to construct a diagram where the binding energy of an electron in lanthanide defect states and in the host valence band and conduction band states can be compared with respect to one and the same energy reference. Usually, like in XPS and UPS studies and in ab initio and full-principle calculations[45-46], energies are referred to the top of the valence band which is then set as the zero of energy like in Figure 4.8 of this work. However, with such approach one cannot relate the binding energies in different compounds, like the four garnets of this work, to a common reference of energy. There are only a few solutions to this problem. In the field of semiconductor science the valence band offset at the heterojunction of two compounds can be determined[47-48]. In the field of

electrochemistry, valence band energies can be related to the standard hydrogen potential[49-50]. In the field of luminescence science, the chemical shift model, was developed in 2012 to construct a vacuum referred binding energy (VRBE) diagram that makes it possible to compare the binding at the VB maximum in different compounds with respect to a same reference energy. VRBE is defined as the energy needed to bring an electron from a level in the diagram to the vacuum outside the sample. The energy at rest in vacuum or vacuum level is then defined as energy zero. Further details about the VRBE diagram can be found in Refs. 1 and 9.
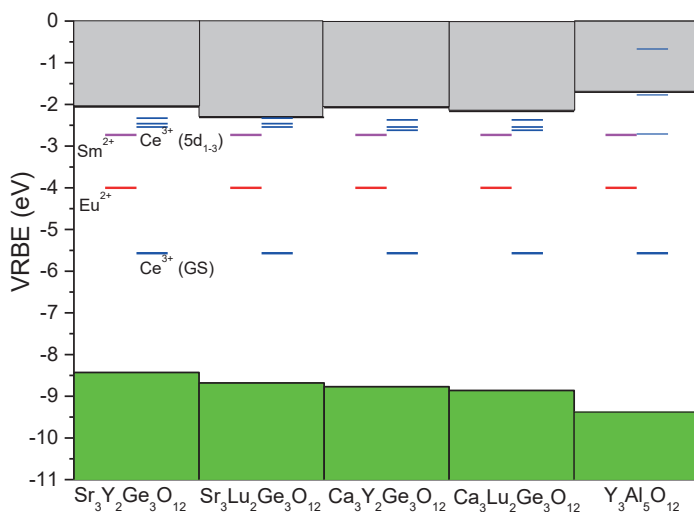
Figure 4.10. VRBE diagram of $(Sr, Ca)_3(Y, Lu)_2Ge_3O_{12}$ and $Y_3Al_5O_{12}$ with location of Ce^{3+}, Eu^{2+}, and Sm^{2+} levels.

Figure 4.10 shows stacked VRBE diagrams for $(Sr, Ca)_3(Y, Lu)_2Ge_3O_{12}$ with location of Ce^{3+}, Eu^{2+}, and Sm^{2+} levels. The detailed VRBE diagrams with all lanthanide impurity levels are shown in Figure S4.5 in the Supporting Information. The data used to construct the diagrams are listed in Table 4.3. We adopted a value of 6.73 eV for the so-called U-parameter in the chemical shift model for all four garnet compounds in this work. This translates to a VRBE value of -3.98 eV for Eu^{2+}, -2.73 eV for Sm^{2+}, and -5.42 eV for Ce^{3+} [51-52]. The charge transfer energy of Eu^{3+} in $(Sr, Ca)_3(Y, Lu)_2Ge_3O_{12}$ as was shown in Table 4.1 then provides the energy at the top of the VB. The decrease of the charge transfer energy of Eu^{3+} implies that the valence band energy moves upward. The bandgap energy was

obtained from Figure 4.2 by adding 8% to the exciton banding energy in order to account for the electron hole binding energy in the exciton. The VRBE in the 5d states of Ce^{3+} was obtained by adding the calculated 5d energies in Table 4.2 for octahedral Ce^{3+} to the ground state energies. The VRBE in the Ce^{3+} 5d levels for $Sr_3Lu_2Ge_3O_{12}$ and $Ca_3Lu_2Ge_3O_{12}$ are the same as in $Sr_3Y_2Ge_3O_{12}$ and $Ca_3Y_2Ge_3O_{12}$, respectively, due to similar excitation spectra. The $Y_3Al_5O_{12}$ VRBE diagram is added for comparison and the data comes from ref.53.

Inspecting the VRBE for the valence band and the conduction band of $(Sr, Ca)_3(Y, Lu)_2Ge_3O_{12}$, Figure 4.10 shows that the VB maxima go downwards while the CB minima go slightly upward except for $Sr_3Lu_2Ge_3O_{12}$ with decreasing the unit cell volume. The binding energies of the electrons in anions usually increase when the bond length to the coordinating ions decreases, which is a manifestation of the Madelung field. For $(Sr, Ca)_3(Y, Lu)_2Ge_3O_{12}$, the top of the VB is composed of O 2p orbitals. Therefore, on replacing Sr or Y by smaller Ca or Lu the bond length with O anions decreases and that promotes stronger O 2p shell electron binding energy as observed in Figure 4.10. The VRBE scheme is consistent with the calculated data where it was found that the VB moves downward by 0.13 eV from $Sr_3Y_2Ge_3O_{12}$ to $Ca_3Y_2Ge_3O_{12}$ as compared to the energy of deep Y 4s orbitals (below -40 eV).

The CB bottoms in the $(Sr, Ca)_3(Y, Lu)_2Ge_3O_{12}$ garnets are on average at ~0.45 eV higher energy than in $Y_3Al_5O_{12}$. The VRBE scheme shows that the energy between the Ce^{3+} $5d_1$ level and the CB in $(Sr, Ca)_3(Y, Lu)_2Ge_3O_{12}$ is ~0.5 eV lower than in $Y_3Al_5O_{12}$:Ce^{3+}. It is well established, and particularly so for $Y_3Al_5O_{12}$ by Ueda *et al.*, that the quenching of Ce^{3+} 5d-4f emission is caused by thermal ionization of the 5d electron to the conduction band. Ueda *et al* and Weber *et al* reported that the thermal quenching temperature ($T_{0.5}$) is 643 K and 650 K, respectively[54-55]. The quenching temperature $T_{0.5}$ ~265 K for $Ca_3Y_2Ge_3O_{12}$:Ce^{3+} in Figure 4.6 and corresponding 0.27 eV activation energy (ΔE) is ~0.5 eV lower than in $Y_3Al_5O_{12}$:Ce^{3+} (0.77 eV). This is consistent with the VRBE diagram showing that the Ce^{3+} $5d_1$ in $Ca_3Y_2Ge_3O_{12}$ is 0.55 eV lower than in $Y_3Al_5O_{12}$ value. The low lying conduction band in the germanium based garnets is then the reason for the lower thermal quenching temperature of $(Sr, Ca)_3(Y, Lu)_2Ge_3O_{12}$:$Ce^{3+}$ as compared to the aluminate based garnet $Y_3Al_5O_{12}$:Ce^{3+}.

Table 4.3 The parameters to construct the VRBE diagram of $(Sr,Ca)_3(Y,Lu)_2Ge_3O_{12}$ and $Y_3Al_5O_{12}$. The units for all the parameters are eV.

Compound	E^{ex}	E^{CT}	E_V	E_C	$E_{Ce^{3+}}(5d_1)$	$E_{Ce^{3+}}(5d_2)$	$E_{Ce^{3+}}(5d_3)$	$E_{Ce^{3+}}(5d_4)$	$E_{Ce^{3+}}(5d_5)$
$Sr_3Y_2Ge_3O_{12}$	6.37	4.43	-8.43	-2.06	-2.54	-2.46	-2.33	1.69	1.69
$Sr_3Lu_2Ge_3O_{12}$	6.37	4.68	-8.68	-2.31	-2.54	-2.46	-2.33	1.69	1.69
$Ca_3Y_2Ge_3O_{12}$	6.59	4.77	-8.77	-2.07	-2.62	-2.54	-2.37	1.71	1.73
$Ca_3Lu_2Ge_3O_{12}$	6.59	4.86	-8.86	-2.16	-2.62	-2.54	-2.37	1.71	1.73
$Y_3Al_5O_{12}$	7.10	5.42	-9.38	-1.71	-2.71	-1.77	-0.67	0.08	0.62

For the TL-studies on Ce-Sm, Ce-Eu, Ce-Tm, and Ce-Yb co-doped samples, only the one with (Ce^{3+}, Sm^{3+}) codoping showed a TL signal in the range of 90 to 450 K, (see Figure 4.7). The VRBE diagrams of Figure 4.10 and Figure S4.5 predict that of all the lanthanides only the ground state of divalent Sm, Eu, and Yb will be below the CB. This indicates that the corresponding trivalent ions may act as electron traps and since the ground state of Ce^{3+} is above the valence band it will act as a hole-trapping center. The trap depths from the VRBE diagrams listed in Table 4.3 for Sm^{2+} are 0.67, 0.42, 0.66 and 0.57 eV for (Ce^{3+}, Sm^{3+}) co-doped $Sr_3Y_2Ge_3O_{12}$, $Sr_3Lu_2Ge_3O_{12}$, $Ca_3Y_2Ge_3O_{12}$ and $Ca_3Lu_2Ge_3O_{12}$, respectively. These values are close to the trap depths derived from the thermoluminescence glow curves in Figure 4.7, which are 0.51, 0.44, 0.54 and 0.53 eV, respectively. This confirms that Sm^{3+} codopant acts as the electron-trapping center and since the TL glow is from Ce who acts as the hole-trapping and the recombination center. The same phenomenon is also reported in lanthanides codoped $YPO_4:Ce^{3+}$ [56-57], $GdAlO_3:Ce^{3+}$ [12] and $Y_3Al_5O_{12}:Ce^{3+}$ [58]. In these cases, Ce^{3+} acts as the recombination center as well as the hole-trapping center while the lanthanide codopants act as electron-trapping centers.

The trap depth of Yb^{2+} is always 0.81 eV deeper than that of Sm^{2+}, and for the four garnet compounds has an average value of ~1.43 eV (Figure S4.5). Adopting the frequency factor of 1.3×10^{13} s^{-1} and a heating rate of 1 K s^{-1}, the TL peak maxium temperature calculated with Eq. 4.2, is ~503 K. Figure 4.6 shows that at this TL

temperature the Ce^{3+} emission is totally quenched. For Eu^{3+} codoped samples, the Eu^{2+} trap depths are even 0.3 eV deeper than for Yb^{2+} this is the reason of the absence of TL glow peaks for (Ce^{3+}, Yb^{3+}) and (Ce^{3+}, Eu^{3+}) co-doping combinations.

4.6 Conclusion

Photoluminescence spectroscopy and first-principles calculations were simultaneously performed in this research. Eu^{3+} and Ce^{3+} are found located at both dodecahedral and octahedral sites from the photoluminescence spectroscopy. Calculated data on 4f-5d transition energies for Ce^{3+} on both sites are consistent with the photoluminescence experimental results. The studied germanium based garnets are found to have ~1 eV smaller bandgap than the yttrium aluminate garnet. The VRBE schemes reveal that the conduction bands of the studied germanium based garnets are at ~0.5 eV lower energy and the valence bands at ~0.5 eV higher energy than the yttrium aluminate garnet. A clear trend is observed that the valence band goes downward with decreasing the unit cell volume. The lower lying conduction band causes a lower quenching temperature for the Ce^{3+} emission. Only Sm^{3+} as codopant provides a TL glow, and other codopant lanthanides either cannot trap an electron or trap the electron too deep so that the recombination luminescence on Ce^{3+} will be quenched. The experimental spectroscopic results, the first-principles calculations and the vacuum referred binding energies derived from the chemical shift model all provide a mutually consistent interpretation of the electron, luminescent, and trapping properties of the studied germanium based garnets. The combination of the experiments, first-principles calculations and the semiempirical chemical shift model can be used as an alternative method to screen the luminescence materials for certain applications (for instance, LED phosphors, afterglow, etc.) and to understand the luminescence mechanisms.

4.7 Acknowledgements

4.8 Reference

1. P.Dorenbos, A Review on How Lanthanide Impurity Levels Change with Chemistry and Structure of Inorganic Compounds. *ECS Journal of Solid State Science and Technology* **2013**,2, 3001-3011.

2. Shao, Q.; Lin, H.; Dong, Y.; Fu, Y.; Liang, C.; He, J.; Jiang, J., Thermostability and Photostability of Sr3SiO5:Eu2+ Phosphors for White Led Applications. *Journal of Solid State Chemistry*, *225* (6), 72-77.

3. Joos, J. J.; Dirk, P.; Smet, P. F., Energy Level Modeling of Lanthanide Materials: Review and Uncertainty Analysis. *Physical Chemistry Chemical Physics* **2015**, 17, 19058−19078.

4. Dorenbos, P., Thermal Quenching of Eu2+ 5d–4f Luminescence in Inorganic Compounds. *Journal of Physics: Condensed Matter* **2005**, *17*, 8103-8111.

5. Yeh, C.-W.; Chen, W.-T.; Liu, R.-S.; Hu, S.-F.; Sheu, H.-S.; Chen, J.-M.; Hintzen, H. T., Origin of Thermal Degradation of Sr2-xSi5N8:Eu Phosphors in Air for Light-Emitting Diodes. *Journal of the American Chemical Society* **2012**, *134*, 14108-14117.

6. Ueda, J.; Dorenbos, P.; Bos, A.; Kuroishi, K.; Tanabe, S., Control of Electron Transfer between Ce3+ and Cr3+ in Y3Al5-xGaxO12 Host by Conduction Band Engineering. *Journal of Materials Chemistry C* **2015**, *3*, 5642−5651.

7. Dorenbos, P., Mechanism of Persistent Luminescence in Eu2+ and Dy3+ Codoped Aluminate and Silicate Compounds. *Journal of the Electrochemical Society* **2005**, *152*, H107-H110

8. Li, Y.; Gecevicius, M.; Qiu, J., Long Persistent Phosphors-from Fundamentals to Applications. *Chemical Society Reviews* **2016**, 45, 2090-2136.

9. Dorenbos, P., Modeling the Chemical Shift of Lanthanide 4f Electron Binding Energies. *Physical Review B* **2012**, *85*, 165107−165117.

10. Bos, A. J. J.; Dorenbos, P.; Bessière, A.; Lecointre, A.; Bedu, M.; Bettinelli, M.; Piccinelli, F., Study of Tl Glow Curves of YPO4 Double Doped with Lanthanide Ions. *Radiation Measurements* **2011**, *46*, 1410-1416.

11. Chakrabarti, K.; Mathur, V. K.; Rhodes, J. F.; Abbundi, R. J., Stimulated Luminescence in Rare-Earth-Doped MgS. *Journal of Applied Physics* **1988**, *64*, 1363-1366.

12. Luo, H.; Bos, A. J. J.; Dorenbos, P., Controlled Electron–Hole Trapping and Detrapping Process in GdAlO3 by Valence Band Engineering. *The Journal of Physical Chemistry C* **2016**, *120*, 5916-5925.

13. Zhong, J.; Zhuang, W.; Xing, X.; Liu, R.; Li, Y.; Liu, Y.; Hu, Y., Synthesis, Crystal Structures, and Photoluminescence Properties of Ce3+-Doped Ca2LaZr2Ga3O12: New Garnet Green-Emitting Phosphors for White Leds. *The Journal of Physical Chemistry C* **2015**, *119*, 5562-5569.

14. Chen, L., et al., Charge Deformation and Orbital Hybridization: Intrinsic Mechanisms on Tunable Chromaticity of Y3Al5O12:Ce3+ Luminescence by Doping Gd3+ for Warm White Leds. *Scientific Reports* **2015**, *5*, 11514-11531.

15. Setlur, A. A.; Heward, W. J.; Gao, Y.; Srivastava, A. M.; Chandran, R. G.; Shankar, M. V., Crystal Chemistry and Luminescence of Ce3+-Doped Lu2CaMg2(Si,Ge)3O12 and Its Use in Led Based Lighting. *Chemistry of Materials* **2006**, *18*, 3314-3322.

16. Luo, H.; Liu, J.; Zheng, X.; Xu, B.; Lu, Y.; Han, L.; Ren, K.; Yu, X., Synthesis and Luminescence Properties of Mg–Si Co-Doped Tb3Al5O12:Ce3+ Phosphors with Blue Excitation for White Leds. *Journal of the American Ceramic Society* **2012**, *95*, 3582-3587.

17. NOVAK1AND, G. A.; GIBBS, G. V., The Crystal Chemistry of the Silicate Garnets. *The American Mineralogist* **1971**, *56*, 791-825.

18. Geller, S., Crystal Chemistry of the Garnets. *Zeitschrift für Kristallographie-Crystalline Materials* **1967**, *125*, 1-47.

19. Uhlich, D.; Plewa, J.; Jüstel, T., Phase Formation and Characterization of Sr3Y2Ge3O12, Sr3In2Ge3O12, and Ca3Ga2Ge3O12 Doped by Trivalent Europium. *Journal of Luminescence* **2008**, *128*, 1649-1654.

20. Kalaji, A.; Saines, P. J.; George, N. C.; Cheetham, A. K., Photoluminescence of Cerium-Doped (Ca1-xSrx)3RE2Ge3O12 Garnet Phosphors for Solid State

Lighting: Relating Structure to Emission. *Chemical Physics Letters* **2013**, *586*, 91-96.

21. Kaminskii, A. A.; Mill, B. V.; Butashin, A. V., Growth and Stimulated Emission Spectroscopy of Ca3Ga2Ge3O12:Nd3+ Garnet Crystals. *Physica Status Solidi (a)* **1983**, *78*, 723-732.

22. Kresse, G.; Furthmüller, J., Efficient Iterative Schemes for *Ab* Initio Total-Energy Calculations Using a Plane-Wave Basis Set. *Physical Review B* **1996**, *54*, 11169-11186.

23. Kresse, G.; Joubert, D., From Ultrasoft Pseudopotentials to the Projector Augmented-Wave Method. *Physical Review B* **1999**, *59*, 1758-1775.

24. Freysoldt, C.; Grabowski, B.; Hickel, T.; Neugebauer, J.; Kresse, G.; Janotti, A.; Van de Walle, C. G., First-Principles Calculations for Point Defects in Solids. *Reviews of Modern Physics* **2014**, *86*, 253-305.

25. Blöchl, P. E., Projector Augmented-Wave Method. *Physical Review B* **1994**, *50*, 17953-17979.

26. Barandiarán, Z.; Seijo, L., The Abinitio Model Potential Representation of the Crystalline Environment. Theoretical Study of the Local Distortion on Nacl:Cu+. *The Journal of Chemical Physics* **1988**, *89*, 5739-5746.

27. Gellé, A.; Lepetit, M.-B., Fast Calculation of the Electrostatic Potential in Ionic Crystals by Direct Summation Method. *The Journal of Chemical Physics* **2008**, *128*, 244716-244724.

28. Karlström, G., et al., Molcas: A Program Package for Computational Chemistry. *Computational Materials Science* **2003**, *28*, 222-239.

29. Barandiarán, Z.; Seijo, L., The Abinitio Model Potential Method. Cowan–Griffin Relativistic Core Potentials and Valence Basis Sets from Li (Z = 3) to La (Z = 57). *Canadian Journal of Chemistry* **1992**, *70*, 409-415.

30. Muñoz-García, A. B.; Seijo, L., Structural, Electronic, and Spectroscopic Effects of Ga Codoping on Ce-Doped Yttrium Aluminum Garnet: First-Principles Study. *Physical Review B* **2010**, *82*, 184118.

72

31. Ning, L.; Lin, L.; Li, L.; Wu, C.; Duan, C.-k.; Zhang, Y.; Seijo, L., Electronic Properties and 4f-5d Transitions in Ce-Doped Lu2SiO5: A Theoretical Investigation. *Journal of Materials Chemistry* **2012**, *22*, 13723-13731.

32. Lee, K.-G.; Yu, B.-Y.; Pyun, C.-H.; Mho, S.-I., Vacuum Ultraviolet Excitation and Photoluminescence Characteristics of (Y,Gd)Al3(BO3)4:Eu3+. *Solid State Communications* **2002**, *122*, 485-488.

33. Wintle, A. G., Thermal Quenching of Thermoluminescence in Quartz. *Geophysical Journal International* **1975**, *41*, 107-113.

34. Azorín, J., Determination of Thermoluminescence Parameters from Glow Curves—I. A Review. *International Journal of Radiation Applications and Instrumentation. Part D. Nuclear Tracks and Radiation Measurements* **1986**, *11*, 159-166.

35. Shinde, S. L.; Nanda, K. K., Thermal Oxidation Strategy for the Synthesis of Phase-Controlled GeO2 and Photoluminescence Characterization. *CrystEngComm* **2013**, *15*, 1043-1046.

36. Micoulaut, M.; Cormier, L.; Henderson, G. S., The Structure of Amorphous, Crystalline and Liquid geo 2. *Journal of Physics: Condensed Matter* **2006**, *18*, R753-R784.

37. Marin, S. J.; O'Keeffe, M.; Young Jr, V. G.; Von Dreele, R. B., The Crystal Structure of Sr3Y2Ge3O12. *Journal of Solid State Chemistry* **1991**, *91*, 173-175.

38. Levy, D.; Barbier, J., Normal and Inverse Garnets: Ca3Fe2Ge3O12, Ca3Y2Ge3O12 and Mg3Y2Ge3O12. *Acta Crystallographica Section C* **1999**, *55*, 1611-1614.

39. Ning, L.; Zhou, C.; Chen, W.; Huang, Y.; Duan, C.; Dorenbos, P.; Tao, Y.; Liang, H., Electronic Properties of Ce3+-Doped Sr3Al2O5Cl2: A Combined Spectroscopic and Theoretical Study. *The Journal of Physical Chemistry C* **2015**,119, 6785-6792.

40. Shi, R.; Qi, M.; Ning, L.; Pan, F.; Zhou, L.; Zhou, W.; Huang, Y.; Liang, H., Combined Experimental and Ab Initio Study of Site Preference of Ce3+ in SrAl2O4. *The Journal of Physical Chemistry C* **2015**, *119*, 19326-19332.

41. Ning, L.; Wu, C.; Li, L.; Lin, L.; Duan, C.; Zhang, Y.; Seijo, L., First-Principles Study on Structural Properties and 4f → 5d Transitions of Locally Charge-Compensated Ce3+ in CaF2. *The Journal of Physical Chemistry C* **2012**, *116*, 18419-18426.

42. Liu, X.; Li, L.; Noh, H. M.; Moon, B. K.; Choi, B. C.; Jeong, J. H., Chemical Bond Properties and Charge Transfer Bands of O2-Eu3+, O2-Mo6+ and O2-W6+ in Eu3+-Doped Garnet Hosts Ln3M5O12 and ABO4 Molybdate and Tungstate Phosphors. *Dalton Transactions* **2014**, *43*, 8814-8825.

43. Dorenbos, P., The Charge Transfer Energy and the Relation with the Band Gap of Compounds. *Journal of Luminescence* **2005**, *111*, 89-104.

44. Dorenbos, P., Crystal Field Splitting of Lanthanide 4f-5d Levels. *Journal of Alloys and Compounds* **2002**, *341*,156-159.

45. Huang, B., Native Point Defects in CaS: Focus on Intrinsic Defects and Rare Earth Ion Dopant Levels for up-Converted Persistent Luminescence. *Inorganic Chemistry* **2015**,54,11423-11440.

46. De Vos, A.; Lejaeghere, K.; Vanpoucke, D. E. P.; Joos, J. J.; Smet, P. F.; Hemelsoet, K., First-Principles Study of Antisite Defect Configurations in ZnGa2O4:Cr Persistent Phosphors. *Inorganic Chemistry* **2016**, *55*, 2402-2412.

47. Caldas, M. J.; Fazzio, A.; Zunger, A., A Universal Trend in the Binding Energies of Deep Impurities in Semiconductors. *Applied Physics Letters* **1984**, *45*, 671-673.

48. Wei, S.-H.; Zunger, A., Role of D Orbitals in Valence-Band Offsets of Common-Anion Semiconductors. *Physical Review Letters* **1987**, *59*, 144-147.

49. Xiaobo Chen, S. S., Liejin Guo, and Samuel S. Mao, Semiconductor-Based Photocatalytic Hydrogen Generation. *Chemical Reviews* **2010**,, *110*, 6503–6570.

50. van de Krol, R.; Liang, Y.; Schoonman, J., Solar Hydrogen Production with Nanostructured Metal Oxides. *Journal of Materials Chemistry* **2008**, *18*, 2311-2320.

74

51. Pieter, D., The Electronic Level Structure of Lanthanide Impurities in REPO4 , REBO3 , REAlO3 , and RE2O3 (RE = La, Gd, Y, Lu, Sc) Compounds. *Journal of Physics: Condensed Matter* **2013**, *25*, 225501-225508.

52. Dorenbos, P., The Electronic Structure of Lanthanide Doped Compounds with 3d, 4d, 5d, or 6d Conduction Band States. *Journal of Luminescence* **2014**, *151*, 224-228.

53. Dorenbos, P., Electronic Structure and Optical Properties of the Lanthanide Activated RE3(Al1-xGax)5O12 (Re=Gd, Y, Lu) Garnet Compounds. *Journal of Luminescence* **2013**, *134*, 310-318.

54. Ueda, J.; Dorenbos, P.; Bos, A. J. J.; Meijerink, A.; Tanabe, S., Insight in the Thermal Quenching Mechanism for Y3Al5O12:Ce3+ through Thermoluminescence Excitation Spectroscopy. *The Journal of Physical Chemistry C* **2015**, 119, 25003-25008.

55. Weber, M. J. Nonradiative Decay from 5d States of Rare Earths in Crystals. Solid State Communications. 1973, 12, 741−744.

56. Krumpel, A. H.; Bos, A. J. J.; Bessière, A.; van der Kolk, E.; Dorenbos, P., Ontrolled Electron and Hole Trapping in YPO4:Ce3+,Ln3+ and LuPO4:Ce3+,Ln3+ (Ln=Sm, Dy, Ho, Er, Tm). *Physical Review B* **2009**, *80*, 085103-085113.

57. Dorenbos, P.; Bos, A. J. J.; Poolton, N. R. J., Carrier Recombination Processes and Divalent Lanthanide Spectroscopy in YPO4:Ce3+;L3+ (L=Sm,Dy,Tm). *Physical Review B* **2010**, *82*, 195127-195134.

58. You, F.; Bos, A. J. J.; Shi, Q.; Huang, S.; Dorenbos, P., Thermoluminescence Investigation of Donor Ce3+, Pr3+, Tb3+ Acceptor Eu3+, Yb3+ Pairs in Y3Al5O12. *Physical Review B* **2012**, *85*, 115101-115108.

4.9 Supporting information
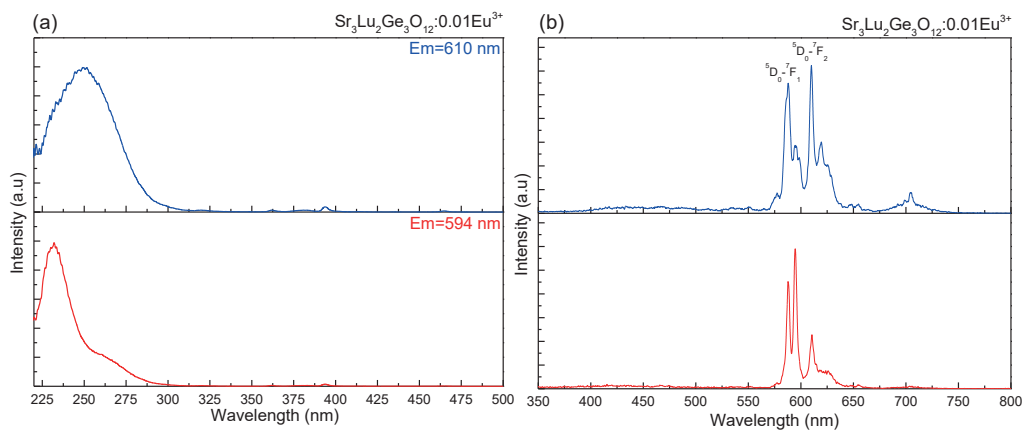
Figure S4.1. Site selective excitation (a) and emission (b) spectra of $Sr_3Lu_2Ge_3O_{12}:0.01Eu^{3+}$. All measurements were performed at RT.
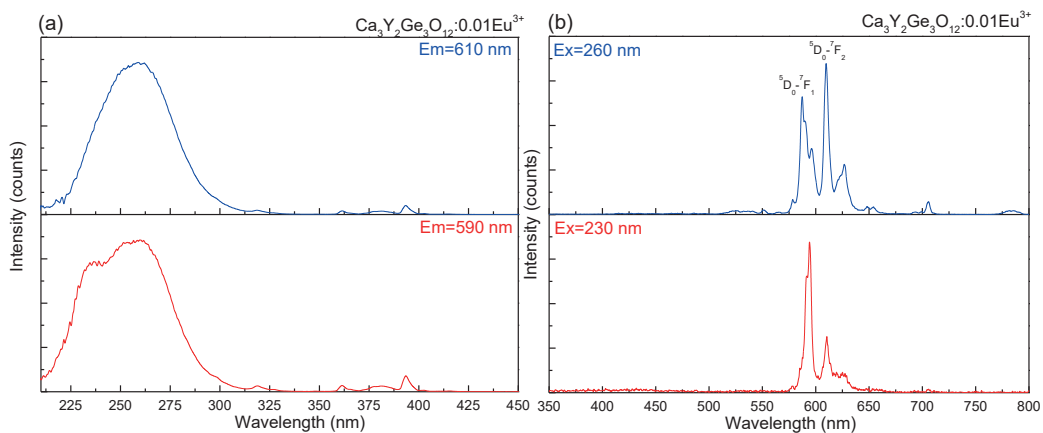
Figure S4.2. Site selective excitation (a) and emission (b) spectra of $Ca_3Y_2Ge_3O_{12}:0.01Eu^{3+}$. All measurements were performed at RT.

76

Figure S4.3. Site selective excitation (a) and emission (b) spectra of $Ca_3Lu_2Ge_3O_{12}$:0.01Eu^{3+}. All measurements were performed at RT.

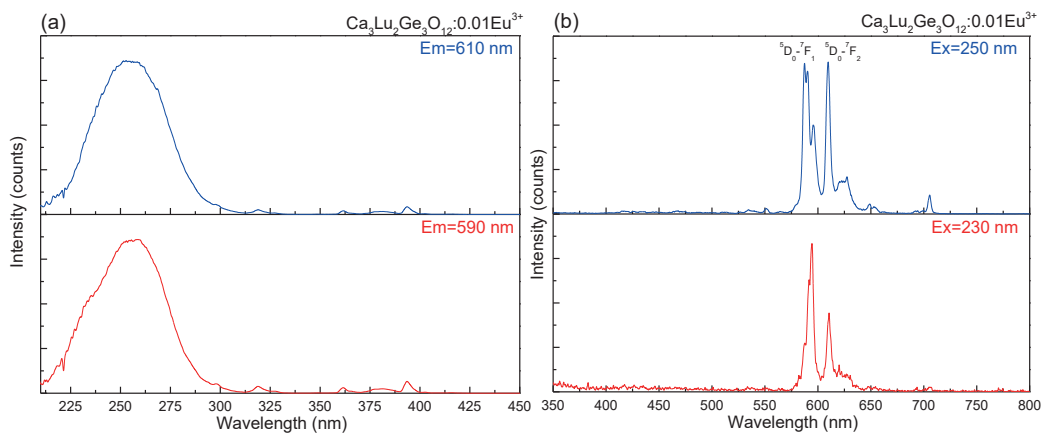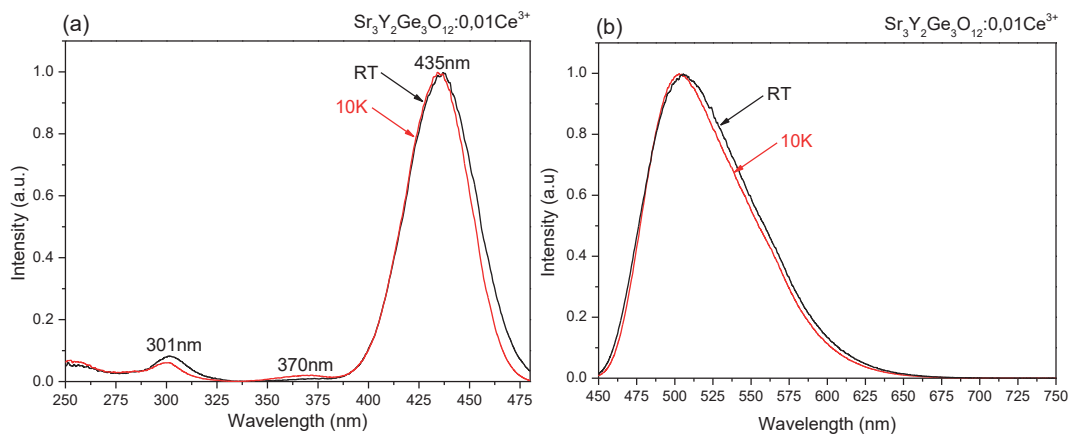Figure S4.4. (a) PLE spectra of $Sr_3Y_2Ge_3O_{12}$:Ce^{3+} monitored at 500 nm emission. (b) PL spectra of $Sr_3Y_2Ge_3O_{12}$:Ce^{3+} excited at 435 nm. The red curves were measured at 10 K and the black curves were measured at room temperature.

Table S4.1. Calculated and experimental values for the lattice parameters and the band gap energy of $Sr_3Y_2Ge_3O_{12}$ and $Ca_3Y_2Ge_3O_{12}$

$Sr_3Y_2Ge_3O_{12}$	a (Å)	O (at C_1 sites)			E_g (eV)
		x	y	z	
PBE0 (25% HF)	13.13747	0.09155	0.19848	0.28893	5.75
PBE0 (32% HF)	13.10606	0.09139	0.19861	0.28909	6.33
Experimental	13.08710	0.09092	0.19828	0.28952	6.38

$Ca_3Y_2Ge_3O_{12}$	a (Å)	O (at C_1 sites)			E_g (eV)
		x	y	z	
PBE0 (25% HF)	12.85153	0.08973	0.19412	0.28562	5.91
PBE0 (32% HF)	12.82131	0.08956	0.19426	0.28580	6.53
Experimental	12.8059	0.08910	0.19330	0.28630	6.70

Table S4.2. The lattice parameters for $Sr_3Y_2Ge_3O_{12}$, $Ca_3Y_2Ge_3O_{12}$ and $Y_3Al_5O_{12}$ host lattices.

Sample	Lattice Constant (Å)	Bond Type	Bond Length (Å)
$Sr_3Y_2Ge_3O_{12}$	13.0871	Sr-O	2.5514 x 4, 2.6833 x 4
		Y-O	2.2494 x 6
		Ge-O	1.7679 x 4
$Ca_3Y_2Ge_3O_{12}$	12.8059	Ca-O	2.4690 x 4, 2.5610 x 4
		Y-O	2.3330 x 6
		Ge-O	1.7660 x 4
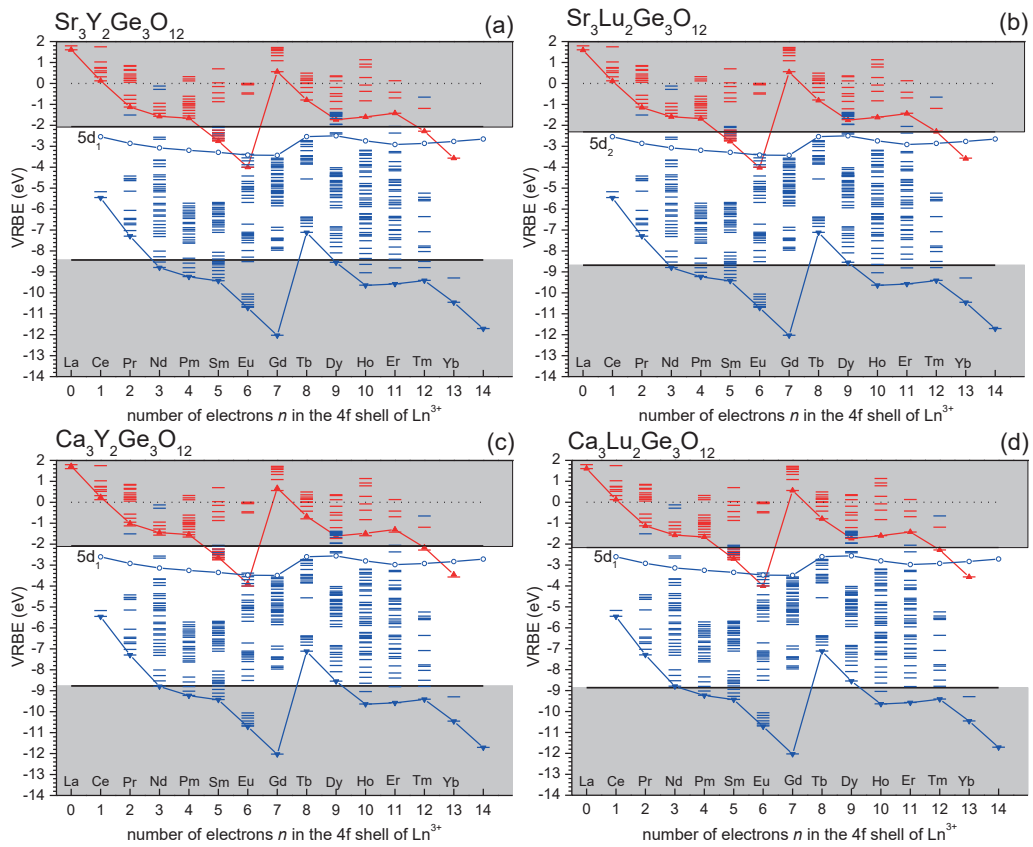
Figure S4.5. The detailed VRBE diagram of (a) $Sr_3Y_2Ge_3O_{12}$, (b) $Sr_3Lu_2Ge_3O_{12}$, (c) $Ca_3Y_2Ge_3O_{12}$ and (d) $Ca_3Lu_2Ge_3O_{12}$

5

Controlled Electron-Hole Trapping and Detrapping Process in GdAlO₃ by Valence Band Engineering

5.1 Abstract

Two different trapping and detrapping processes of charge carriers have been investigated in $GdAlO_3:Ce^{3+},Ln^{3+}$ (Ln= Pr, Er, Nd, Ho, Dy, Tm, Eu and Yb) and $GdAlO_3:Ln^{3+},RE^{3+}$ (Ln=Sm, Eu and Yb, RE= Ce, Pr and Tb). Cerium is the recombination center and lanthanide codopants act as electron trapping centers in $GdAlO_3:Ce^{3+},Ln^{3+}$. Different lanthanide codopants generate different trap depths. The captured electrons released from the lanthanide recombine at cerium *via* the conduction band, eventually producing the broad 5d-4f emission centerd at ~360 nm from Ce^{3+}. On the other hand, Sm^{3+}, Eu^{3+} and Yb^{3+} act as recombination centers, while Ce^{3+}, Pr^{3+} and Tb^{3+} act as hole-trapping centers in $GdAlO_3:Ln^{3+},RE^{3+}$. In this situation, we find evidence that recombination is by means of hole release instead of the more commonly reported electron release. The trapped holes are released from Pr^{4+} or Tb^{4+} and recombine with the trapped electrons on Sm^{2+}, Eu^{2+} or Yb^{2+} and yield characteristic trivalent emission from Sm^{3+}, Eu^{3+} or Yb^{3+} at ~600 nm, ~617 nm or ~980 nm, respectively. Lanthanum was introduced to engineer the valence band energy and change the trap depth in $Gd_{1-x}La_xAlO_3:Eu^{3+},Pr^{3+}$ and $Gd_{1-x}La_xAlO_3:Eu^{3+},Tb^{3+}$. The results show that the valence band moves upwards and the trap depth related to Pr^{3+} or Tb^{3+} decreases.

5.2 Introduction

The trapping and detrapping processes of electrons and holes are of current interest due to the necessity to better understand the mechanism of afterglow and storage phosphors. An afterglow phosphor (or storage phosphor) is composed of the host lattice, the recombination (luminescence) center and the trapping center. The trapping center can be either an electron or a hole trapping center[1]. For afterglow phosphors, the captured electrons/holes are spontaneously released at room temperature from the trapping center and recombine in the luminescence center, eventually causing emission that can range from UV to even near-infrared depending on the luminescence centers and host lattices[2-3]. For storage phosphors, deeper traps are needed to prevent the thermal fading at room temperature[4].

The electron trapping and detrapping process has been widely investigated[5-6]. A good example is the well-known afterglow phosphor $SrAl_2O_4:Eu^{2+},Dy^{3+}$. EXAFS confirmed that the concentration of trivalent europium increases after exposing the

sample to UV light, indicating that Eu^{2+} is the electron donor and electrons are released due to photoionization[7]. The released electrons move freely in the conduction band and will be captured by the electron-trapping center. The nature of the trap is still under debate. The trapped electrons are released slowly and recombine with the europium recombination center and eventually generates Eu^{2+} emission centerd at ~520 nm[8]. The trap depth in this case is the distance between the electron-trapping level and the bottom of the conduction band (CB). The trap depth can be adjusted by the so-called band gap engineering technique. For example, Ga has been used to substitute Al in $Gd_3Al_{5-x}Ga_xO_{12}:Cr^{3+},Eu^{3+}$ [9], $Y_3Al_{5-x}Ga_xO_{12}:Ce^{3+},Cr^{3+}$ [5] and $Zn(Ga_{1-x}Al_x)_2O_4:Cr^{3+},Bi^{3+}$[10]. It was claimed that substitution of Al by Ga lowers the CB that moves more close to the trapped electron level therefore decreasing the trap depth.

Instead of electrons being released from the electron-trapping center to recombine with a luminescence center through the CB, holes can also be released from a hole-trapping center to recombine with a luminescence center *via* the valence band (VB). However, rarely reports are published discussing about hole-trapping and detrapping processes. One of the few examples is $MgS:Ce^{3+},Sm^{3+}$. Chakrabarti *et al* reported that samarium acts as a recombination center and cerium as the trapping center that capture holes after UV irradiation[11]. The holes migrate from cerium to samarium producing Sm^{3+} characteristic emission during the thermoluminescence (TL) readout. Similar phenomenon was also reported in $YPO_4:Sm^{3+},Tb^{3+}$ by Bos *et al*[12]. They observed only a Sm^{3+} characteristic emission in $YPO_4:Sm^{3+}, Tb^{3+}$ at 530 K during the TL readout, which indicates that holes are released from Tb^{4+} to recombine in the samarium luminescence center.

The rare reporting on hole-trapping and detrapping processes is likely caused by a lack in our knowledge on how to identify a hole-trapping center and particularly on the depth of such trap. One needs knowledge on the location of the trapping levels with respect to the valence band maximum (VBM). One also needs to know whether the hole releases at lower temperature than the trapped electron. The knowledge of the energy at the VBM is also needed in other fields, for instance the "natural valence band offset" in semiconductor materials[13-16] or for photocatalytic materials[17]. In those fields the VBM of a compound is always specified with respect to that of another reference compound. It is not until 2012 that a model, called the chemical shift model, was developed to construct a Vacuum Referred

Binding Energy (VRBE) diagram that makes it possible to compare the binding at the VB maximum in different compounds with respect to a same reference energy[18-20]. A finding from this model is that the VRBE in the $4f^n$ ground state for lanthanides (both divalent and trivalent) is almost independent of type of compounds[21-24]. Therefore, the lanthanide-related hole trap depths can be adjusted by changing the VRBE at the top of the VB and electron trap depths by changing the VRBE at the bottom of the CB.

The objective of this study is to reveal electron and hole trapping and detrapping processes. $GdAlO_3$ has been chosen as host lattice because of its simple structure with only one site to substitute for a trivalent lanthanide without the need for charge compensation[25]. We prepared two groups of materials, one group is $GdAlO_3$: Ce^{3+}, Ln^{3+} (Ln= Pr, Er, Nd, Ho, Dy, Tm, Eu and Yb). Here Ce^{3+} will turn out to be the recombination and luminescence center and the lanthanide codopants act as the electron-trapping center with for each lanthanide a different trap depth. The other group is $GdAlO_3$:Ln^{3+},RE^{3+} (Ln=Sm, Eu and Yb, RE= Ce, Pr and Tb). Here Ln^{3+} ions appear to be the recombination and luminescence centers and RE^{3+} ions act as hole-trapping centers. The holes release from the RE^{4+} and recombine with Ln^{2+} producing Ln^{3+} emission *via* the VB. The trap depth of Pr and Tb can be adjusted by VB engineering techniques. Substitution of Gd by La will decrease the band gap but moves the absolute position of the valence band energy upwards, therefore the trap depths related to Pr and Tb hole-trapping centers decrease.

5.3 Experimental

All starting materials were purchased from Sigma-Aldrich and used without further treatment. The appropriate stoichiometric mixture of Al_2O_3 (99.99%) and rare earth oxides with the purity of 5N (99.999%) were weighted according to the chemical formula and milled homogeneously with the help of acetone. After drying ,the powder was synthesized at 1500°C for 10 h in a corundum crucible with the atmosphere of N_2/H_2 (N_2:93%,H_2:7%). After that, the obtained compounds were cooled down to room temperature.

All powders were checked with a PANalytical XPert PRO X-ray diffraction system with Co Kα (λ = 0.178901 nm) X-ray tube (45 kV, 40 mA). The photoluminescence excitation (PLE) and photoluminescence emission (PL)

measurements were measured with a setup that consists of an UV/vis branch with a 500 W Hamamatsu CW Xe lamp and Gemini 180 monochromator and a VUV/UV branch using a deuterium lamp with an ARC VM502 vacuum monochromator. The PerkinElmer MP-1913 photomultiplier was exploited as a detector connected at the exit slit of a Princeton Acton SP2300 monochromator. The sample is placed in an evacuated sample chamber.

TL measurements above room temperature (300-600 K) were performed with a RISØ TL/OSL reader (model DA-15) and a controller (model DA-20). Samples were irradiated with a $^{90}Sr/^{90}Y$ beta source with a dose rate of 0.7 mGy s^{-1}. Low temperature TL measurements (90-450 K) were recorded with a sample chamber operating under vacuum (P = 10^{-7} mbar), a $^{90}Sr/^{90}Y$ beta irradiation source having a dose rate of ∼0.4 mGy s^{-1} and a PerkinElmer channel PM tube (MP-1393). Liquid nitrogen was used as a cooling medium. A 3 mm C5-58 filter from about 350 to 470 nm was placed between the sample and photomultiplier tube (PMT) during the measurements of $GdAlO_3$:Ce^{3+},Ln^{3+} (Ln= Pr, Er, Nd, Ho, Dy, Tm, Eu and Yb). For the measurements of $GdAlO_3$:Ln^{3+},RE^{3+} (Ln=Sm, Eu and Yb, RE= Ce, Pr and Tb), a 600 nm bandpass filter (600FS40-50) was placed between the sample and PMT[26].

TL emission spectra (TLEM) were measured using an UV to vis spectrometer (Ocean Optics, QE65000) and a NIR spectrometer (Ocean Optics, NIRQ512) with a HR composite grating (300 lines/mm) and an entrance aperture of 100 mm resulting in a 3.3 nm (FWHM) wavelength resolution. The spectral range is 200 to 900 nm for QE65000 and 900 to 1700 nm for NIRQ512.

The TL excitation spectra (TLE) were measured by first illuminating the samples during 600 s with a monochromatic photon beam produced with a 150 W Xenon arc lamp (Hamamatsu L2273) filtered by a 1/8 monochromator (Oriel Cornerstone 130) with wavelength resolution of 0.8 nm/0.1 mm slit width. Next, the system is programmed to record all the TL glow curves from room temperature to 350 °C with changing illumination wavelength. The plot of the integrated TL glow peaks versus the illumination wavelength is called a TL excitation spectra. A 600 nm bandpass filter (600FS40-50) was placed between the sample and PMT.

5.4 Results

5.4.1 X-Ray diffraction spectra, photoluminescence spectroscopy and vacuum referred binding energy diagram of GdAlO$_3$

Figure 5.1 shows XRD patterns of GdAlO$_3$ with different content of lanthanum. The peaks of the synthesized phosphors exhibit a slight shift toward smaller 2θ angles with respect to the pattern of pure GdAlO$_3$. This confirms that the lanthanum ions enter into the gadolinium site and increase the cell volume because lanthanum has a larger ionic radius than gadolinium. A solid solution can be achieved provided that the La content remains less than 0.5. Two separate phases of GdAlO$_3$ and LaAlO$_3$ appear when the content of La is 0.75 (Figure S5.1 in the Supporting Information).
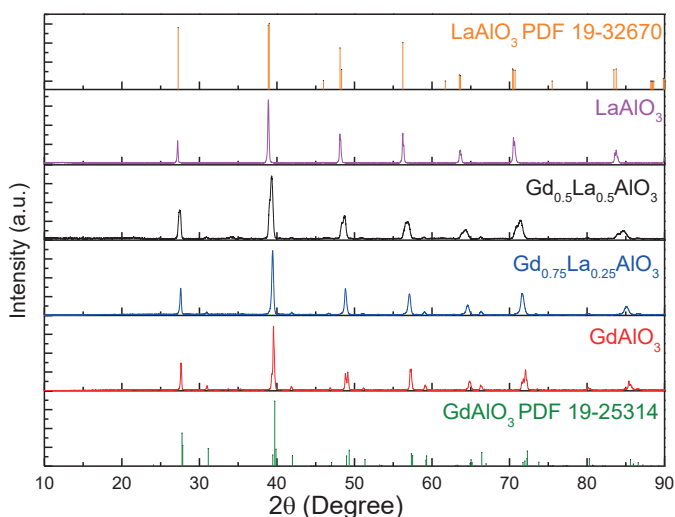
Figure 5.1. XRD patterns of the as-prepared samples of GdAlO$_3$, Gd$_{0.75}$La$_{0.25}$AlO$_3$, Gd$_{0.5}$La$_{0.5}$AlO$_3$ and LaAlO$_3$.

Figure 5.2 shows low-temperature excitation and emission spectra of Eu^{3+} for different values of the La fraction x. The host exciton creation band can be observed in the VUV and decreased from 7.29 eV (170 nm) for GdAlO$_3$ to 6.38 eV (195 nm) for LaAlO$_3$, which implies that the band gap decreases with increasing lanthanum content. The exciton energy found for GdAlO$_3$ and LaAlO$_3$ is close to values in previous reports, i.e., 7.08 eV (175 nm) for GdAlO$_3$[27] and 5.5 (225 nm)-6.5 eV (190 nm) for LaAlO$_3$[28-31]. The broad excitation band in the UV between 200

86

nm and 290 nm for $GdAlO_3$ is due to electron transfer from the valence band to Eu^{3+}. It shifts towards longer wavelength with increase of x. The energy of the charge transfer band for Eu^{3+} decreases from 4.86 eV (255 nm) for $GdAlO_3$ to 3.93 eV (315 nm) for $LaAlO_3$. The values are similar with those in previous reports: e.g., 4.68 eV (265 nm) for $GdAlO_3$ and 3.95 eV (315 nm) for $LaAlO_3$[32]. Figure 5.2b shows the emission spectra of Eu^{3+} in $Gd_{1-x}La_xAlO_3$ with different content of La excited at the peak of the charge transfer band. All the samples show Eu^{3+} characteristic red emission.
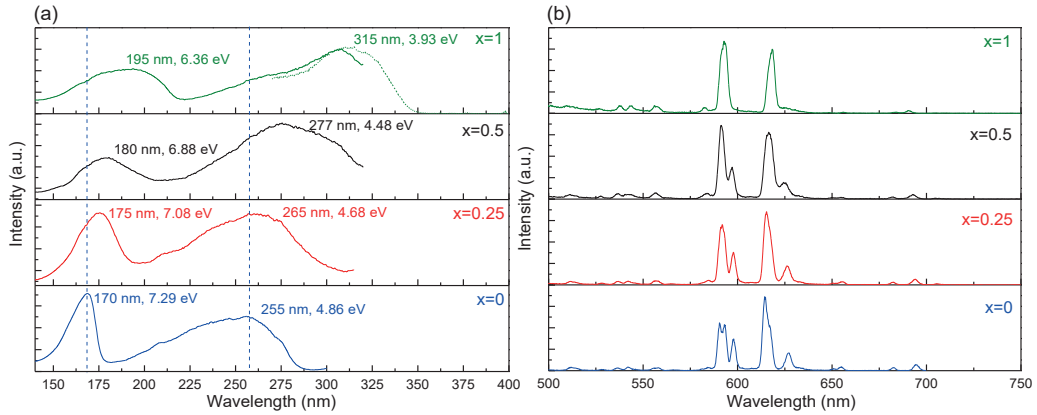

Figure 5.2. PLE (a) and PL spectra (b) of $Gd_{1-x}La_xAlO_3:0.01Eu^{3+},0.01Tb^{3+}$ (x=0, 0.25, 0.5 and 1). The excitation spectrum from 150 to 320 was measured by deuterium lamp excitation (solid line). The excitation spectrum from 250 nm to 400 nm was measured by Xe lamp excitation (dotted line). The excitation spectra were recorded at 592 nm emission and the emission spectra were excited at the charge transfer peak maxima. All measurements were performed at 10 K.

Figure 5.3 displays the vacuum-referred binding energy (VRBE) scheme for $GdAlO_3$. The zigzag curves labelled curve 1 and curve 2 connect the VRBE of an electron in the lowest $4f^n$ levels of the trivalent and the divalent lanthanides, respectively. All those VRBEs are fully determined from knowledge on the Coulomb repulsion energy of U(6,A)=6.75 eV as provided in Ref [22]. The Eu^{3+} charge transfer energy of 4.86 eV as obtained from Figure 5.2a and indicated by arrow 2 in Figure 5.3 provides then the VRBE E_V= -8.80 eV at the top of valence band. The mobility band gap E_{VC}, or the energy between the bottom of the CB and the top of the VB, is obtained from the host exciton creation energy of 7.29 eV (Figure 5.2) and an estimated value for the exciton binding energy. For wide band

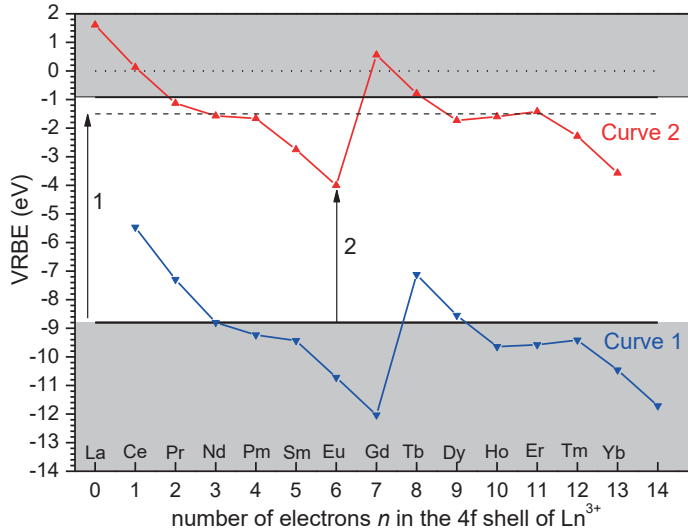gap compounds it is estimated around 8% of the exciton creation energy, resulting in $E_{VC} = 7.87$ eV.

Figure 5.3. Low temperature vacuum referred binding energy diagram for $GdAlO_3$. Arrow 1 shows the transition of host exciton creation. Arrow 2 indicates the charge transfer from O^{2-} to Eu^{3+}.

The VRBE diagram predicts that electrons trapped by Pr^{3+}, Nd^{3+}, Sm^{3+}, Dy^{3+}, Ho^{3+}, Er^{3+}, Tm^{3+} or Yb^{3+} will be released at lower temperature than the holes trapped by Ce^{3+} and recombine with Ce producing Ce^{3+} 5d-4f emission. For combinations of Tb^{3+}/ Pr^{3+} with Sm^{3+}, Eu^{3+} or Yb^{3+} the scheme predicts that the holes release earlier from Tb^{4+} and Pr^{4+} than electrons from the deep traps by Sm, Eu, Yb to produce characteristic Sm^{3+}, Eu^{3+}, Yb^{3+} emission.

5.4.2 Thermoluminescence glow curves of GdAlO$_3$: Ce^{3+},Ln^{3+} (Ln= Pr, Er, Nd, Ho, Dy, Tm, Eu and Yb)

In Figure 5.4 the normalized TL glow curves from Ce^{3+} 5d-4f emission in $GdAlO_3:Ce^{3+}$, Ln^{3+} (Ln= Er, Nd, Ho, Dy and Tm) are shown. The TL maximum temperatures are spread out from 150 K for $GdAlO_3:Ce^{3+},Er^{3+}$ to 413 K for $GdAlO_3:Ce^{3+},Tm^{3+}$. No TL glow peaks with Ce^{3+} emission were observed for the samples codoped with Pr^{3+}, Sm^{3+}, Eu^{3+} or Yb^{3+}.

The trapping parameters of the Tm^{3+} trapping center in $GdAlO_3:Ce^{3+},Tm^{3+}$ were determined using the variable heating rate method[5, 33-34] (Figure S5.2). For the trap depth a value of 1.26 eV and for the frequency factor a value of $3x10^{14}$ s^{-1} was found. Since all codopants Er^{3+}, Nd^{3+}, Ho^{3+}, Dy^{3+} and Tm^{3+} replace Gd^{3+} in the host it is plausible to assume that the frequency factor remains the same[35]. Then, the trap depths for the codopants Er^{3+}, Nd^{3+}, Ho^{3+}, Dy^{3+} were found using the T_m from Figure 5.4 and employing

$$\frac{\beta E}{kT_m^2} = s \exp(-\frac{E}{kT_m}) \qquad\qquad 5.1$$

where $\beta = 1$ K s^{-1} is the heating rate, k is the Boltzman constant (eV K^{-1}), $s = 3x10^{14}$ s^{-1}, and T_m is the temperature (K) at the glow curve peak maximum. The values of the trap depths are shown in the legend of the figure.
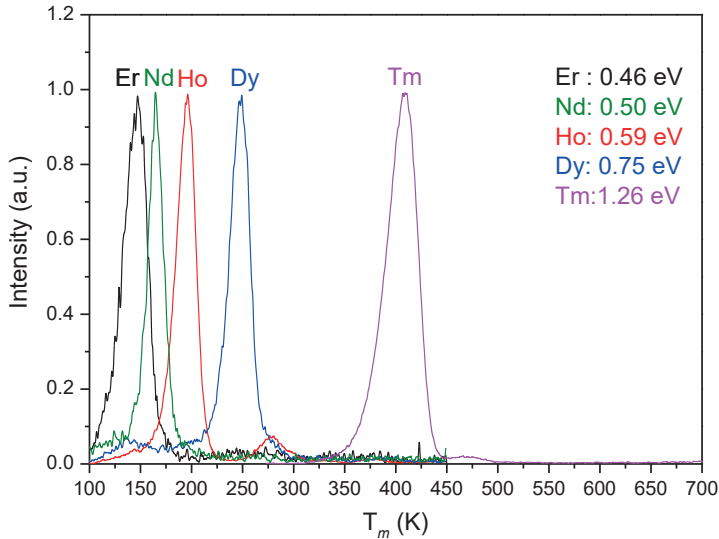
Figure 5.4. Normalized thermoluminescence glow curves of $GdAlO_3:0.01Ce^{3+},0.01Ln^{3+}$ (Ln= Er, Nd, Ho, Dy and Tm). The glow curves of Er, Nd, Ho and Dy codoped samples were measured by the low-temperature TL setup from 90 to 450 K after 1600 s irradiation by its β source. $GdAlO_3:Ce^{3+},Tm^{3+}$ was recorded by the RISØ TL-reader from 300 to 700 K after 1600 s irradiation by its β source. The heating rate was 1 K/s for all TL-recordings. The TL glow curves were measured with a Hoya 3 mm C5-58 bandpass filter from about 350 to 470 nm to transmit the 5d-4f Ce^{3+} emission (at 343 nm and 362 nm).

5.4.3 Thermoluminescence properties of GdAlO$_3$:Ln^{3+}, RE^{3+} (Ln=Sm, Eu and Yb, RE= Ce, Pr and Tb) and Gd$_{1-x}$La$_x$AlO$_3$:Ln^{3+}, Eu^{3+} (Ln= Sm and Eu).

Thermoluminescence emission (TLEM) spectra were measured for GdAlO$_3$:Ln^{3+}, RE^{3+} (Ln=Sm, Eu and Yb, RE= Ce, Pr and Tb) samples in order to identify the luminescence and recombination center during TL readout. Parts a, b, and c of Figure 5.5 show typical TLEM spectra of GdAlO$_3$:Eu^{3+},Tb^{3+}, GdAlO$_3$:Sm^{3+},Tb^{3+} and GdAlO$_3$:Yb^{3+},Tb^{3+}, respectively. Similar figures for other dopant combinations can be found in Figure S5.3.
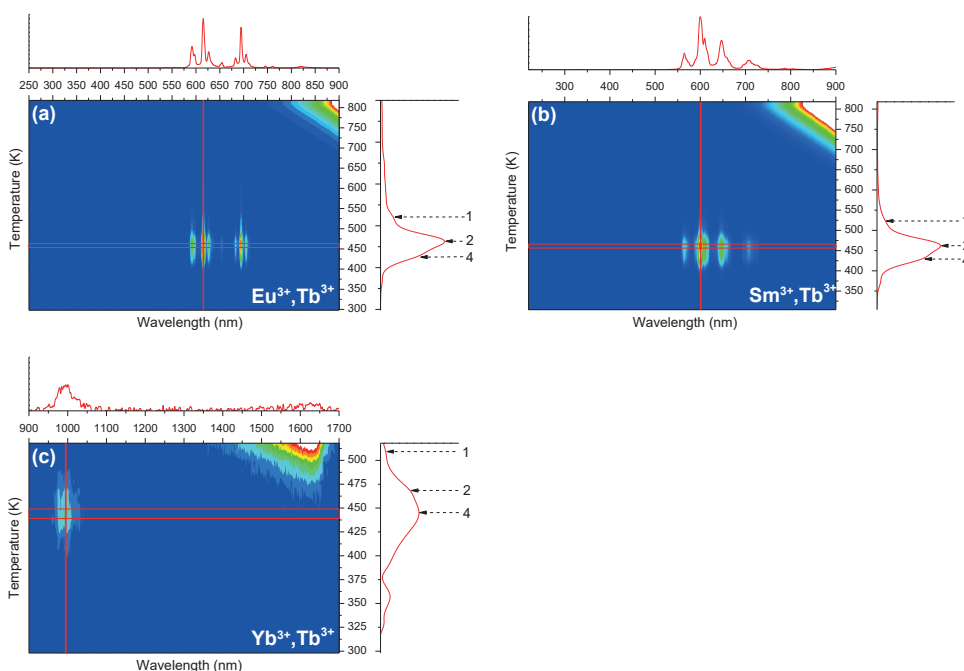
Figure 5.5. Thermoluminescence emission spectra of (a) GdAlO$_3$:0.01Eu^{3+},0.01Tb^{3+}, (b) GdAlO$_3$:0.01Sm^{3+},0.01Tb^{3+} and (c) GdAlO$_3$:0.01Yb^{3+},0.01Tb^{3+}. The samples (a) and (b) were measured by the UV/vis spectrometer (Ocean Optics, QE65000) from 300 to 800 K, sample (c) was measured by the NIR spectrometer (Ocean Optics, NIRQ512) from 300 to 520 K. The heating rate for all of these samples is 5 K/s after exposure to irradiation of 2.5 kGy from a ^{60}Co source.

Characteristic red Eu^{3+} emission with the associated TL glow curve centerd at ~460 K (heating rate 5 K s^{-1}) can be observed for GdAlO$_3$:Eu^{3+} (Figure S5.3a),

GdAlO$_3$:Eu^{3+},Tb^{3+} (Figure 5.5a), GdAlO$_3$:Eu^{3+},Pr^{3+} (Figure S5.3b) and for GdAlO$_3$:Eu^{3+},Ce^{3+} (Figure S5.3c) samples. This glow peak will be referred to as peak 2 and will later be attributed to hole release from a host-related defect. No emission from Tb^{3+}, Pr^{3+} or Ce^{3+} is observed indicating that only the Eu^{3+} ions act as the recombination (luminescence) center in these samples. An additional shoulder (peak 4) in the TL glow is observed at ~435 K in the GdAlO$_3$:Eu^{3+},Tb^{3+} sample (Figure 5.5a). For the GdAlO$_3$:Eu^{3+},Pr^{3+} sample, the shoulder (peak 3) is at 15 K higher temperature ~450 K (Figure S5.3b).

Similarly, a characteristic emission from Sm^{3+} with again the TL glow peak 2 centerd at ~460 K is observed in GdAlO$_3$:Sm^{3+} (Figure S5.3d), GdAlO$_3$:Sm^{3+},Tb^{3+} (Figure 5.5b), GdAlO$_3$:Sm^{3+},Pr^{3+} (Figure S5.3e) and GdAlO$_3$:Sm^{3+},Ce^{3+} (Figure S5.3f) samples. Again no emission from Tb^{3+}, Pr^{3+} or Ce^{3+} is monitored. For GdAlO$_3$:Sm^{3+},Tb^{3+} the shoulder peak 4 at ~435 K appears in Figure 5.5b. A similar shoulder peak 3 at ~445 K is observed for GdAlO$_3$:Sm^{3+},Pr^{3+} in Figure S5.3e.

The Yb^{3+} characteristic emission from the $^2F_{7/2}$ level to the $^2F_{5/2}$ ground state is centerd at ~980 nm and is observed both in GdAlO$_3$:Yb^{3+} (Figure S5.3g) and GdAlO$_3$:Yb^{3+},Tb^{3+} (Figure 5.5c). The glow peak 2 for both samples are found at ~460 K (heating rate 5 K/s). The GdAlO$_3$:Yb^{3+},Tb^{3+} sample (Figure 5.5c) shows a glow peak 4 at ~445 K, which is the same as those in Figure 5.5a and Figure 5.5b. Yb^{3+} emission is absent in the GdAlO$_3$:Yb^{3+}, Pr^{3+} and GdAlO$_3$:Yb^{3+}, Ce^{3+} samples.
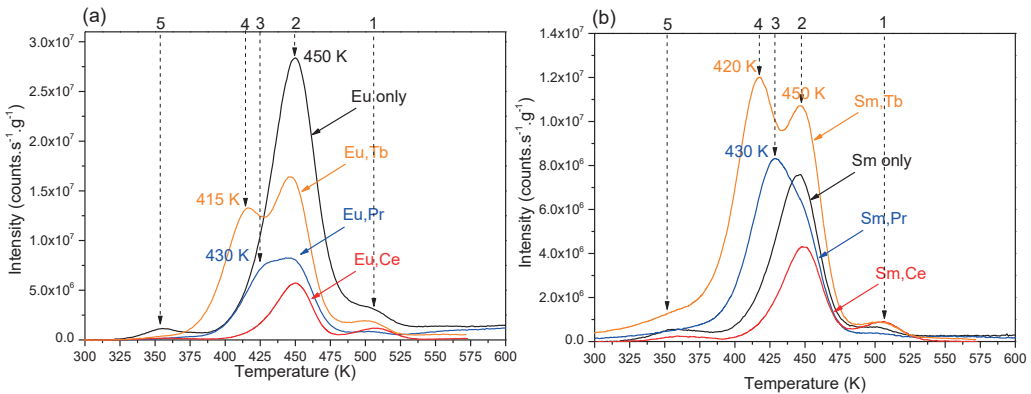
Figure 5.6. Thermoluminescence glow curves of (a) GdAlO$_3$:0.01Eu^{3+},0.01 RE^{3+}, (b) GdAlO$_3$:0.01Sm^{3+}, 0.01RE^{3+} (RE= Ce, Pr and Tb). Figure 5.6(a) and (b) were measured with the RISØ TL-reader from 300 to 600 K with 1600 s irradiation by its β source. The

heating rate was 1 K/s for all TL-recordings. A 600 nm bandpass filter (600FS40-50) was placed between the samples and PMT. The peak intensities are calibrated by mass.

Parts (a) and (b) of Figure 5.6 show TL glow curves of $GdAlO_3:Eu^{3+}$, RE^{3+} and $GdAlO_3:Sm^{3+}$, RE^{3+} (RE= Ce, Pr and Tb). All samples share the same glow peaks 5 and 2 at ~350 K and ~450 K and an additional one at ~510 K (heating rate 1 K/s) hereafter referred to as peak 1. Glow peaks 4 and 3 appear at ~415 K and ~430 K for $GdAlO_3:Eu^{3+},Tb^{3+}$ and $GdAlO_3:Eu^{3+},Pr^{3+}$ in Figure 5.6a, respectively. These two peaks can also be observed at ~420 K or ~430 K for the samples codoped with Tb^{3+} or Pr^{3+} in Figure 5.6b. Peaks 2-4 appear also in the TLEM spectra (Figure 5.5) at somewhat different temperature because of the different heating rate. We conclude that peak 1 and 2 are from host related hole traps, peak 3 from Pr^{4+} and peak 4 from the Tb^{4+} hole-trapping center. No additional TL peaks are observed for Ce^{3+} codoped samples. The trap depths were calculated with Eq. 5.1 using a frequency factor of $3x10^{14}$ s^{-1}. Peak temperatures T_m and calculated trap depths are listed in Table 5.1. Since the TL intensity of Eu^{3+} doped samples are about twice higher than that of Sm^{3+} doped ones, the studies presented below were focused on the Eu^{3+} doped samples.

Table 5.1. List of samples, TL glow peaks and estimated trap depths

sample	glow peak	trap depth E (eV)
$GdAlO_3:Eu^{3+}$	2	1.39 ± 0.02
$GdAlO_3:Eu^{3+}$, Tb^{3+}	4 and 2	1.28 ± 0.02 and 1.39 ± 0.02
$GdAlO_3:Eu^{3+}$, Pr^{3+}	3 and 2	1.33 ± 0.03 and 1.39 ± 0.02
$GdAlO_3:Eu^{3+}$, Ce^{3+}	2	1.39 ± 0.02
$GdAlO_3:Sm^{3+}$	2	1.39 ± 0.02
$GdAlO_3:Sm^{3+}$, Tb^{3+}	4 and 2	1.29 ± 0.02 and 1.39 ± 0.02
$GdAlO_3:Sm^{3+}$, Pr^{3+}	3 and 2	1.33 ± 0.03 and 1.39 ± 0.02
$GdAlO_3:Sm^{3+}$, Ce^{3+}	2	1.39 ± 0.02

Figure 5.7a shows the normalized TL glow curves for $Gd_{1-x}La_xAlO_3:Eu^{3+},Tb^{3+}$ with different content of lanthanum. The as measured TL glow curves are shown in Figure S5.4a. One observes that the glow peak maxima shift toward lower temperature with increasing content of lanthanum. When the lanthanum content is 0.25 (x=0.25), peak 2 has weakened and shifted to 440 K. Peak 4 at 415 K for x=0

becomes much broader and shifts towards 390 K and 365 K for x=0.25 and 0.5, respectively. Peak 4 seems missing in the LaAlO$_3$ sample.

Our main conclusion is that peak 4 broadens and shifts towards lower temperature with increase of La concentration. The frequency factor for LaAlO$_3$ can be deduced as 6.5×10^{13} s^{-1} by the variable heating rate plot of LaAlO$_3$:Eu^{3+},Tb^{3+} (Figure S5.5). However, the frequency factor for x=0.25 and 0.5 samples cannot be determined with this method because the TL glow peaks are much broadened. Considering that the compounds are quite similar, the frequency factor of Gd$_{1-x}$La$_x$AlO$_3$ for x=0.25 and 0.5 samples are fixed as 3×10^{14} s^{-1}, sharing the same value of GdAlO$_3$. The average traps depths are then estimated by Eq. 5.1 and the results are listed in Table 5.2.
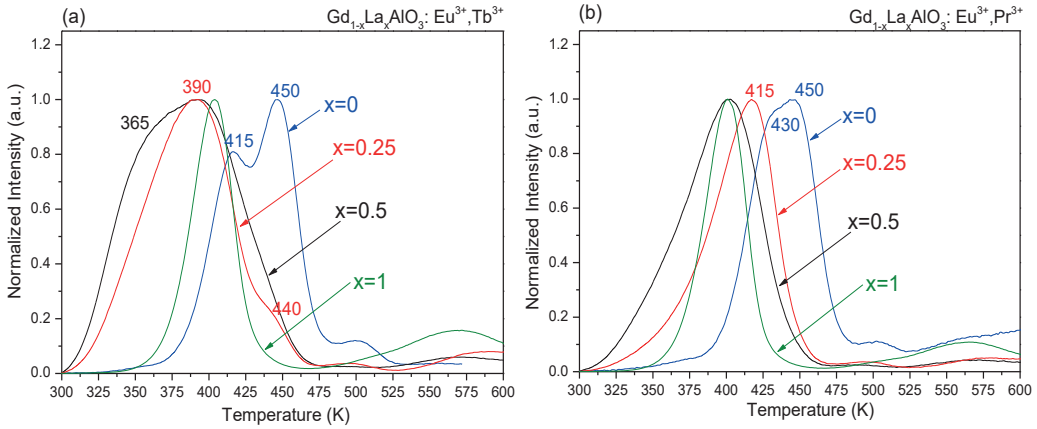

Figure 5.7. Normalized thermoluminescence glow curves of (a) Gd$_{1-x}$La$_x$AlO$_3$:0.01Eu^{3+},0.01Tb^{3+}, (b) Gd$_{1-x}$La$_x$AlO$_3$:0.01Eu^{3+},0.01Pr^{3+}. All glow curves were measured by the RISØ TL-reader from 300 to 600 K with 1600 s irradiation by its β source. The heating rate was 1 K/s for all TL-recordings. A 600 nm bandpass filter (600FS40-50) was placed between the samples and PMT in order to select the Eu^{3+} emission.

Table 5.2. Glow peak positions and trap depths of Gd$_{1-x}$La$_x$AlO$_3$:0.01Eu^{3+},0.01Tb^{3+}.

x	peak position T_m (K)	trap depth E (eV)	frequency factor s (s^{-1})
0	415 ± 5 and 450 ± 5	1.28 ± 0.02 and 1.39 ± 0.02	3.0×10^{14}
0.25	390 ± 5 and 440 ± 5	1.20 ± 0.02 and 1.36 ± 0.02	(3.0×10^{14})
0.5	365 ± 15 and 395 ± 5	1.12 ± 0.05 and 1.22 ± 0.02	(3.0×10^{14})
1	400 ± 5	1.18 ± 0.02	6.5×10^{13}

Figure 5.7b shows the normalized TL glow curves of $Gd_{1-x}La_xAlO_3:Eu^{3+},Pr^{3+}$ with different content of lanthanum. The as measured TL glow curves are shown in Figure S5.4b. Similar to Figure 5.7a, the TL glow peaks below appear to shift to lower temperature when increasing the concentration of lanthanum. The clear double peak observed for x=0 is not observed for the La diluted samples. Trap depths are listed in Table 5.3.

Table 5.3. Peak positions and trap depths of $Gd_{1-x}La_xAlO_3:0.01Eu^{3+},0.01Pr^{3+}.$

x	peak positions T_m (K)	trap depths E (eV)	frequency factor s (s^{-1})
0	430 ± 10 and 450 ± 5	1.33 ± 0.03 and 1.39 ± 0.02	3.0×10^{14}
0.25	415 ± 5	1.28 ± 0.02	(3.0×10^{14})
0.5	400 ± 5	1.23 ± 0.02	(3.0×10^{14})
1	400 ± 5	1.18 ± 0.02	6.5×10^{13}

Figure 5.8b shows the thermoluminescence excitation (TLE) spectrum of $LaAlO_3:Tb^{3+},Eu^{3+}$. A broad band centerd at ~315 nm is observed. For comparison the Eu^{3+} luminescence excitation spectrum from Figure 5.2a is shown as well (Figure 5.8a). The broad TLE band peaking at 315 nm corresponds with the broad CT-band also observed in the luminescence excitation spectrum.
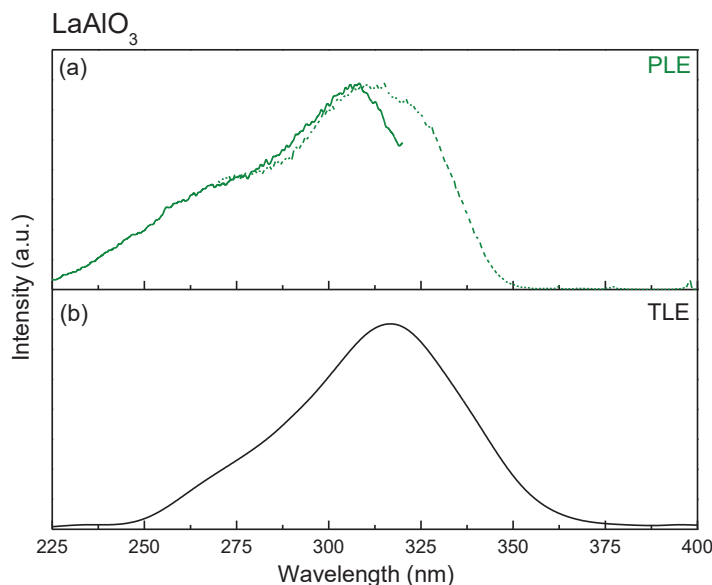
Figure 5.8. Comparison of (a) photoluminescence excitation spectra of $LaAlO_3:0.01Eu^{3+}$ recorded at 592 nm emission and (b) thermoluminescence excitation spectrum of $LaAlO_3:0.01Eu^{3+},0.01Tb^{3+}$. The sample has been excited by a Xe lamp from 200 to 450 nm for 600 s before measuring. The thermoluminescence excitation spectra were obtained by plotting the integrated TL from 300 to 600 K as function of the excitation wavelength. The heating rate for TL readout is 1K/s and the wavelength step is 5 nm. The sample was illuminated at room temperature.

The isothermal decay spectra of $Gd_{1-x}La_xAlO_3:0.01Eu^{3+},0.01Tb^{3+}$ and $Gd_{1-x}La_xAlO_3:0.01Eu^{3+},0.01Pr^{3+}$ can be found in Figure 5.9. The measurements were only carried out with the lanthanum content x=0.25 and 0.5 because these samples contain the significant tails at ~360 K that benefit to afterglow properties. One can observe that $Gd_{0.5}La_{0.5}AlO_3:0.01Eu^{3+},0.01Tb^{3+}$ has the best afterglow properties among all of the samples indicating a proper trap depth.

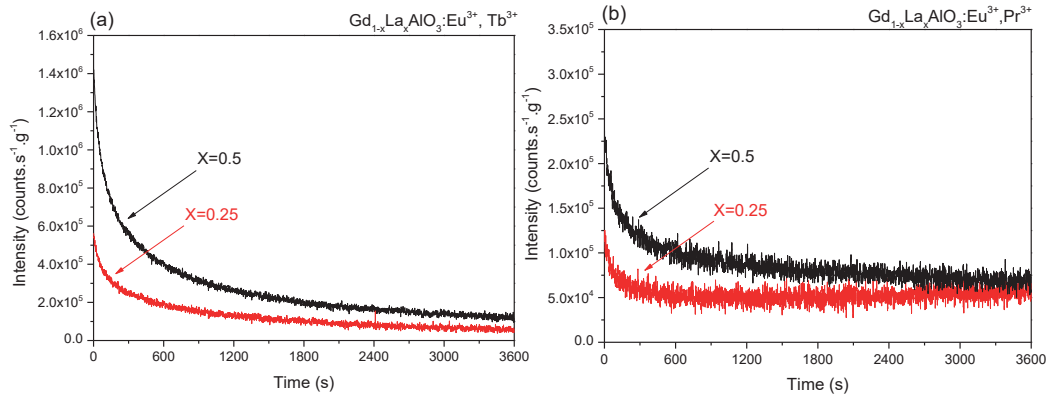Figure 5.9. Room temperature isothermal decay spectra of (a) $Gd_{1-x}La_xAlO_3:0.01Eu^{3+},0.01Tb^{3+}$, (b) $Gd_{1-x}La_xAlO_3:0.01Eu^{3+},0.01Pr^{3+}$ with x=0.25 and 0.5. All the samples were irradiated by β source for 1600 s and the intensity was corrected by mass.

5.5 Discussion

To discuss the trapping and detrapping process of charge carriers in $GdAlO_3$, we will exploit the VRBE diagram in Figure 5.3. The charge carriers generated by β irradiation can move freely through the conduction band and the valence band. Electrons are then trapped by electron-trapping centers (like Nd, Sm, Dy, Ho, Er, Tm, Yb) and holes by hole-trapping centers (like Ce, Pr, Tb). Such prediction of hole release, hole trapping and hole transport from a VRBE scheme (in contrast to the case of electrons) has never been really tested experimentally. Below we will

provide evidence that the predictions fully agree with the observations. Note that holes tend to be shared between two oxygen anions to form a so-called V_k center[36-38]. Often movement of such a center is thermally activated and in a VRBE diagram one should place the V_k hole state higher than above the top of the valence band with an amount equal to the binding energy of the V_k-center[39].

5.5.1 Electron trapping and electron release

Figure 5.4 shows that the TL glow peak temperatures T_m are different for different lanthanides in Ce^{3+} and Ln^{3+} (Ln= Er, Nd, Ho, Dy and Tm) codoped $GdAlO_3$. The change in T_m implies that the type of lanthanide codopants influence the trap depth significantly.
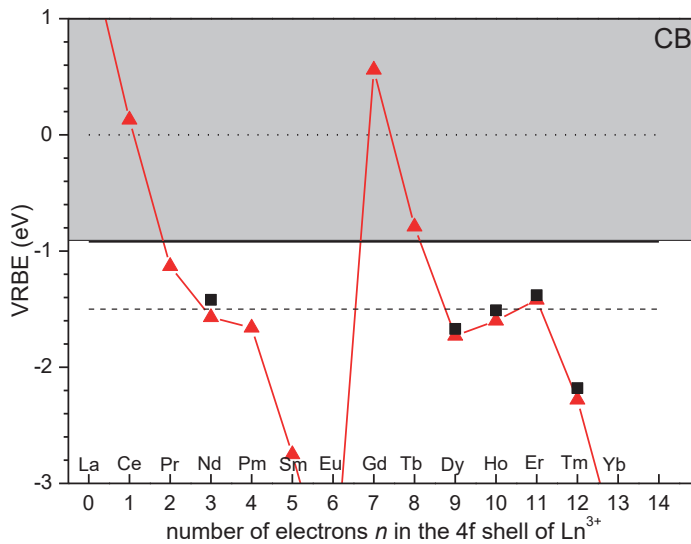
Figure 5.10. Comparison of the VRBE predicted by the VRBE diagram (▲) and TL experiments (■).

In Figure 5.10 the trap depths listed in the legend of Figure 5.4 are compared with the VRBE levels in Figure 5.3. They fully agree with the prediction made from the VRBE diagram however with a systematic shift. The diagram predicts that Tm has the deepest trap depth among the above five codopants (Er, Nd, Ho, Dy and Tm), resulting in its TL glow peak at the highest temperature. On the other hand, Er has the shallowest trap depth, which produces a TL glow peak at the lowest

temperature. No TL glow peaks with Ce^{3+} emission can be found for (Ce,Pr), (Ce,Sm), (Ce,Eu) and (Ce,Yb) codoped samples. The electron trap depth of Pr is predicted as very shallow and its glow peak temperature then will fall beyond the temperature range of our TL facility. The trap depth of Sm^{2+} in the VRBE diagram is 1.83 eV which would correspond with T_m = 587 K if s = 3.0×10^{14} s^{-1} and β = 1 K/s. Ce^{3+} emission GdAlO₃ is totally quenched at this temperature[28]. The trap depths of Eu^{2+} and Yb^{2+} are even deeper than that of Sm^{2+} and absence of Ce^{3+} TL emission for these codopants is also attributed to thermal quenching of Ce^{3+} emission.

Although the trap depths predicted by the VRBE diagram follow the values derived from the TL experiments there is one deviating data point. The VRBE diagram shows a trap depth of Nd^{2+} 0.03 eV deeper than that of Ho^{2+}. So one expects that the TL glow peak maximum temperature of Nd^{2+} is at a higher temperature than the one of Ho^{2+}. However, this is not the case (see Figure 5.4). The same phenomenon has been also found in TL glow curves in YPO_4 reported by Bos[12]. This may indicate that the shape of curve 2 in Figure 5.2 needs a minor adjustment regarding the value for the ground state Nd^{2+}.

The agreement of the VRBE diagram prediction and TL experiments prove that indeed the Ln^{3+} (Ln= Er, Nd, Ho, Dy, and Tm) codopants are the electron-trapping centers and Ce^{3+} is the recombination center in GdAlO₃:Ce^{3+}, Ln^{3+}. During heating the electrons release from the lanthanide codopants and return through the conduction band to eventually recombine with Ce^{4+} producing emission from Ce^{3+}.

5.5.2 Hole trapping and hole release
In Figure 5.5 a comparison was made of samples with the same hole-trapping center (Tb) but different electron-trapping centers (Eu, Sm and Yb). All the samples show TL glow peaks at the same temperature (peak 1, peak 2 and peak 4 as assigned above) but with significantly different emission spectra. Peak 1 and 2 can be monitored in all the samples shown in Figure 5.5, Figure 5.6 and Figure S5.3. Therefore, those peaks are assigned to an unidentified host related hole traps. Peak 4 appears only in the samples codoped with Tb. The trap depth of peak 4 has been calculated as 1.28 ± 0.02 eV shown in Table 5.1. The estimated Eu^{2+}, Sm^{2+} and Yb^{2+} electron trap depths are 3.08 eV, 1.83 eV and 2.65 eV, thus much deeper than the trap depth for peak 4. The VRBE diagram predicts that the Tb^{3+} ground

state is above the VB and Tb^{3+} may act as a hole-trapping center. During the TL readout, the activation energy needed to release holes from Tb^{4+} (1.28 ± 0.02 eV) is smaller than to release electrons from the electron-trapping centers. Therefore, the holes release from Tb^{4+} earlier than electrons from Eu^{2+}, Sm^{2+} or Yb^{2+} producing characteristic Eu^{3+}, Sm^{3+} or Yb^{3+} 4f-4f emission.

A new peak (peak 3) appears in the Pr-codoped samples (Figure 5.6). Again, no emission from Pr^{3+} can be found in the TLEM spectra shown in Figure S5.3b and e. This confirms that Pr^{3+} is not the recombination center. The trap depth of peak 3 is 1.33 ± 0.03 eV as shown in Table 5.1, which is also much smaller than the electron trap depth of Eu^{2+} and Sm^{2+}. Considering that the ground state energy of Pr^{3+} and Tb^{3+} in the VRBE diagram is quite similar, also Pr^{3+} acts as the hole-trapping center. No Yb^{3+} emission was monitored in (Yb, Pr) codoped sample. The explanation can be the energy transfer from Yb^{3+} $^2F_{7/2}$ to Pr^{3+} $^1G_4$ level that quenches the Yb^{3+} emission.

Ce^{3+} also acts as the hole-trapping center according to the VRBE diagram. However, that trap is too deep to release a hole in the measurement range which explains that no TL extra peak(s) can be observed related to hole release from Ce^{4+} (Figure 5.6, Figure S5.33c and f).

The trap depth for Tb^{4+} and Pr^{4+} in Table 5.1 are 1.28 ± 0.02 eV and 1.33 ± 0.03 eV which are lower than predicted by the VRBE diagram (1.61 eV and 1.44 eV for Tb^{4+} and Pr^{4+}). The explanation can be that the released holes are not moving through the valence band but form a so-called V_k center (a hole shared between two oxygen ions). The migration of a V_k center is thermally activated and it will migrate to recombine at Eu^{2+}, Sm^{2+} or Yb^{2+} generating characteristic Eu^{3+}, Sm^{3+} or Yb^{3+} 4f-4f emission.

The thermoluminescence excitation (TLE) spectrum in Figure 5.8 shows a broad band centerd at ~315 nm which coincides with the Eu^{3+} CT-band in Figure 5.2a. During CT-band excitation electrons are excited from the valence band to the Eu^{2+} $4f^7(^8S_{7/2})$ ground state leaving a hole in the valence band. Those holes can be captured by Tb^{3+} to become Tb^{4+}. Some holes will be also captured by the host-related hole-trapping center. In $LaAlO_3$, Tb^{3+} will provide a very shallow hole trap depth, and they will be released immediately at room temperature. During the TL

readout, the holes release from the hole-trapping centers, forming the V_k center and recombine with Eu^{2+} producing Eu^{3+} characteristic emission.

5.5.3 Engineering the trap depth by valence band tailoring

The above discussion of the hole-trapping and hole-release process confirms that the trap depths of the Tb^{3+} and Pr^{3+} hole-trapping centers are related to the valence band maximum energy, indicating that the TL glow curves can be shifted by engineering the valence band.

Figure 5.11 shows the VRBE diagrams for $Gd_{1-x}La_xAlO_3$ with different fraction of x. The data to construct the diagrams are listed in Table 5.4. The VRBE in the 4f ground state of Eu^{2+} ($E_{Eu}{}^{2+}$) is fixed at -3.98 eV because changes of $E_{Eu}{}^{2+}$ [22-23] within the same type of compounds are insignificant. The charge transfer energy of Eu^{3+} in $Gd_{1-x}La_xAlO_3$ is shown in Figure 5.2 and the detailed data are listed in Table 5.4. The decrease of the charge transfer energy of Eu^{3+} implies that the valence band maxima increases (Table 5.4). The ground state energy of Tb^{3+} and Pr^{3+} is like that for Eu^{2+} fixed for all the compounds.
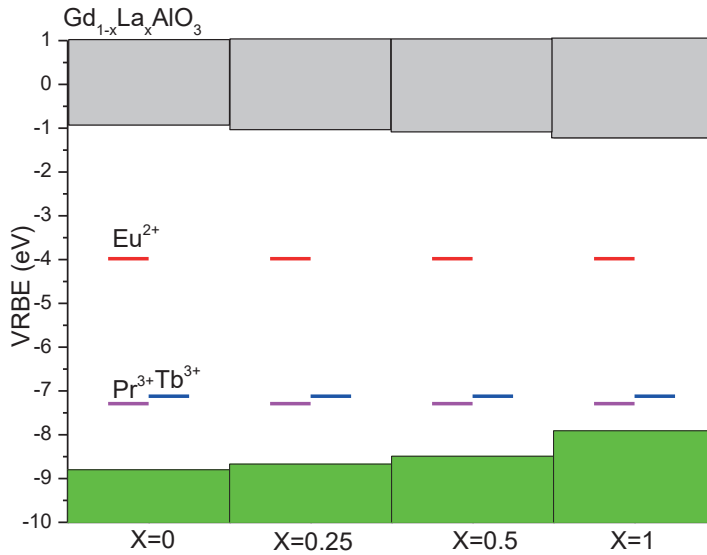

Figure 5.11. VRBE diagram of $Gd_{1-x}La_xAlO_3$ (x=0, 0.25, 0.5 and 1).

Figure 5.11 displays that the valence band goes upward and the energy difference between Tb^{3+}/Pr^{3+} ground states and the valence band maxima decreases with

increasing lanthanum concentration. The diagram agrees with the observed TL peak shift in Figure 5.7 where the Tb TL peak (peak 4) shifts from 415 ± 5 K (1.28 ± 0.02 eV) for x=0 to 365 ± 15 K (1.12 ± 0.05 eV) for x=0.5. A large uncertainty exists for x=0.25 and x=0.5 samples due to the very broad TL glow curves that make it tough to identify the exact TL peak maximum. The TL glow curves also shift to lower temperature with increasing lanthanum concentration in Figure 5.7b. However, the Pr TL peak can be only distinguished for x=0. The missing of peak 4 for x=1 (LaAlO$_3$:Eu^{3+},Tb^{3+}/Pr^{3+}) is due to the very shallow hole trap depth in Pr^{4+} and Tb^{4+} creating a TL peak far below the room temperature.

The ground state level of Pr^{3+} is ~0.17 eV lower than that of Tb^{3+} shown in the VRBE diagram, indicating that the TL glow peak maximum temperature of Pr^{3+} should be at a lower temperature than the one of Tb^{3+}. However, the TL experiments displays that the Pr TL peak (peak 3) T_m is ~10 K higher than that of the Tb peak (peak 4) shown in Figure 5.6 and Table 5.1.

Table 5.4. Parameters to construct the VRBE diagram of Gd$_{1-x}$La$_x$AlO$_3$:Tb^{3+}/Pr^{3+}, Eu^{3+} (x=0, 0.25, 0.5 and 1). The units for all the parameters are all eV.

X	E^{ex}	E^{CT}	E_V	E_C	$E_{Tb}{}^{3+}$	$E_{Pr}{}^{3+}$
0	7.29	4.86	-8.80	-0.92	-7.12	-7.29
0.25	7.08	4.68	-8.67	-1.02	-7.12	-7.29
0.5	6.88	4.48	-8.49	-1.05	-7.12	-7.29
1	6.36	3.93	-7.91	-1.22	-7.12	-7.29

So far, we conclude that the trap depth of Tb hole-trapping centers can be engineered by valence band tailoring with substitution of gadolinium by lanthanum.

5.6 Conclusion

The trapping and detrapping process of electrons and holes have been studied in this paper. In GdAlO$_3$:Ce^{3+}, Ln^{3+} (Ln= Er, Nd, Ho, Dy and Tm), the Ln^{3+} codopants are the electron-trapping centers and Ce^{3+} is the hole-trapping center as well as the recombination center. The captured electrons released from Ln^{2+} recombine with Ce^{4+} producing Ce^{3+} 5d-4f emission (at 343 nm and 362 nm). For GdAlO$_3$:Ln^{3+},

RE^{3+} (Ln=Sm, Eu and Yb, RE= Ce, Pr and Tb), the Ln^{3+} is the electron-trapping center as well as the recombination center and RE^{3+} is the hole-trapping center. The holes release earlier (i.e. at lower temperature) than electrons and therefore recombine with Ln^{2+} generating Ln^{3+} 4f-4f characteristic emission during TL readout. The energy of the valence band maximum can be engineered by substitution of Gd by La therefore adjusting the trap depth of Tb^{3+}. Such valence band engineering may be a potential method to "deliberately design" the hole traps for afterglow phosphors.

5.7 Acknowledgements

5.8 Reference

1. Aitasalo, T.; Hölsä, J.; Krupa, J. C.; Lastusaari, M.; Niittykoski, J., Persistent Luminescence Materials. In *Physics of Laser Crystals*, Krupa, J.-C.; Kulagin, N., Eds. Springer Netherlands: 2003; Vol. 126, pp 35-50.

2. Van den Eeckhout, K.; Smet, P. F.; Poelman, D., Persistent Luminescence in Eu2+ Doped Compounds a Review. *Materials* 2010, *3*, 2536-2566.

3. Van den Eeckhout, K.; Poelman, D.; Smet, P., Persistent Luminescence in Non-Eu2+-Doped Compounds: A Review. *Materials* 2013, *6*, 2789-2818.

4. Leblans, P.; Vandenbroucke, D.; Willems, P., Storage Phosphors for Medical Imaging. *Materials* 2011, *4*, 1034-1086.

5. Ueda, J.; Dorenbos, P.; Bos, A.; Kuroishi, K.; Tanabe, S., Control of Electron Transfer between Ce3+ and Cr3+ in Y3Al5-xGaxO12 Host by Conduction Band Engineering. *Journal of Materials Chemistry C* 2015, *3*, 5642-5651.

6. Luo, H.; Bos, A. J. J.; Dobrowolska, A.; Dorenbos, P., Low-Temperature Vuv Photoluminescence and Thermoluminescence of UV Excited Afterglow Phosphor Sr3Alxsi1-xO5:Ce3+,Ln3+ (Ln = Er, Nd, Sm, Dy and Tm). *Physical Chemistry Chemical Physics* 2015, *17*, 15419-15427.

7. Korthout, K.; Van den Eeckhout, K.; Botterman, J.; Nikitenko, S.; Poelman, D.; Smet, P. F., Luminescence and X-Ray Absorption Measurements of Persistent SrAl2O4:Eu,Dy Powders: Evidence for Valence State Changes. *Physical Review B* 2011, *84*, 085140.

8. Botterman, J.; Joos, J. J.; Smet, P. F., Trapping and Detrapping in SrAl2O4:Eu,Dy Persistent Phosphors: Influence of Excitation Wavelength and Temperature. *Physical Review B* 2014, *90*, 085147.

9. Xu, J.; Ueda, J.; Tanabe, S., Design of Deep-Red Persistent Phosphors of Gd3Al5-xGaxO12:Cr3+ Transparent Ceramics Sensitized by Eu3+ as an Electron Trap Using Conduction Band Engineering. *Optical Materials Express* 2015, *5*, 963-968.

10. Zhuang, Y.; Ueda, J.; Tanabe, S., Tunable Trap Depth in Zn(Ga1-xAlx)2O4:Cr,Bi Red Persistent Phosphors: Considerations of High-Temperature Persistent Luminescence and Photostimulated Persistent Luminescence. *Journal of Materials Chemistry C* 2013, *1*, 7849-7855.

11. Chakrabarti, K.; Mathur, V. K.; Rhodes, J. F.; Abbundi, R. J., Stimulated Luminescence in Rare-Earth-Doped MgS. *Journal of Applied Physics* 1988, *64*, 1363-1366.

12. Bos, A. J. J.; Dorenbos, P.; Bessière, A.; Lecointre, A.; Bedu, M.; Bettinelli, M.; Piccinelli, F., Study of Tl Glow Curves of YPO4 Double Doped with Lanthanide Ions. *Radiation Measurements* 2011, *46*, 1410-1416.

13. Kowalczyk, S. P.; Cheung, J. T.; Kraut, E. A.; Grant, R. W., CdTe-HgTe Heterojunction Valence-Band Discontinuity: A Common-Anion-Rule Contradiction. *Physical Review Letters* 1986, *56*, 1605-1608.

14. Wei, S.-H.; Zunger, A., Role of D Orbitals in Valence-Band Offsets of Common-Anion Semiconductors. *Physical Review Letters* 1987, *59*, 144-147.

15. Li, Y.-H.; Walsh, A.; Chen, S.; Yin, W.-J.; Yang, J.-H.; Li, J.; Da Silva, J. L. F.; Gong, X. G.; Wei, S.-H., Revised Ab Initio Natural Band Offsets of All Group Iv, Ii-Vi, and Iii-V Semiconductors. *Applied Physics Letters* 2009, *94*, 212109.

16. Cai, Z.-H.; Narang, P.; Atwater, H. A.; Chen, S.; Duan, C.-G.; Zhu, Z.-Q.; Chu, J.-H., Cation-Mutation Design of Quaternary Nitride Semiconductors Lattice-Matched to Gan. *Chemistry of Materials* 2015, *27*, 7757-7764.

17. Xiaobo Chen, S. S., Liejin Guo, and Samuel S. Mao, Semiconductor-Based Photocatalytic Hydrogen Generation. *Chemical Reviews* 2010,, *110*, 6503–6570.

18. Dorenbos, P., Modeling the Chemical Shift of Lanthanide 4f Electron Binding Energies. *Physical Review B* 2012, *85*, 165107.

19. Dorenbos, P., Electronic Structure Engineering of Lanthanide Activated Materials. *Journal of Materials Chemistry* 2012, *22*, 22344.

20. P.Dorenbos, A Review on How Lanthanide Impurity Levels Change with Chemistry and Structure of Inorganic Compounds. *ECS Journal of Solid State Science and Technology* 2013, R3001-R3011.

21. Dorenbos, P.; Rogers, E. G., Vacuum Referred Binding Energies of the Lanthanides in Transition Metal Oxide Compounds. *ECS Journal of Solid State Science and Technology* 2014, *3*, R150-R158.

22. Pieter, D., The Electronic Level Structure of Lanthanide Impurities in Repo 4 , REBO3, REAlO3 , and RE2O3 (RE = La, Gd, Y, Lu, Sc) Compounds. *Journal of Physics: Condensed Matter* 2013, *25*, 225501.

23. Dorenbos, P., The Electronic Structure of Lanthanide Doped Compounds with 3d, 4d, 5d, or 6d Conduction Band States. *Journal of Luminescence* 2014, *151*, 224-228.

24. Dorenbos, P., Lanthanide 4f Electron Binding Energies and the Nephelauxetic Effect in Wide Band Gap Compounds. *Journal of Luminescence* 2013, *136*, 122-129.

25. Du Boulay, D.; Ishizawa, N.; Maslen, E. N., GdAlO3 Perovskite. *Acta Crystallographica Section C* 2004, *60*, i120-i122.

26. Dobrowolska, A.; Bos, A. J. J.; Dorenbos, P., Electron Tunnelling Phenomena in YPO4:Ce,Ln (Ln = Er, Ho, Nd, Dy). *Journal of Physics D: Applied Physics* 2014, *47*, 335301.

27. Verweij, J. W. M.; Cohen-Adad, M. T.; Bouttet, D.; Lautesse, H.; Moine, B.; Pédrini, C., Luminescence Properties of GdAlO3: Ce Powders. Dependence on Reduction Conditions. *Chemical Physics Letters* 1995, *239*, 51-55.

28. Lim, S.-G.; Kriventsov, S.; Jackson, T. N.; Haeni, J. H.; Schlom, D. G.; Balbashov, A. M.; Uecker, R.; Reiche, P.; Freeouf, J. L.; Lucovsky, G., Dielectric Functions and Optical Bandgaps of High-K Dielectrics for Metal-Oxide-Semiconductor Field-Effect Transistors by Far Ultraviolet Spectroscopic Ellipsometry. *Journal of Applied Physics* 2002, *91*, 4500-4505.

29. Mi, Y. Y.; Yu, Z.; Wang, S. J.; Lim, P. C.; Foo, Y. L.; Huan, A. C. H.; Ong, C. K., Epitaxial Laalo3 Thin Film on Silicon: Structure and Electronic Properties. *Applied Physics Letters* 2007, *90*, 181925.

30. Edge, L. F.; Schlom, D. G.; Chambers, S. A.; Cicerrella, E.; Freeouf, J. L.; Holländer, B.; Schubert, J., Measurement of the Band Offsets between Amorphous LaAlO3 and Silicon. *Applied Physics Letters* 2004, *84*, 726-728.

31. Ohtomo, A.; Hwang, H. Y., A High-Mobility Electron Gas at the LaAlO3/SrTiO3 Heterointerface. *Nature* 2004, *427*, 423-426.

32. Oliveira, H. H. S.; Cebim, M. A.; Da Silva, A. A.; Davolos, M. R., Structural and Optical Properties of GdAlO3:RE3+ (RE = Eu or Tb) Prepared by the Pechini Method for Application as X-Ray Phosphors. *Journal of Alloys and Compounds* 2009, *488*, 619-623.

33. Krumpel, A. H.; Bos, A. J. J.; Bessière, A.; van der Kolk, E.; Dorenbos, P., Ontrolled Electron and Hole Trapping in YPO4:Ce3+,Ln3+ and LuPO4:Ce3+,Ln3+ (Ln=Sm, Dy, Ho, Er, Tm). *Physical Review B* 2009, *80*, 085103.

34. Azorín, J., Determination of Thermoluminescence Parameters from Glow Curves—I. A Review. *International Journal of Radiation Applications and Instrumentation. Part D. Nuclear Tracks and Radiation Measurements* 1986, *11*, 159-166.

35. Bos, A. J. J.; Dorenbos, P.; Bessière, A.; Viana, B., Lanthanide Energy Levels in YPO4. *Radiation Measurements* 2008, *43*, 222-226.

36. Tasker, P. W.; Stoneham, A. M., An Appraisal of the Molecular Model for the Vk Centre. *Journal of Physics and Chemistry of Solids* 1977, *38*, 1185-1189.

37. Murray, R. B.; Keller, F. J., Recombination Luminescence from VK Centers in Potassium Iodide. *Physical Review* 1965, *137*, A942-A948.

38. Gazzinelli, R.; Ribeiro, G. M.; de Siqueira, M. L., Esr and Endor Studies of the Vk Center in SrF2. *Solid State Communications* 1973, *13*, 1131-1134.

39. Mott, N. F.; Stoneham, A. M., The Lifetime of Electrons, Holes and Excitons before Self-Trapping. *Journal of Physics C: Solid State Physics* 1977, *10*, 3391.
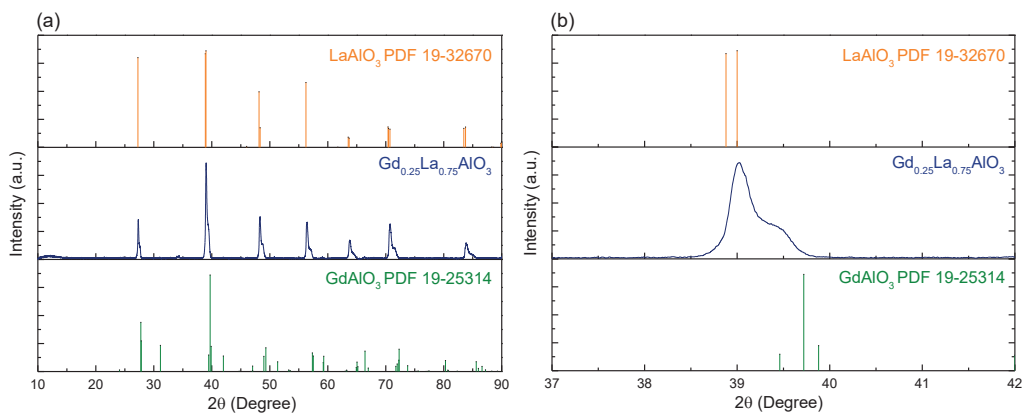
5.9 Supporting information

Figure S5.1. (a) the XRD pattern of the as-prepared $Gd_{0.25}La_{0.75}AlO_3$, (b) the detailed XRD pattern from 37 to 42 °.
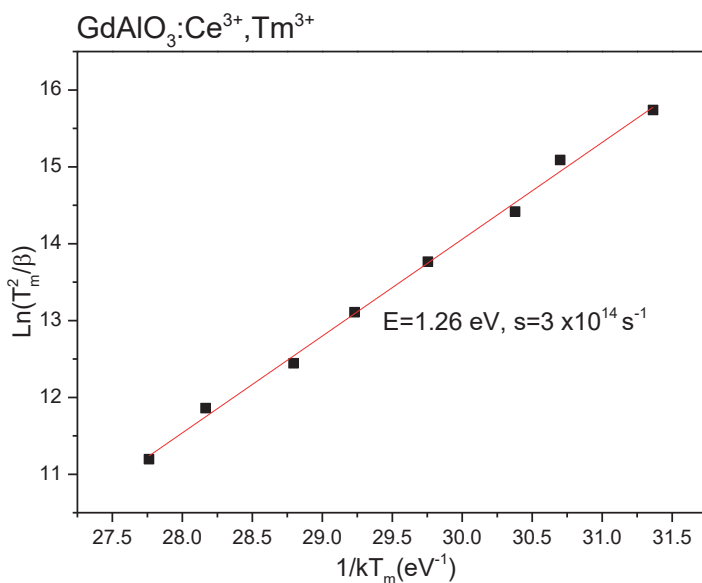

Figure S5.2. Arrhenius Plot of $GdAlO_3:0.01Ce^{3+}$, $0.01Tm^{3+}$ derived by determining the glow peak maximum temperature T_m for different heating rates β. The applied heating rates were 2.4, 1.2, 0.64, 0.32, 0.16, 0.08, 0.04 and 0.02 K/s. All the samples were recorded by the RISØ TL-reader from 300 to 700 K with 1600 s irradiation by its β source. The TL glow curves were measured with a Hoya 3 mm C5-58 bandpass filter from about 350 to 470 nm to transmit the 5d-4f Ce^{3+} emission (at 343 nm and 362 nm) efficiently.
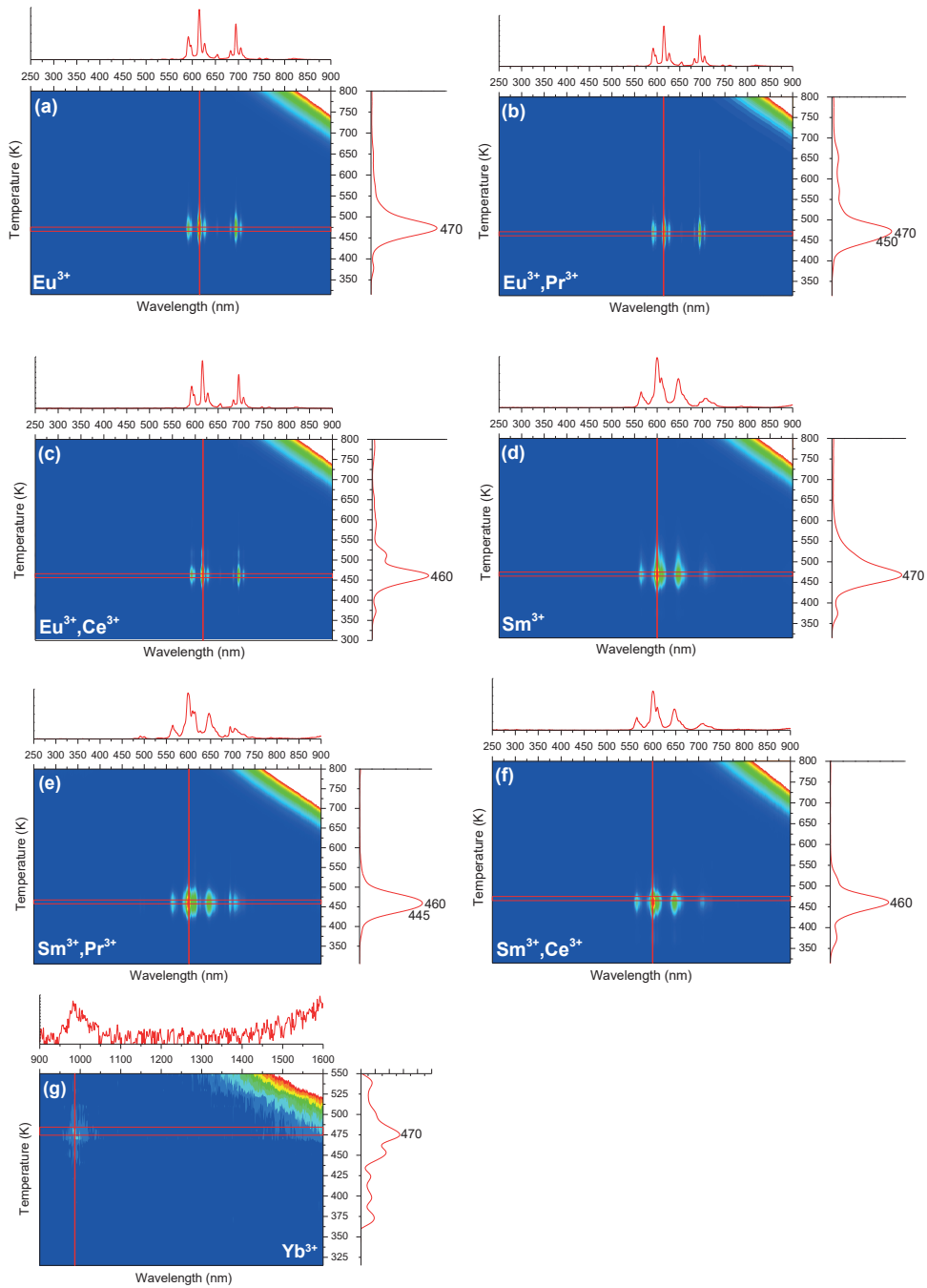
107

Figure S5.3. The thermoluminescence emission (TLEM) spectra of (a) $GdAlO_3:0.01Eu^{3+}$, (b) $GdAlO_3:0.01Eu^{3+},0.01Pr^{3+}$, (c) $GdAlO_3:0.01Eu^{3+},0.01Ce^{3+}$, (d) $GdAlO_3:0.Sm^{3+}$, (e) $GdAlO_3:0.01Sm^{3+},0.01Pr^{3+}$, (f) $GdAlO_3:0.01Sm^{3+},0.01Ce^{3+}$, (g) $GdAlO_3:0.01Yb^{3+}$. The samples (a) and (f) were measured by the UV/vis spectrometer (Ocean Optics, QE65000) from 300 to 800 K, sample (g) was measured by the NIR spectrometer (Ocean Optics, NIRQ512) from 300 to 550 K. The heating rate for all of these samples is 5 K/s after exposure to irradiation of 2.5 kGy from a ^{60}Co source.
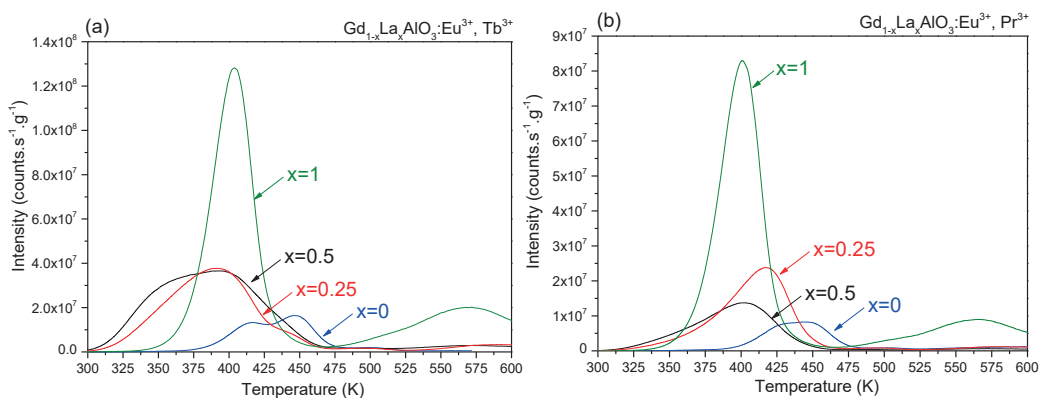

Figure S5.4. Unnormalized thermoluminescence glow curves of (a) $Gd_{1-x}La_xAlO_3:0.01Eu^{3+},0.01Tb^{3+}$ and (b) $Gd_{1-x}La_xAlO_3:0.01Eu^{3+},0.01Pr^{3+}$. Both figures were measured by the RISØ TL-reader from 300 to 600 K with 1600 s irradiation by its β source and corrected by the mass. The heating rate was 1 K/s for all TL-recordings. A 600 nm bandpass filter (600FS40-50) was placed between the sample and PMT.
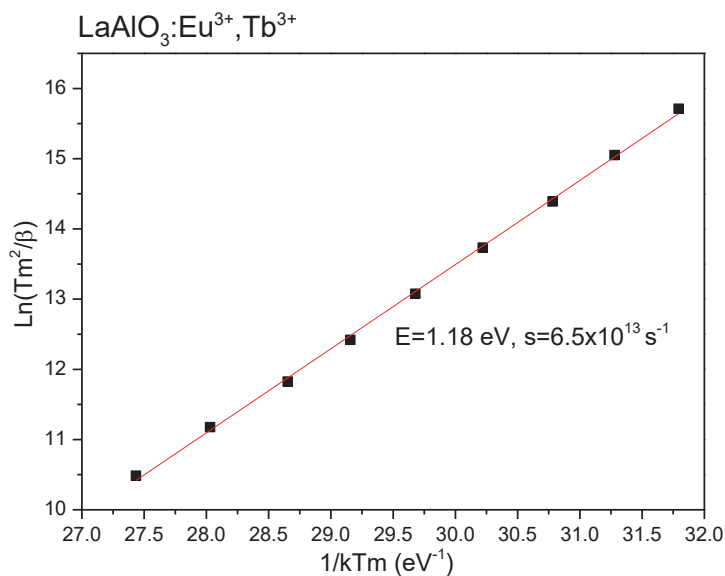
Figure S5.5. Arrhenius Plot of LaAlO$_3$:0.01Tb^{3+}, 0.01Eu^{3+} by determining the glow peak maximum temperature T_m for different heating rates β. The applied heating rates were 5.0, 2.4, 1.2, 0.64, 0.32, 0.16, 0.08, 0.04 and 0.02 K/s. All the samples were recorded by the RISØ TL-reader from 300 to 600 K with 1600 s irradiation by its β source. A 600 nm bandpass filter (600FS40-50) was placed between the sample and PMT in order to select the Eu^{3+} emission.

6

Charge Carrier Trapping Processes in RE$_2$O$_2$S (RE=La, Gd, Y and Lu)

6.1 Abstract

Two different charge carrier trapping processes have been investigated in $RE_2O_2S:Ln^{3+}$ (RE= La, Gd, Y and Lu; Ln= Ce, Pr and Tb) and $RE_2O_2S:M$ (M= Ti^{4+} and Eu^{3+}). Cerium, praseodymium and terbium act as recombination centers and hole trapping centers while host intrinsic defects provide the electron trap. The captured electrons released from the intrinsic defects recombine at Ce^{4+}, Pr^{4+} or Tb^{4+} *via* the conduction band. On the other hand, Ti^{4+} and Eu^{3+} act as recombination centers and electron trapping centers while host intrinsic defects act as hole trapping centers. For these codopants we find evidence that recombination is by means of hole release instead of electron release. The released holes recombine with the trapped electrons on Ti^{3+} or Eu^{2+} and yield broad Ti^{4+} yellow-red charge transfer (CT) emission or characteristic Eu^{3+} 4f-4f emission. We will conclude that the afterglow in $Y_2O_2S:Ti^{4+}$, Eu^{3+} is due to hole release instead of more common electron release.

6.2 Introduction

Charge carrier trapping and detrapping processes are of great interest in the luminescence research field both for an application and for a theoretical point of view[1]. Afterglow phosphors require that the captured electrons or holes are spontaneously released at room temperature to recombine at the luminescence center. Neither a too shallow nor a too deep trap will produce room temperature afterglow[2-3]. For storage materials used in X-ray imaging, deeper traps are needed to prevent thermal fading at room temperature[4].

The lanthanide dopant can either act as an electron or as a hole trapping center. Such electron trapping was reported as early as in the 1960s by McClure *et al*, who found that trivalent lanthanides in CaF_2 can be reduced to divalent under γ-irradiation[5]. In 2005, Dorenbos proposed that when the divalent lanthanide $4f^n$ ground state levels are below the conduction band (CB) the corresponding trivalent ions may act as electron trapping centers and as function of type of lanthanide codopant there is a predictable variation in trap depth[6]. Later, this hypothesis was experimentally confirmed by thermoluminescence (TL) studies of $YPO_4:Ce^{3+}$, Ln^{3+} (Ln = Pr, Nd, Sm, Dy, Ho, Er, Tm, and Yb) by Bos *et al*[7]. Here, Ce^{3+} acts as the hole trapping center as well as the recombination (luminescence) center while the

selected lanthanide codopants are the electron trapping centers. During the TL readout, the trapped electrons are released and move freely in the CB to eventually recombine at Ce^{4+}. Different lanthanide codopants have different TL glow peak maxima indicating different trap depth. The same phenomenon has been reported later in $Sr_3Al_xSi_{1-x}O_5:Ce^{3+}$, Ln^{3+} (Ln = Er, Nd, Sm, Dy and Tm)[8], $Y_3Al_5O_{12}$: Ln^{3+}, RE^{3+} (Ln= Ce^{3+}, Pr^{3+} and Tb^{3+}; RE= Eu^{3+} and Yb^{3+})[9] and $GdAlO_3:Ce^{3+}$, Ln^{3+} (Ln= Pr, Er, Nd, Ho, Dy and Tm)[10].

When the trivalent lanthanide $4f^n$ ground state levels are close above the VB, these ions may act as hole trapping centers. The captured holes can be released to recombine with a luminescence center *via* the VB or as a migrating V_k center. Compared to the many reports on electron trapping and detrapping processes, there are much less reports that discuss hole trapping and detrapping processes. One of the few is by Chakrabarti *et al* in the 1980s who found that during UV irradiation of $MgS:Ce^{3+}$, Sm^{3+} the holes are captured by cerium and electrons by samarium. After hole release, they recombine with samarium producing Sm^{3+} characteristic emission during the TL readout[11]. The other example is from our own studies on $Gd_{1-x}La_xAlO_3:Eu^{3+},Tb^{3+}$ where Tb^{3+} acts as the hole trapping center and Eu^{3+} as the electron trapping center. The captured holes release from Tb^{4+} earlier than electrons from Eu^{2+} and recombine with Eu^{2+} producing Eu^{3+} characteristic 4f-4f emission. Another example of hole detrapping is given by Bos et al. in $YPO_4:Tb^{3+}$, RE^{3+} (RE^{3+} = Nd, Ho and Dy) where again Tb^{3+} is acting as a hole trapping center and RE^{3+} as electron tapping center[7].

Eu^{2+} and Ce^{3+} are the most widely used recombination (luminescence) centers in afterglow materials. For instance, $SrAl_2O_4:Eu^{2+},Dy^{3+}$ [12], $CaAl_2O_4:Eu^{2+},Nd^{3+}$ [13], $CaS:Eu^{2+},Dy^{3+}$ [14], $Ca_2Si_5N_8:Eu^{2+},Tm^{3+}$ [15] and $Y_3Al_{5-x}Ga_xO_{12}:Ce^{3+},Cr^{3+}$ [16]. The 5d excited levels of divalent europium or trivalent cerium are located very close to the CB in those compounds, and therefore excited electrons are easily released into the CB and subsequently caught by a trivalent lanthanide or Cr^{3+} cation[1]. The trapped electrons are released slowly and recombine with the europium or cerium recombination center to generate Eu^{2+} or Ce^{3+} emission. In these cases, the afterglow mechanism is due to the electron trapping and electron release.

In 2003, Kang *et al* reported on the afterglow material of $Y_2O_2S:Mg^{2+}$, Ti^{4+} that shows a unique orange broad band persistent luminescence centered at ~595 nm

after 380 nm UV excitation[17]. After that, dozens of reports were published to modify or improve this material. For instance, $Y_2O_2S:Eu^{3+},Mg^{2+},Ti^{4+}$ [18] and $Gd_2O_2S:Eu^{3+},Mg^{2+},Ti^{4+}$ [19] were synthesized and show afterglow emission both from Eu^{3+} and Ti^{4+}.

Different to Eu^{2+} and Ce^{3+}, Eu^{3+} can only act as an electron acceptor. The same applies to Ti^{4+} with the $3d^0$ electron configuration. If neither Eu^{3+} nor Ti^{4+} can be an electron donor then what is the electron donor in phosphors like $Y_2O_2S:Eu^{3+},Mg^{2+},Ti^{4+}$ and $Gd_2O_2S:Eu^{3+},Mg^{2+},Ti^{4+}$? Where and how are the electrons captured? How are these electrons released and why is the afterglow from Ti^{4+} and Eu^{3+}?

Several studies were carried out to analysis the afterglow mechanism of $Y_2O_2S:Eu^{3+},Mg^{2+},Ti^{4+}$. Hölsä et al found that the afterglow emission is from Eu^{3+} and Ti^{3+} but did not explain the afterglow mechanism[20]. Zhou et al observed that the afterglow is from Eu^{3+} and Ti^{4+}, and the traps that contribute to the afterglow are complex Ti related traps[18]. Lei et al studied the thermoluminescence of $Gd_2O_2S:RE^{3+}$, Ti, Mg (RE = Ce, Pr, Nd, Sm, Eu, Tb, Dy, Ho, Er, Tm and Yb)[21]. Lei et al proposed that UV-light exposure causes an electronic transition from the ground state of the RE^{3+} to the excited state, and simultaneously electrons and holes are created in the host. Then the captured electrons return back to the exited states of RE^{3+} at room temperature resulting in characteristic f–f persistent afterglow emission. Since the $4f^n$ states of the lanthanide ions are localized impurity states, after excitation of RE^{3+} to the excited state one may not interpret that the 4f state leaves a hole in the host lattice that can be filled by another electron[22]. Therefore, the transition suggested by Lei et al is highly unlikely.

The objective of this study is to reveal the trapping and detrapping processes of electrons and holes in $RE_2O_2S:M$ (RE= La, Gd, Y and Lu; M= Ce^{3+}, Pr^{3+}, Tb^{3+}, Eu^{3+} and Ti^{4+}) materials. Photoluminescence emission (PL) and excitation (PLE) spectra of Eu^{3+} or Ti^{4+} single doped samples have been measured to construct the vacuum referred binding energy (VRBE) diagrams showing the lanthanide and titanium levels within the band gap. Thermoluminescence emission (TLEM) and thermoluminescence (TL) measurements were performed to identify the recombination centers and to derive the trap depths. Thermoluminescence excitation (TLE) spectra were measured to analyze the charging process of Eu^{3+} or

Ti^{4+} single doped samples. Finally, to show how the obtained knowledge can be applied, the results are used to propose the persistent luminescence mechanism of $Y_2O_2S: Ti^{4+}, Eu^{3+}$.

6.3 Experimental

All starting materials were purchased from Sigma-Aldrich and used without further treatment. The materials were synthesized by mixing of 5 N (99.999%) purity rare earth oxides, S (99.5%), TiO_2 (99.99%) and Na_2CO_3 (99.99%) and fired from 1150 to 1250°C during 4 to 8 h one or two times in a corundum crucible in CO atmosphere. The obtained compounds were washed by deionized water a couple of times to remove the Na_2CO_3 flux. The content of Na_2CO_3 is 7% by weight.

All powders were checked with a PANalytical XPert PRO X-ray diffraction system with a Co Kα (λ = 0.178901 nm) X-ray tube (45 kV, 40 mA). The PL spectra of Ti doped samples were measured by a UV to VIS spectrometer (Ocean Optics, QE65000) with a UV LED (365 nm, 780 mW) excitation. The PLE spectra of Ti doped samples and the PLE and PL spectra for all the Eu^{3+} doped samples were measured with a setup that consists of an UV/vis branch with a 500W Hamamatsu CW Xe lamp and Gemini 180 monochromator. The PerkinElmer MP-1913 photomultiplier was exploited as a detector connected at the exit slit of a Princeton Acton SP2300 monochromator.

Low-temperature TL measurements (90-450 K) were recorded with a sample chamber operating under vacuum (P = 10^{-7} mbar), a $^{90}Sr/^{90}Y$ β irradiation source having a dose rate of $\sim$0.4 mGy s^{-1} and a PerkinElmer channel PM tube (MP-1393). Liquid nitrogen was used as a cooling medium. A 600 nm bandpass filter (600FS40-50, Andover Corporation) was placed between the sample and the PMT during the measurements of Ce^{3+}, Pr^{3+}, Eu^{3+} and Ti^{4+} singly doped samples to transmit the red emission from the above dopants. For the Tb^{3+} doped samples, a 550 nm bandpass filter (550FS40-50, Andover Corporation) was placed between the sample and the PMT. TLEM spectra were measured using an UV to vis spectrometer (Ocean Optics, QE65000) with a HR composite grating (300 lines/mm) and an entrance aperture of 100 µm resulting in a 3.3 nm (fwhm) wavelength resolution. Samples were irradiated with a ^{60}Co gamma source to an absorbed dose of ~1.6 kGy[23].

The TL excitation spectra (TLE) were measured by first illuminating the samples during 600 s with monochromatic photons from a 150 W xenon arc lamp (Hamamatsu L2273) filtered by a 1/8 monochromator (Oriel Cornerstone 130) with wavelength resolution of 0.8 nm/0.1 mm slit width. The slit width was selected as 1 mm and the wavelength step was fixed as 10 nm. Next, the system is programmed by LabVIEW to record all the TL glow curves from room temperature to 350 °C for excitation wavelengths between 200 nm and 450 nm. The plot of the integrated TL glow peaks versus the excitation wavelength is called a TL excitation spectrum[24]. The TL spectra were all recorded by a RISØ TL/OSL reader model DA-15 and a controller model DA-20. The same 600 nm bandpass filter (600FS40-50) was placed between the sample and PMT.

6.4 Results

6.4.1 X-Ray diffraction spectra and photoluminescence spectroscopy

The X-ray diffraction (XRD) patterns of as-prepared RE_2O_2S materials are shown in Figure 6.1. All samples are of single phase and match with the Y_2O_2S reference card (No. 382242) due to the same crystal structure (space group: P-3m1). A slight shift of the XRD patterns can be observed in Figure 6.1b due to different lattice parameters.
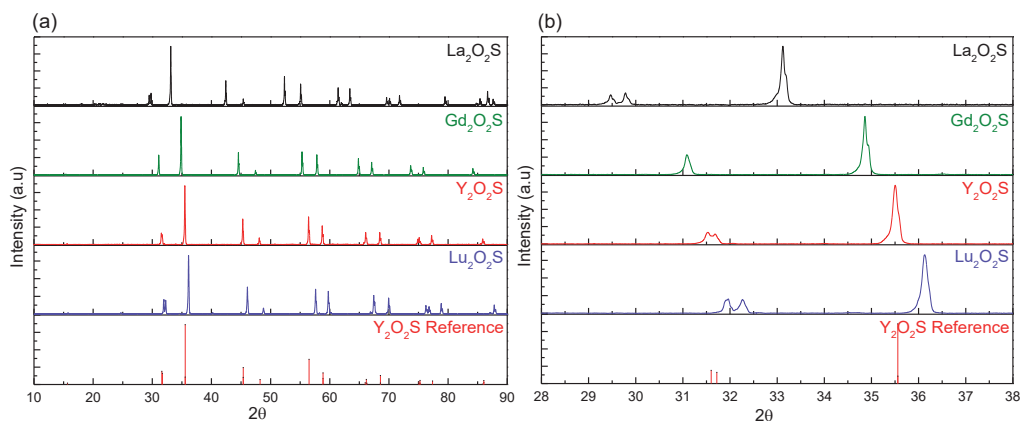

Figure 6.1. (a) XRD patterns of the as-prepared samples of La_2O_2S, Gd_2O_2S, Y_2O_2S and Lu_2O_2S. (b) Detailed XRD patterns in the range from 28 to 38°.

Figure 6.2 displays the PLE (a) and PL (b) spectra of Eu^{3+} single doped RE_2O_2S. All the samples have the characteristic Eu^{3+} 4f-4f emission. The host exciton

creation energy increases from 4.57 eV (271 nm) for La_2O_2S to 4.66 eV (266 nm) for Lu_2O_2S. Those exciton energies are similar to that in previous reports, i.e., 4.60 eV for La_2O_2S[25] and 4.71 eV for Lu_2O_2S[26]. The broad excitation band near 320-400 nm originates from electron transfer from the valence band (VB) to Eu^{3+}, also called the charge transfer (CT) band. It increases from 3.61 eV (343 nm) for La_2O_2S to 3.77 eV (329 nm) for Lu_2O_2S and shows the same tendency as the host exciton creation energy. The CT bands of Eu^{3+} in RE_2O_2S have fwhm (full width at half maximum) around 0.8 eV which is quite typical for Eu^{3+} CT bands[27-28].
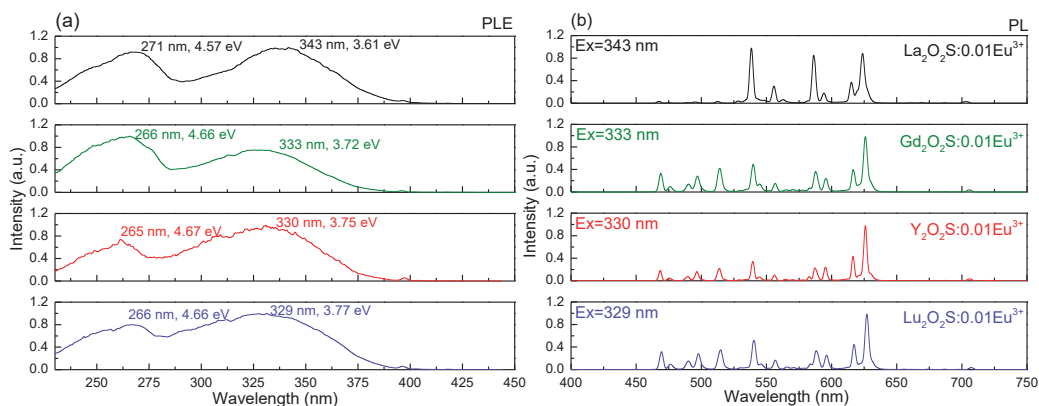
Figure 6.2. Room temperature PLE (a) and PL spectra (b) of $La_2O_2S{:}0.01Eu^{3+}$, $Gd_2O_2S{:}0.01Eu^{3+}$, $Y_2O_2S{:}0.01Eu^{3+}$ and $Lu_2O_2S{:}0.01Eu^{3+}$. The excitation spectra were recorded at 627 nm emission. The emission spectra were excited at the charge transfer peak maxima, which are labeled in the legend of Figure 6.2b. The numbers in the Figure 6.2a show the host exciton excitation maxima (left) and the charge transfer maxima (right).

Figure 6.3 illustrates the PLE (a) and PL (b) spectra of Ti^{4+} single-doped RE_2O_2S. All samples show a broad band emission with fwhm around 0.5 eV. The broad emission bands originate from the Ti^{4+} charge transfer emission. The Ti^{4+} emission red shifts from 555 nm for $La_2O_2S{:}Ti^{4+}$ to 635 nm for $Lu_2O_2S{:}Ti^{4+}$. Here a calibrated CCD spectrometer was used to measure the emission spectra since the PerkinElmer MP-1913 photomultiplier we used is not sensitivity to the red light. A comparison of $Y_2O_2S{:}Ti^{4+}$ emission spectra measured by the PerkinElmer MP-1913 PMT and the CCD are shown in Figure S6.1 in the Supporting Information.
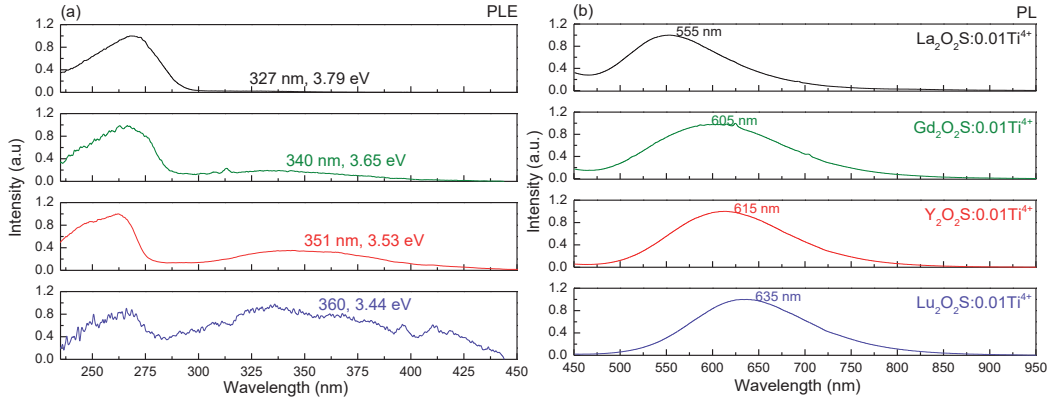
Figure 6.3. Room temperature PLE (a) and PL spectra (b) of $La_2O_2S:0.01Ti^{4+}$, $Gd_2O_2S:0.01Ti^{4+}$, $Y_2O_2S:0.01Ti^{4+}$ and $Lu_2O_2S:0.01Ti^{4+}$. The excitation spectra were measured at the emission maxima. The CT maxima are shown in the legend of Figure 6.3a. The emission spectra were recorder by a calibrated CCD spectrometer (Ocean Optics, QE65000) under the 365 nm UV-LED excitation.

The excitation spectra of Ti^{4+} are shown in the Figure 6.3a. Similar to that for Eu^{3+}, the broad band near 265 nm is the host exciton creation band and the one near 320-380 nm is the VB → Ti^{4+} charge transfer. The relative intensity of the Ti^{4+} CT excitation band (the ratio of Ti^{4+} CT intensity to the host exciton intensity) increases from La_2O_2S to Lu_2O_2S. The Ti^{4+} CT excitation band of $La_2O_2S:Ti^{4+}$ is weak at room temperature. Therefore, the low-temperature (10 K) photoluminescence excitation spectrum of $La_2O_2S:Ti^{4+}$ was measured and shown in Figure S6.2.

Figure S6.2 shows that at 10 K Ti^{4+} CT excitation band locates at ~327 nm (3.79 eV). Figure S6.3 shows that the temperature $T_{0.5}$ where Ti^{4+} emission intensity is quenched by 50% is at ~165 K. The activation energy for thermal quenching can be derived from[29]:

$$I(T) = \frac{I(0)}{1+C\exp(-\frac{E}{kT})} \qquad 6.1$$

where *I (T)* and *I (0)* is the luminescence intensity at temperature T and 0 and *E* indicates the activation energy. A fit through the data in Figure S6.3, as indicated by the solid curve provides the activation energy E = 0.05 eV.

118

Figure 6.3a shows that the Ti^{4+} CT excitation bands shift to longer wavelength from La_2O_2S (3.79 eV) to Lu_2O_2S (3.44 eV). Here we take the CT excitation band maxima as the Ti^{4+} CT energy and the numbers are displayed on the figure legend (Figure 6.3a). For $Lu_2O_2S:Ti^{4+}$, we use the centroid of the band near 360 nm (3.44 eV) as the Ti^{4+} CT energy.

6.4.2 Thermoluminescence emission spectra

Thermoluminescence emission (TLEM) spectra were measured for $RE_2O_2S:Ti^{4+}$ and $RE_2O_2S:Eu^{3+}$ in order to identify the luminescence and recombination center during the TL readout. Figure 6.4 shows two typical TLEM spectra of $Y_2O_2S:Ti^{4+}$ and $Y_2O_2S:Eu^{3+}$. Similar figures for RE=La, Gd and Lu can be found in Figure S6.4.
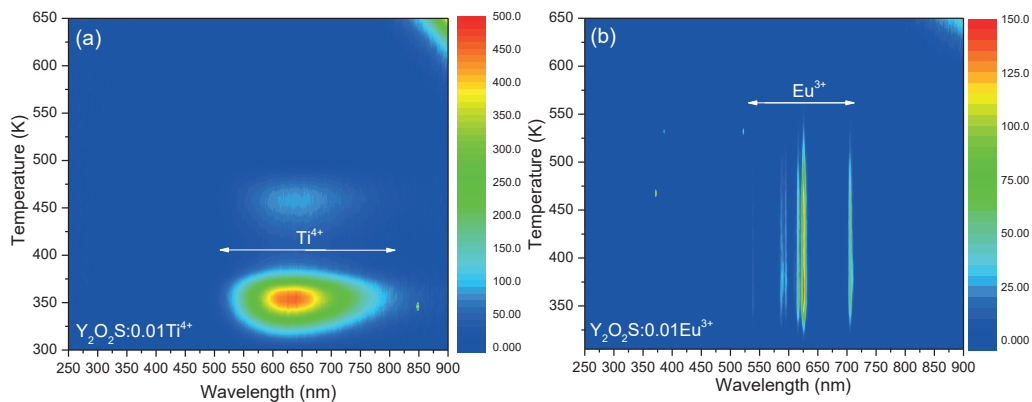
Figure 6.4. The thermoluminescence emission (TLEM) spectra of (a) $Y_2O_2S:0.01Ti^{4+}$ and (b) $Y_2O_2S:0.01Eu^{3+}$. The heating rate is 1 K/s after and each sample has been exposed to an irradiation dose of 1.6 kGy from a ^{60}Co source.

Two broad TL glow curves centered at ~350 and ~455 K can be observed for $Y_2O_2S:Ti^{4+}$ (Figure 6.4a). The TL emission spectra centered at ~615 nm matches with the photoluminescence emission spectra shown in Figure 6.3b, indicating that Ti acts as the recombination center leading to Ti^{4+} charge transfer emission. The Ti^{4+} TL emission can also be observed in the $Gd_2O_2S:Ti^{4+}$ (Figure S6.4a) and $Lu_2O_2S:Ti^{4+}$ (Figure S6.4b) although the later one shows much weaker Ti^{4+} TL intensity than the others. No Ti^{4+} TL emission was observed in $La_2O_2S:Ti^{4+}$, which is attributed to the almost complete thermal quenching of Ti^{4+} emission above room temperature (Figure S6.3). Characteristic red Eu^{3+} TL emission can be observed for $Y_2O_2S:Eu^{3+}$ (Figure 6.4b), $La_2O_2S:Eu^{3+}$ (Figure S6.4c), $Gd_2O_2S:Eu^{3+}$ (Figure

S6.4d) and $Lu_2O_2S:Eu^{3+}$ (Figure S6.4e). The observation of Eu^{3+} TL emission evidences that, like Ti^{4+}, Eu^{3+} acts as the recombination center.

6.4.3 Low-temperature thermoluminescence

Figure 6.5 displays the low-temperature TL glow curves of Y_2O_2S single doped with Tb^{3+}, Pr^{3+}, Ce^{3+}, Eu^{3+} or Ti^{4+}.
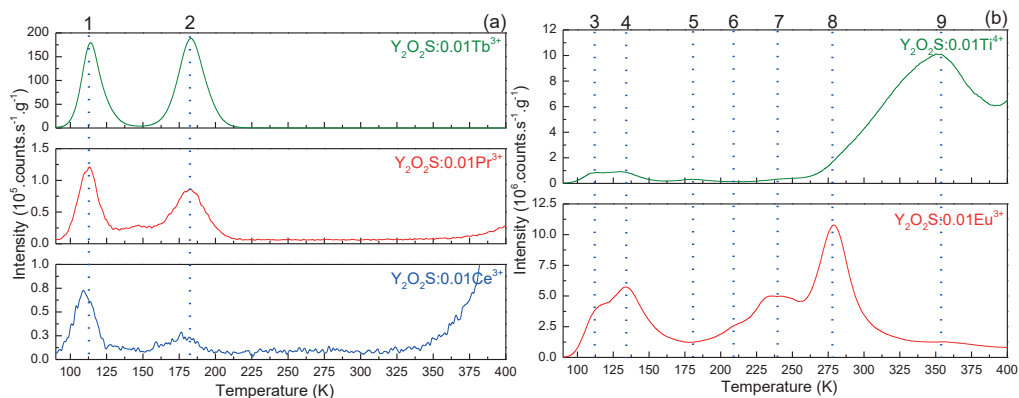

Figure 6.5 Low temperature thermoluminescence glow curves of (a) $Y_2O_2S:0.01Tb^{3+}$, $Y_2O_2S:0.0Pr^{3+}$ and $Y_2O_2S:0.0Ce^{3+}$, (b) $Y_2O_2S:0.01Ti^{4+}$ and $Y_2O_2S:0.01Eu^{3+}$. The heating rate was 1 K/s for all TL-recordings. The peak intensities are normalised by the mass of the sample.

Tb^{3+}, Pr^{3+} and Ce^{3+} single doped Y_2O_2S (Figure 6.5a) have the same glow peaks (herein referred to peaks 1 and 2) at ~115 K and ~182 K with different relative intensity. This implies that charge carriers are not released from Ce, Pr or Tb but from other trapping centers. The TL intensity of Ce^{3+} is around 3 orders of magnitude lower than that of Tb^{3+} which is due to the significant thermal quenching of Ce^{3+} emission at this temperature. Figure S6.5 shows that the temperature $T_{0.5}$ where Ce^{3+} emission intensity is quenched by 50% is at ~63 K. An Arrhenius fit of the quenching curve provides a 30 meV quenching energy barrier. The rising glow above 350 K in the $Y_2O_2S:Pr^{3+}$ and $Y_2O_2S:Ce^{3+}$ TL glow curves are due to blackbody radiation. No TL glow peaks are observed above 225 K in Figure 6.5a.

Figure 6.5b displays the TL glow curves for Ti^{4+} and Eu^{3+} single doped Y_2O_2S. Between 90 and 260 K both samples share the same TL glow peaks (numbered 3, 4, 5, 6, 7 and 8) indicating that charge carriers are released from the same type of

trapping centers not related to Eu or Ti. One observes a very broad TL glow starting from ~260 K and maximum at ~350 K in the Ti^{4+} doped sample which matches with that in the TLEM spectra (Figure 6.4a), and it contributes to the Ti^{4+} CT-luminescence afterglow. The Eu^{3+} doped sample shows like in Figure 6.4b the same glow at ~350 K that contributes to the afterglow although it is 1 order of magnitude less intense than that of the Ti^{4+} doped sample.

The trap depth E corresponding with the TL glow peaks numbered in Figure 6.5 was roughly estimated using the temperature T_m at the maximum of the glow and employing the first order kinetics equation

$$\frac{\beta E}{kT_m^2} = s \exp(-\frac{E}{kT_m}) \qquad 6.2$$

where $\beta = 1K \ s^{-1}$ is the heating rate, k is the Boltzmann constant (8.62 x 10^{-5} eV/K) , and s is the frequency factor (s^{-1})[30]. The frequency factor s, which is related to the host lattice vibrational mode, is estimated using the 444 cm^{-1} (1.3 x 10^{13} s^{-1})[31] R3 line from Y_2O_2S Raman spectroscopy and assumed to be the same for all the Y_2O_2S samples with different dopants. The TL parameters (frequency factor s, peak position T_m and trap depth E) are listed in Table 6.1.

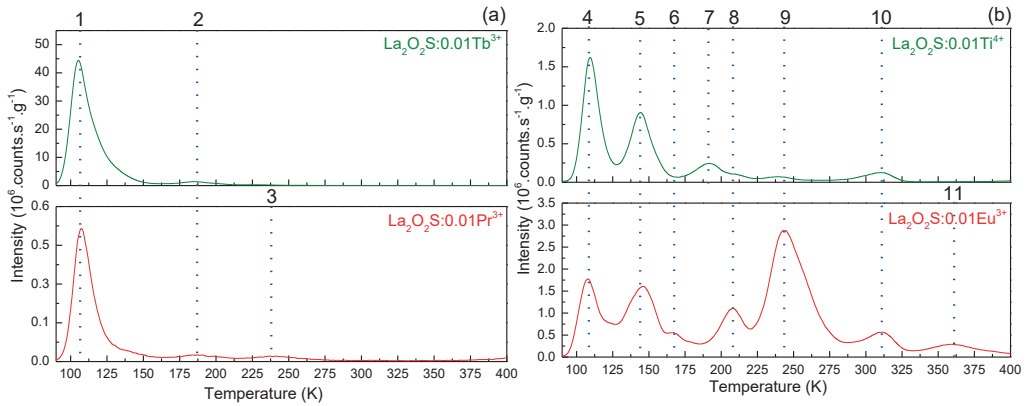Figure 6.6 Low-temperature thermoluminescence glow curves of (a) $La_2O_2S:0.01Tb^{3+}$ and $La_2O_2S:0.0Pr^{3+}$, (b) $La_2O_2S:0.01Ti^{4+}$ and $La_2O_2S:0.01Eu^{3+}$. The heating rate was 1 K/s for all TL-recordings. The peak intensities are normalized by the mass of the sample.

Figure 6.6a, 6.7a and 6.8a display the low-temperature TL for La_2O_2S, Gd_2O_2S and Lu_2O_2S with different dopants. As in Figure 6.5a, with Tb^{3+} and Pr^{3+} doping, TL

glow peaks at the same temperature are observed. With Ce^{3+} doping the same TL glow peak temperature as with Tb^{3+} and Pr^{3+} doping in Lu_2O_2S is observed in Figure 6.8a. For Ce^{3+} doping in $La_2O_2S:Ce^{3+}$ and $Gd_2O_2S:Ce^{3+}$ the Ce^{3+} emission totally quenched [26] and no TL glow peaks were measured.
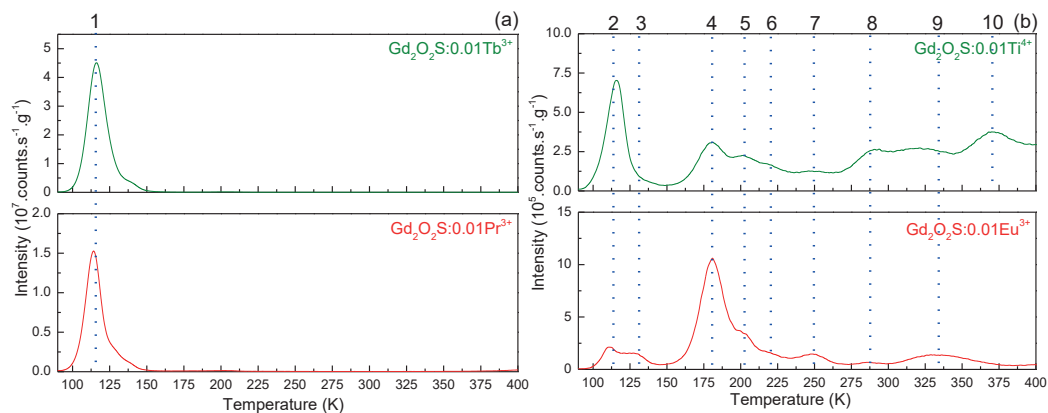
Figure 6.7. Low-temperature thermoluminescence glow curves of (a) $Gd_2O_2S:0.01Tb^{3+}$ and $Gd_2O_2S:0.0Pr^{3+}$, (b) $Gd_2O_2S:0.01Ti^{4+}$ and $Gd_2O_2S:0.01Eu^{3+}$. The heating rate was 1 K/s for all TL-recordings. The peak intensities are normalized by the mass of the sample.

Figure 6.8. Low-temperature thermoluminescence glow curves of (a) $Lu_2O_2S:0.01Tb^{3+}$, $Lu_2O_2S:0.0Pr^{3+}$ and $Lu_2O_2S:0.0Ce^{3+}$, (b) $Lu_2O_2S:0.01Ti^{4+}$ and $Lu_2O_2S:0.01Eu^{3+}$. The heating rate was 1 K/s for all TL-recordings. The peak intensities are normalized by the mass of the sample.

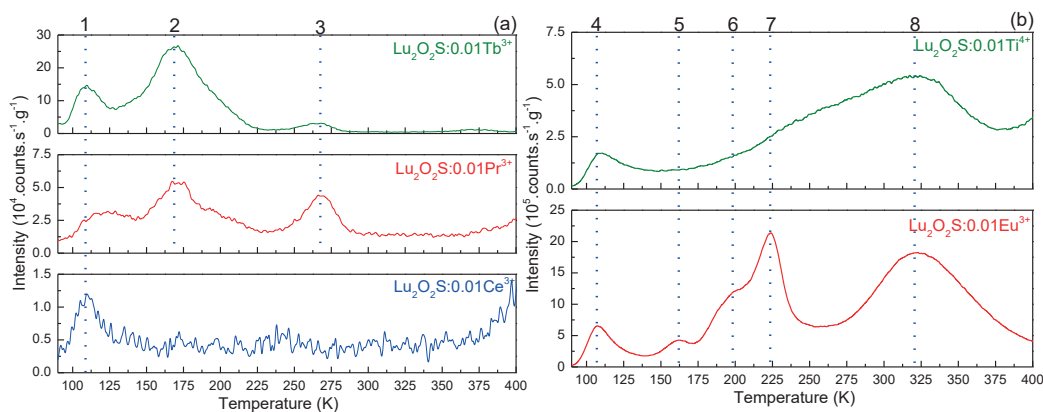Figure 6.6b illustrates the low temperature TL for Ti^{4+} and Eu^{3+} single doped La_2O_2S. We observe that between 90 to 400 K both samples share almost the same

TL glow peaks except for peaks 7 and 11. The same TL peak position implies that charge carriers are released from the same type of trapping centers not related to Eu or Ti. The absence of TL glow above 325 K in $La_2O_2S:Ti^{4+}$ is probably due to the almost complete thermal quenching of Ti^{4+} emission above room temperature (Figure S6.3).

Almost the same TL glow peak positions are observed for $Gd_2O_2S:Ti^{4+}$ and $Gd_2O_2S:Eu^{3+}$ shown in Figure 6.7b with peak numbers 2, 3, 4, 5, 6, 7, 8 and 9. An extra peak (peak 10) is observed at ~375 K for $Gd_2O_2S:Ti^{4+}$.

$Lu_2O_2S:Ti^{4+}$ in Figure 6.8b shows an extremely broad Ti^{4+} TL glow curve that begins at ~135 K and reaches maximum glow at ~320 K. It appears that Ti^{4+} doped RE_2O_2S shows broader TL glow peaks than when Eu^{3+} is the dopant. This may indicate a trap depth distribution[32] caused by the need for charge compensating defects.

Table 6.1 lists all thermoluminescence parameters. All the frequency factors s are from the R3 line of RE_2O_2S Raman spectroscopy[31], which is 1.1 x 10^{13} (365cm^{-1}) for La_2O_2S, 1.3 x 10^{13} (428 cm^{-1}) for Gd_2O_2S, 1.3 x 10^{13} (444 cm^{-1}) for Y_2O_2S and 1.4 x 10^{13} (472 cm^{-1}) for Lu_2O_2S and all the trap depths (E) were calculated by Eq.2.

Table 6.1. The peak number, frequency factor s (s^{-1}), peak maxima T_m (K) and trap depth E (eV) of the TL glow peaks recorded at $\beta = 1$ K/s from RE_2O_2S (RE=La, Gd, Y and Lu).

		1	2	3	4	5	6	7	8	9	10	11
	s						1.1 x 10^{13}					
La_2O_2S	T_m	105	185	240	110	145	165	190	208	245	312	360
	E	0.28	0.51	0.66	0.30	0.39	0.45	0.52	0.57	0.68	0.87	1.0
	s						1.3 x 10^{13}					
Gd_2O_2S	T_m	115	115	130	180	203	220	250	288	335	370	
	E	0.31	0.31	0.35	0.50	0.56	0.61	0.70	0.80	0.94	1.0	
	s						1.3 x 10^{13}					
Y_2O_2S	T_m	115	182	113	134	181	210	240	278	350		
	E	0.31	0.50	0.31	0.37	0.50	0.58	0.67	0.78	0.98		

	s				1.4×10^{13}				
	T_m	108	170	267	105	160	200	223	320
Lu_2O_2S	E	0.29	0.47	0.75	0.29	0.44	0.61	0.62	0.90

So far, we found that in Tb^{3+}, Pr^{3+} and Ce^{3+} single doped RE_2O_2S, the charge carriers are not released from Ce, Pr or Tb but from other trapping centers. The same applies for Ti^{4+} and Eu^{3+} single-doped RE_2O_2S. Here we conclude that for Tb^{3+}, Pr^{3+} and Ce^{3+} doped RE_2O_2S the TL glow curves are from host related electron traps while for Ti^{4+} and Eu^{3+} doped samples the TL bands are from host related hole trapping centers. The reasons will be discussed in detail in the Discussion part.

6.4.4 Thermoluminescence excitation spectra

Figure 6.9a shows the thermoluminescence excitation (TLE) spectra of Eu^{3+} single doped RE_2O_2S. A comparison with the Eu^{3+} excitation spectra (PLE) from Figure 6.2a can be seen in Figures S6.7-S6.10 in the Supporting Information. For each sample two broad bands centered near 260 and 330 nm can be observed that matches with the host exciton creation bands and Eu^{3+} CT-bands, respectively.
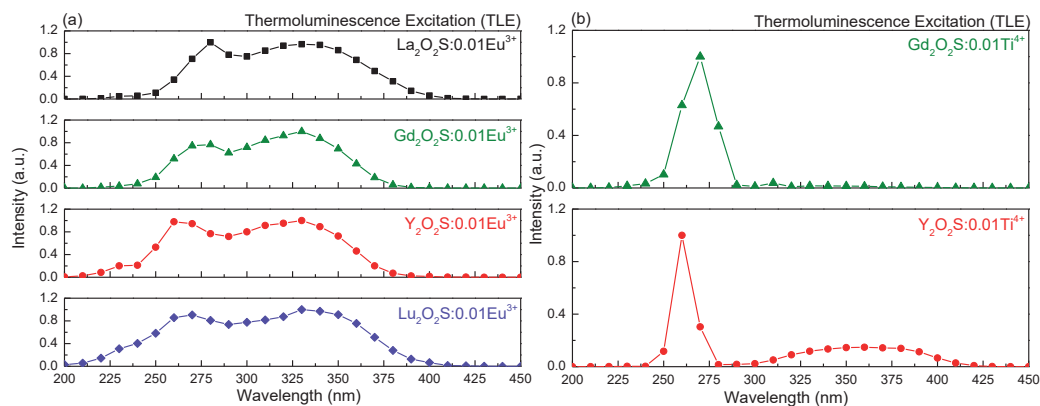

Figure 6.9. Thermoluminescence excitation (TLE) spectra of (a) $RE_2O_2S:0.01Eu^{3+}$, (b) $Gd_2O_2S:0.01Ti^{4+}$ and $Y_2O_2S:0.01Ti^{4+}$. The samples have been excited by an Xe lamp with wavelengths ranging from 200 to 450 nm during 600 s before TL glow curve recording. The slit width was set at 1 mm leading to a spectrum resolution of 8 nm. The thermoluminescence excitation spectra were obtained by plotting the integrated TL from 300 K to 600 K as function of the excitation wavelength. The heating rate for TL readout is 1 K/s and the wavelength step is 10 nm. The sample was excited at room temperature.

Figure 6.9b shows the TLE spectra of $Gd_2O_2S:Ti^{4+}$ and $Y_2O_2S:Ti^{4+}$. Comparison with the PLE spectra from Figure 6.3a can be seen in Figure S6.8 and S6.9. The TLE band between 260 to 280 nm is the host exciton creation band and the one between 300 to 400 nm is the Ti^{4+} CT-band, similar to the Ti^{4+} PLE spectra shown in Figure 6.3a. $Gd_2O_2S:Ti^{4+}$ shows a very weak TLE band near 350 nm with intensity much lower than in the PLE spectrum. However the band still exists indicating that this sample can be charged by 350 nm UV light. No TLE spectra could be recorded for $La_2O_2S:Ti^{4+}$ and $Lu_2O_2S:Ti^{4+}$ which is probably related to the very weak excitation efficiency of Ti^{4+} CT-luminescence in Figure 6.3.

6.5 Discussion

6.5.1 Vacuum Referred Binding Energy (VRBE) diagram of RE_2O_2S and Ti^{4+} charge transfer bands

To discuss the trapping and detrapping processes of electrons and holes in RE_2O_2S, we will first construct and exploit the VRBE diagram. The VRBE stands for vacuum referred binding energy that is defined as the energy needed to bring an electron from a level in the diagram to the vacuum outside the sample. The energy at rest in vacuum or vacuum level is then defined as energy zero. The reason to choose the VRBE diagram is because the binding energy of an electron in a lanthanide defect (both divalent and trivalent) states within the bandgap can be compared in different materials with respect to the same energy reference. Further details about how to construct the VRBE diagrams from spectroscopic data can be found in Ref.33-34.

Figure 6.10 shows the stacked VRBE diagrams of RE_2O_2S with location of Pr^{3+}, Tb^{3+}, Eu^{2+} and Ti^{3+} levels. The detailed VRBE diagrams with all lanthanide impurities level locations can be found in Figure S6.11. All the data needed and used to construct the VRBE diagrams are listed in Table 6.2. We adopted for all four samples a value of 6.37 eV for the so-called U-parameter of the chemical shift model. The reason for adopting the same U-parameter is due to the similar chemical environment surrounding Eu^{3+} in RE_2O_2S. This value defines within the chemical shift model a VRBE of -3.77 eV in the ground state of Eu^{2+} in the four RE_2O_2S samples. The Pr^{3+} and Tb^{3+} grounds states are then fixed at the same energy for all of the samples, with the values of -6.76 eV and -6.57 eV, respectively.
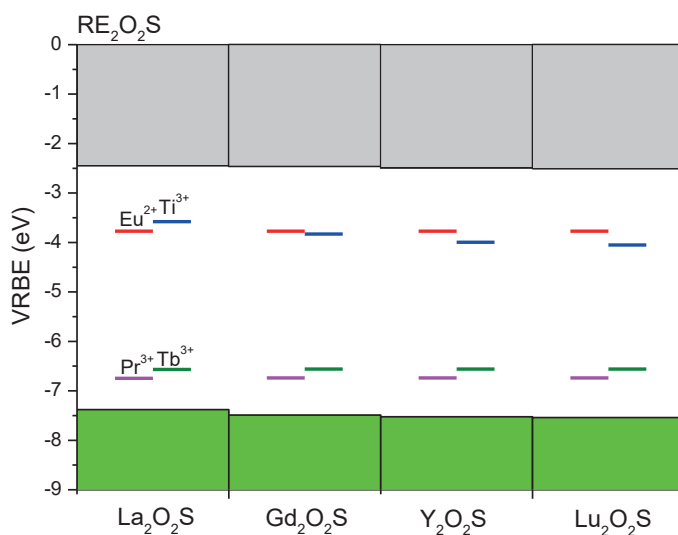
Figure 6.10 Stacked VRBE diagrams of RE_2O_2S (RE=La, Gd, Y and Lu) with the VRBE in the ground states of Pr^{3+}, Tb^{3+}, Eu^{2+}, and Ti^{3+}.

The top of the valence band is obtained from the VB $\rightarrow$ Eu^{3+} CT-energy in Figure 6.2a and Table 6.2. The increase of that CT energy with smaller RE implies that the valence band maximum moves downwards. The conduction band bottom is obtained from the exciton creation energy (Figure 6.2a) plus 8% of that to account for the electron-hole binding energy.

Table 6.2. The parameters used to construct the VRBE diagram for RE_2O_2S with U= 6.37 eV. All numbers are in eV.

Sample	E^{ex}	E^{CT} (Eu^{3+})	E^{CT} (Ti^{4+})	E_V	E_C	E_{Tb}^{3+}	E_{Pr}^{3+}
La_2O_2S	4.57	3.61	3.79	-7.38	-2.44	-6.57	-6.75
Gd_2O_2S	4.66	3.72	3.65	-7.49	-2.46	-6.57	-6.75
Y_2O_2S	4.67	3.75	3.53	-7.52	-2.48	-6.57	-6.75
Lu_2O_2S	4.66	3.77	3.44	-7.54	-2.51	-6.57	-6.75

The Ti^{4+} doped oxysulfides show very broad excitation (fwhm ~0.8 eV) and emission (whm ~0.5 eV) bands in Figure 6.3. The broad excitation band between 320 and 380 nm is due to the VB $\rightarrow$ Ti^{4+} charge transfer, which means that electrons in the anions are excited to Ti^{4+} forming Ti^{3+} in its lowest $3d_1$ state. Here we assume that the energy at the maximum of the CT-band corresponds with the

126

location of the $Ti^{3+/4+}$ level above the VB-top. Therefore, the VRBE in the ground states of Ti^{3+} can be obtained as shown in Figure 6.10.

Rogers et al, compiled the VRBE in the Ti^{3+} ground state levels derived from different Ti^{4+} doped materials. They found that the VRBE in the Ti^{3+} lowest $3d_1$ state (E_{3d1}) appears always near -4±1 eV and the compound to compound variation of VRBE is attributed to the crystal field splitting(CFS)[35]. Figure 6.10 shows that the Ti^{3+} $3d_1$ states are near -4 eV and decrease from La_2O_2S to Lu_2O_2S. It was empirically found that the size of the CFS for the 5d-levels of the lanthanides is inversely propositional to the square of the bond length[36]. Ti^{3+} has one electron in the d-orbital like the 5d excited states of the lanthanides that shows the same CFS tendency as the 5d-levels of lanthanides[35, 37]. Table S6.1 shows that the RE-(O,S) bond lengths decrease from La_2O_2S to Lu_2O_2S[38-41]. Therefore, the CFS of the Ti^{3+} 3d-levels is expected to increase from La_2O_2S to Lu_2O_2S. Such increased CFS will then reduce the VRBE in the lowest $3d_1$ state of Ti^{3+}. This forms then our explanation for the red-shift from 327 nm (3.79 eV) in La_2O_2S:Ti^{4+} to 360 nm (3.44 eV) in Lu_2O_2S:Ti^{4+} of the VB $\rightarrow$ Ti^{4+} charge transfer excitation and the red-shift of the Ti^{4+} CT-luminescence in Figure 6.3b.

6.5.2 Trapping and detrapping

The stacked VRBE diagrams of Figure 6.10 show that the divalent Eu ground state is about 1.3 eV below the CB in RE_2O_2S which implies that the corresponding trivalent Eu can act as an electron trapping center. The same applies to Ti which has Ti^{3+} ground state location about 1.2 to 1.5 eV below the CB as illustrated in Figure 6.10 which means that Ti^{4+} also acts as the electron trapping center.

During γ-ray irradiation in the TLEM spectra and β-ray irradiation in the low temperature TL spectra, the free charge carriers are generated that can move freely through the CB and the VB. For the Eu^{3+} or Ti^{4+} single doped RE_2O_2S, the electrons will be trapped in either Eu^{3+} or Ti^{4+} forming Eu^{2+} or Ti^{3+}, and the holes must be trapped somewhere else. In Figure 6.5b-6.8b, some common TL glow peaks at the same temperature can be observed. The temperatures at the maxima of glow peaks 3, 4, 5, 6, 7, and 9 listed in Table 6.1 are about the same but with different relative intensities in Y_2O_2S:Eu^{3+}/Ti^{4+}. La_2O_2S:Eu^{3+}/Ti^{4+}, Gd_2O_2S:Eu^{3+}/Ti^{4+} and Lu_2O_2S:Eu^{3+}/Ti^{4+} also show the common TL glow peaks at the same temperature. These suggest that the Eu^{3+} or Ti^{4+} single doped samples have the same type of hole trapping centers.

The thermoluminescence excitation (TLE) spectra for each Eu^{3+} doped sample in Figure 6.9a shows a broad band that coincides with the VB → Eu^{3+} CT excitation in Figure 6.2a. During CT-band excitation electrons are excited from the valence band to the Eu^{2+} $^8S_{7/2}$ ground state leaving a hole in the valence band. It was demonstrated by Struck et al that during the Eu^{3+} CT excitation a hole can dissociate from the CT-state [42]. Also p-type photoconductivity was observed by Dobrov et al in La_2O_2S:Eu^{3+} during VB → Eu^{3+} CT excitation [43]. So, during CT-band excitation part of the holes are released and trapped in the hole trapping centers. Then during the TL readout, the captured holes release again to recombine with Eu^{2+} producing Eu^{3+} characteristic emission as shown in Figure 6.4 and Figure S6.4. The same conclusion was also suggested by Forest et al[25] and Fonger et al[44-45] by studying the thermoluminescence after CT excitation in La_2O_2S:Eu^{3+} and Y_2O_2S:Eu^{3+}.

The TLE spectra for Ti^{4+} doped Y_2O_2S and Gd_2O_2S in Figure 6.9b again shows a broad band that coincides with the VB → Ti^{4+} CT-bands in Figure 6.3a. During the CT-band excitation, Ti^{3+} is formed and holes are released to the VB to be captured by the hole trapping center. Similar as for Eu doping, during the TL readout, the captured holes are released again and recombine at Ti^{3+} producing Ti^{4+} CT-luminescence as shown in Figure 6.4 and Figure S6.4.

Figure 6.5a and Table 6.1 show that the Ce^{3+}, Pr^{3+} and Tb^{3+} single doped Y_2O_2S all have the same glow peaks. From the stacked VRBE diagrams in Figure 6.10 and Figure S6.11 we observe that the trivalent Ce, Pr and Tb ground states are 2.6 eV, 0.77 eV, and 0.95 eV above the VB and these trivalent ions can act as hole trapping center during β irradiation. Then the electrons must be captured by the host lattice itself. Now the question turns to whether the captured electrons release earlier or the trapped holes release earlier.

If the holes from Ce^{4+}, Pr^{4+} or Tb^{4+} release earlier than electrons, one can estimate according to Eq. 2 with a heating rate of 1 K/s that the TL peak positions (T_m) due to hole release from Ce^{4+}, Pr^{4+} and Tb^{4+} to the VB in Y_2O_2S are expected at ~900 K, 276 K and 339 K, respectively. This means that the TL peak temperature for Y_2O_2S:Ce^{3+}, Y_2O_2S:Pr^{3+} and Y_2O_2S:Tb^{3+} should be different and much higher than the observed TL temperature shown in Figure 6.5a. Similarly, one observes that with Pr^{3+} and Tb^{3+} doping in La_2O_2S, Gd_2O_2S and Lu_2O_2S, the TL glow peaks for each sample are at the same temperature shown in Figure 6.6a, 6.7a and 6.8a,

respectively. Therefore, in Ce^{3+}, Pr^{3+} and Tb^{3+} single doped RE_2O_2S, the TL glow curves originate from electrons released from host lattice related trapping centers and recombine at the Ce^{4+}, Pr^{4+} or Tb^{4+} hole trapping center providing Ce^{3+}, Pr^{3+} and Tb^{3+} emission.

6.5.3 The afterglow mechanism of $Y_2O_2S:Ti^{4+}$, Eu^{3+}

Based on the above discussion, the afterglow mechanism of $Y_2O_2S:Ti^{4+}$,Eu^{3+} can be proposed as illustrated in Figure 6.11. Upon UV excitation by day light, electrons are excited from the VB to Ti^{4+} and Eu^{3+} forming Ti^{3+} and Eu^{2+} in the ground states (arrows 1). The holes released to the VB are captured by the hole trapping centers (arrow 2) although it is still not clear what are those hole trapping centers. Then, the hole trapping center with a shallow trap depth enables spontaneously release of holes at the room temperature (arrow 3). It travels as a free hole *via* the VB or as a self-trapped hole or V_k center to recombine with Ti^{3+} and Eu^{2+} producing Ti^{4+} CT emission and Eu^{3+} 4f-4f emission (arrows 4). We conclude that the afterglow of $Y_2O_2S:Ti^{4+}$,Eu^{3+} is due to the hole release instead of the more common electron release. However, further research needs to be performed to identify the nature of the hole trapping centers.
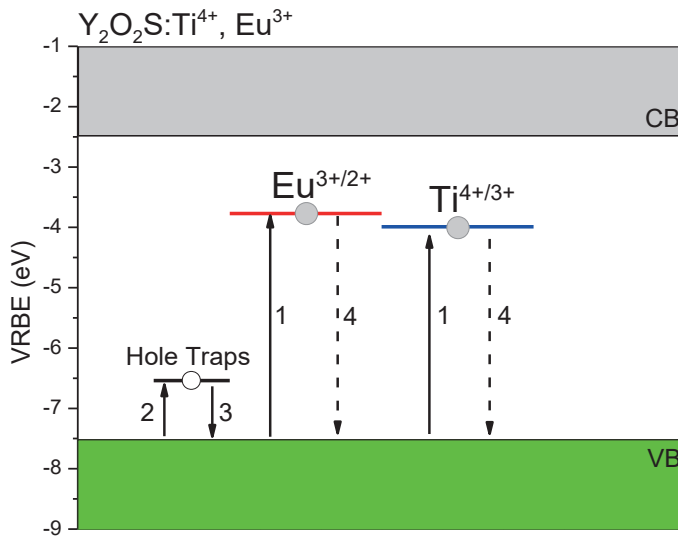

Figure 6.11. The proposed afterglow mechanism for $Y_2O_2S:Ti^{4+}$,Eu^{3+}. The filled circle stands for electrons and the open circle stands for hole.

6.6 Conclusion

Photoluminescence spectroscopy, thermoluminescence and the chemical shift model have been combined to study the trapping and detrapping processes of the charge carriers in RE_2O_2S. Photoluminescence spectroscopy shows that Ti^{4+} CT-luminescence provides the orange-red emission in $RE_2O_2S:Ti^{4+}$. The red-shift of the Ti^{4+} CT-excitation and emission from $La_2O_2S:Ti^{4+}$ to $Lu_2O_2S:Ti^{4+}$ is attributed to the increased crystal field splitting of the Ti^{3+} 3d levels with smaller size of the site occupied. The TLEM spectra confirm that Ti^{4+} and Eu^{3+} act as the recombination center. The low temperature TL measurements reveal that for Tb^{3+}, Pr^{3+} and Ce^{3+} doped RE_2O_2S the TL glow curves are from host related electron traps while for Ti^{4+} and Eu^{3+} doped RE_2O_2S the TL bands are from the host related hole trapping centers. The TL excitation spectra show that the electrons captured by Ti^{4+} and Eu^{3+} originate from the VB. Finally, the afterglow mechanism of $Y_2O_2S:Ti^{4+},Eu^{3+}$ were derived that is due to the hole release instead of the more common electron release based on the above information.

6.7 Acknowledgements

6.8 Reference

1. Li, Y.; Gecevicius, M.; Qiu, J., Long Persistent Phosphors-from Fundamentals to Applications. *Chemical Society Reviews* **2016**, 45, 2090-2136.

2. Van den Eeckhout, K.; Smet, P. F.; Poelman, D., Persistent Luminescence in Eu2+ Doped Compounds a Review. *Materials* **2010**, *3*, 2536-2566.

3. Van den Eeckhout, K.; Poelman, D.; Smet, P., Persistent Luminescence in Non-Eu2+-Doped Compounds: A Review. *Materials* **2013**, *6*, 2789-2818.

4. Leblans, P.; Vandenbroucke, D.; Willems, P., Storage Phosphors for Medical Imaging. *Materials* **2011**, *4*, 1034-1086.

5. McClure, D. S.; Kiss, Z., Survey of the Spectra of the Divalent Rare-Earth Ions in Cubic Crystals. *The Journal of Chemical Physics* **1963**, *39*, 3251-3257.

6. Dorenbos, P., Valence Stability of Lanthanide Ions in Inorganic Compounds. *Chemistry of Materials* **2005**, *17*, 6452-6456.

7. Bos, A. J. J.; Dorenbos, P.; Bessière, A.; Lecointre, A.; Bedu, M.; Bettinelli, M.; Piccinelli, F., Study of Tl Glow Curves of YPO4 Double Doped with Lanthanide Ions. *Radiation Measurements* **2011**, *46*, 1410-1416.

8. Luo, H.; Bos, A. J. J.; Dobrowolska, A.; Dorenbos, P., Low-Temperature Vuv Photoluminescence and Thermoluminescence of UV Excited Afterglow Phosphor Sr3AlxSi1-xO5:Ce3+,Ln3+ (Ln = Er, Nd, Sm, Dy and Tm). *Physical Chemistry Chemical Physics* **2015**, *17*, 15419-15427.

9. You, F.; Bos, A. J. J.; Shi, Q.; Huang, S.; Dorenbos, P., Thermoluminescence Investigation of Donor Ce3+, Pr3+, Tb3+ Acceptor Eu3+, Yb3+ Pairs in Y3Al5O12. *Physical Review B* **2012**, *85*, 115101.

10. Luo, H.; Bos, A. J. J.; Dorenbos, P., Controlled Electron–Hole Trapping and Detrapping Process in GdAlO3 by Valence Band Engineering. *The Journal of Physical Chemistry C* **2016**, *120*, 5916-5925.

11. Chakrabarti, K.; Mathur, V. K.; Thomas, L. A.; Abbundi, R. J., Charge Trapping and Mechanism of Stimulated Luminescence in CaS:Ce,Sm. *Journal of Applied Physics* **1989**, *65*, 2021-2023.

12. Matsuzawa, T., A New Long Phosphorescent Phosphor with High Brightness, SrAl2O4:Eu2 +, Dy3 + *journal of Electrochem Society* **1996**, *143*, 2670.

13. Hajime Yamamoto; Matsuzawab, T., Mechanism of Long Phosphorescence of SrAl2O4:Eu2+, Dy3+ and CaAl2O4:Eu2+, Nd3+. *Journal of Luminescence* **1997**, *72*, 287-289.

14. Rodríguez Burbano, D. C.; Sharma, S. K.; Dorenbos, P.; Viana, B.; Capobianco, J. A., Persistent and Photostimulated Red Emission in CaS:Eu2+,Dy3+ Nanophosphors. *Advanced Optical Materials* **2015**, 551-557.

15. Miyamoto, Y.; Kato, H.; Honna, Y.; Yamamoto, H.; Ohmi, K., An Orange-Emitting, Long-Persistent Phosphor, Ca2Si5N8:Eu2+,Tm3+. *Journal of the Electrochemical Society* **2009**, *156*, J235.

16. Ueda, J.; Dorenbos, P.; Bos, A.; Kuroishi, K.; Tanabe, S., Control of Electron Transfer between Ce3+ and Cr3+ in Y3Al5-xGaxO12 Host by Conduction Band Engineering. *Journal of Materials Chemistry C* **2015**, *3(22)*, 5642-5651.

17. Kang, C.-C.; Liu, R.-S.; Chang, J.-C.; Lee, B.-J., Synthesis and Luminescent Properties of a New Yellowish-Orange Afterglow Phosphor Y2O2S:Ti,Mg. *Chemistry of Materials* **2003**, *15*, 3966-3968.

18. Zhou, X.; Xing, M.; Jiang, T.; Fu, Y.; Peng, Y.; Wang, H.; Luo, X., Afterglow Performance Enhancement and Mechanism Studies on Y2O2S:Eu,Mg,Ti Prepared Via Cold Isostatic Pressing. *Journal of Alloys and Compounds* **2014**, *585*, 376-383.

19. Hang, T.; Liu, Q.; Mao, D.; Chang, C., Long Lasting Behavior of Gd2O2S:Eu3+ Phosphor Synthesized by Hydrothermal Routine. *Materials Chemistry and Physics* **2008**, *107*, 142-147.

20. Hölsä, J.; Laamanen, T.; Lastusaari, M.; Malkamäki, M.; Niittykoski, J.; Zych, E., Effect of Mg2+ and Tiiv Doping on the Luminescence of Y2O2S:Eu3+. *Optical Materials* **2009**, *31*, 1791-1793.

21. Lei, B.; Liu, Y.; Zhang, J.; Meng, J.; Man, S.; Tan, S., Persistent Luminescence in Rare Earth Ion-Doped Gadolinium Oxysulfide Phosphors. *Journal of Alloys and Compounds* **2010**, *495*, 247-253.

22. Dorenbos, P., Mechanism of Persistent Luminescence in Eu2+ and Dy3+ Codoped Aluminate and Silicate Compounds. *Journal of the Electrochemical Society* **2005**, *152*, H107-H110.

23. Dobrowolska, A.; Bos, A. J. J.; Dorenbos, P., Electron Tunnelling Phenomena in YPO4:Ce,Ln (Ln = Er, Ho, Nd, Dy). *Journal of Physics D: Applied Physics* **2014**, *47*, 335301-335311..

24. Bos, A. J. J.; van Duijvenvoorde, R. M.; van der Kolk, E.; Drozdowski, W.; Dorenbos, P., Thermoluminescence Excitation Spectroscopy: A Versatile Technique to Study Persistent Luminescence Phosphors. *Journal of Luminescence* **2011**, *131*, 1465-1471.

25. Forest, H.; Cocco, A.; Hersh, H., Energy Storage in La2O2S: Eu3+ with Direct 4f6 Eu3+ Excitation. *Journal of Luminescence* **1970**, *3*, 25-36.

26. Yokono, S.; Abe, T.; Hoshina, T., Red Luminescence of Ce3+ Due to the Large Stokes Shifts in Y2O2S and Lu2O2S. *Journal of Luminescence* **1981**, *24*, 309-312.

27. Dorenbos, P., The Charge Transfer Energy and the Relation with the Band Gap of Compounds. *Journal of Luminescence* **2005**, *111*, 89-104.

28. Dorenbos, P., Systematic Behaviour in Trivalent Lanthanide Charge Transfer Energies. *Journal of Physics: Condensed Matter* **2003**, *15*, 8417-8434.

29. Ueda, J.; Meijerink, A.; Dorenbos, P.; Bos, A. J. J.; Tanabe, S., Thermal Ionization and Thermally Activated Crossover Quenching Processes for 5d-4f Luminescence in Y3Al5-xGaxO12: Pr3+. *Physical Review B* **2017**, *95*, 014303.

30. Azorín, J., Determination of Thermoluminescence Parameters from Glow Curves—I. A Review. *International Journal of Radiation Applications and Instrumentation. Part D. Nuclear Tracks and Radiation Measurements* **1986**, *11*, 159-166.

31. Yokono, S.; Imanaga, S.; Hoshina, T., Raman Spectra for Eu Doped Ln2O2S Phosphors. *Journal of the Physical Society of Japan* **1979**, *46*, 1882-1888.

32. Van den Eeckhout, K.; Bos, A.; Poelman, D.; Smet, P., Revealing Trap Depth Distributions in Persistent Phosphors. *Physical Review B* **2013**, *87* (4), 045126.

33. Dorenbos, P., Modeling the Chemical Shift of Lanthanide 4f Electron Binding Energies. *Physical Review B* **2012**, *85* (16), *165107*.

34. P.Dorenbos, A Review on How Lanthanide Impurity Levels Change with Chemistry and Structure of Inorganic Compounds. *ECS Journal of Solid State Science and Technology* **2013**, 2, R3001-R3011.

35. Rogers, E. G.; Dorenbos, P., Vacuum Energy Referred Ti3+/4+ Donor/Acceptor States in Insulating and Semiconducting Inorganic Compounds. *Journal of Luminescence* **2014**, *153*, 40-45.

36. Dorenbos, P., 5d-Level Energies of Ce3+ and the Crystalline Environment. Iii. Oxides Containing Ionic Complexes. *Physical Review B* **2001**, *64* (12), 125117.

37. Avram, N. M.; Brik, M. G., *Optical Properties of 3d-Ions in Crystals: Spectroscopy and Crystal Field Analysis*; Springer Berlin Heidelberg, 2013.

38. Machado, L. C.; de Azeredo, M. T. D. O.; Corrêa, H. P. S.; do Rosário Matos, J.; Mazali, Í. O., Formation of Oxysulfide LnO2S2 and Oxysulfate LnO2SO4 Phases in the Thermal Decomposition Process of Lanthanide Sulfonates (Ln = la, Sm). *Journal of Thermal Analysis and Calorimetry* **2012**, *107*, 305-311.

39. Lian, J.; Sun, X.; Li, J.-G.; Xiao, B.; Duan, K., Characterization and Optical Properties of (Gd1-x, Prx)2O2S Nano-Phosphors Synthesized Using a Novel Co-Precipitation Method. *Materials Chemistry and Physics* **2010**, *122*, 354-361.

40. Ronda, C. R.; Mulder, H.; Klaassen, D. B. M., Solid Solubility of the Oxisulfides of Y, La, and Gd. *Journal of Solid State Chemistry* **1989**, *80*, 299-302.

41. Leskelä, M.; Niinistö, L., Solid Solutions in the Rare-Earth Oxysulfide Series. *Journal of Solid State Chemistry* **1976**, *19*, 245-250.

42. Struck, C. W.; Fonger, W. H., Dissociation of Eu3+ Charge-Transfer State Iny2O2S and La2O2S into Eu2+ and a Free Hole. *Physical Review B* **1971**, *4*, 22-34.

43. Dobrov, W. I.; Buchanan, R. A., Photoconductivity and Luminescence in Lanthanum Oxysulfide. *Applied Physics Letters* **1972**, *21*, 201-203.

44. Struck, C. W.; Fonger, W. H., Role of the Charge-Transfer States in Feeding and Thermally Emptying the 5d States of Eu3+ in Yttrium and Lanthanum Oxysulfides. *Journal of Luminescence* **1970**, *1*, 456-469.

45. Fonger, W. H.; Struck, C. W., Energy Loss and Energy Storage from the Eu3+ Charge-Transfer States in Y and La Oxysulfides. *Journal of the Electrochemical Society* **1971**, *118*, 273-280.
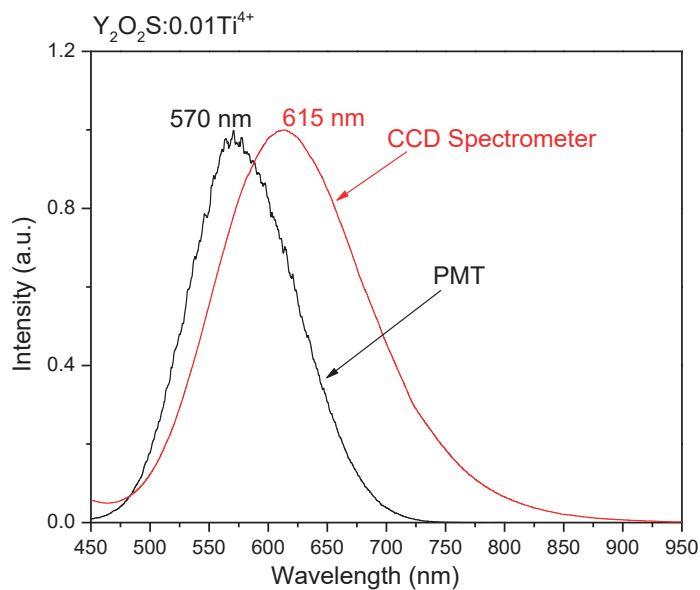
6.9 Supporting information

Figure S6.1. The comparison of the $Y_2O_2S:0.01Ti^{4+}$ emission spectra measured by the PMT (EMI 9635QA) and CCD (QE65000). Both curves were excited by 365 nm UV radiation and recorded at room temperature (RT).
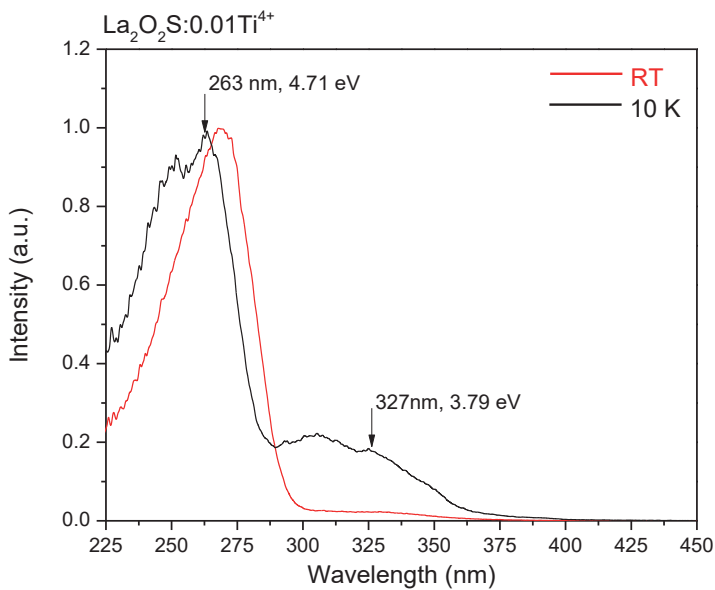
Figure S6.2. Comparison of the $La_2O_2S:0.01Ti^{4+}$ excitation spectra measured at 10 K and RT.
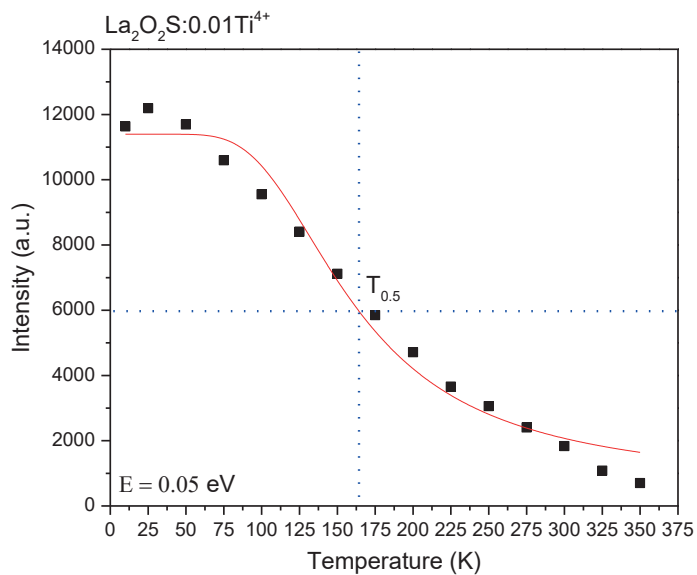

La$_2$O$_2$S:0.01Ti^{4+}

$T_{0.5}$

$E = 0.05$ eV

Figure S6.3. Thermal-quenching curve of $La_2O_2S:0.01Ti^{4+}$. The Black squares are measured and the red curve is fitted with Eq. 1.

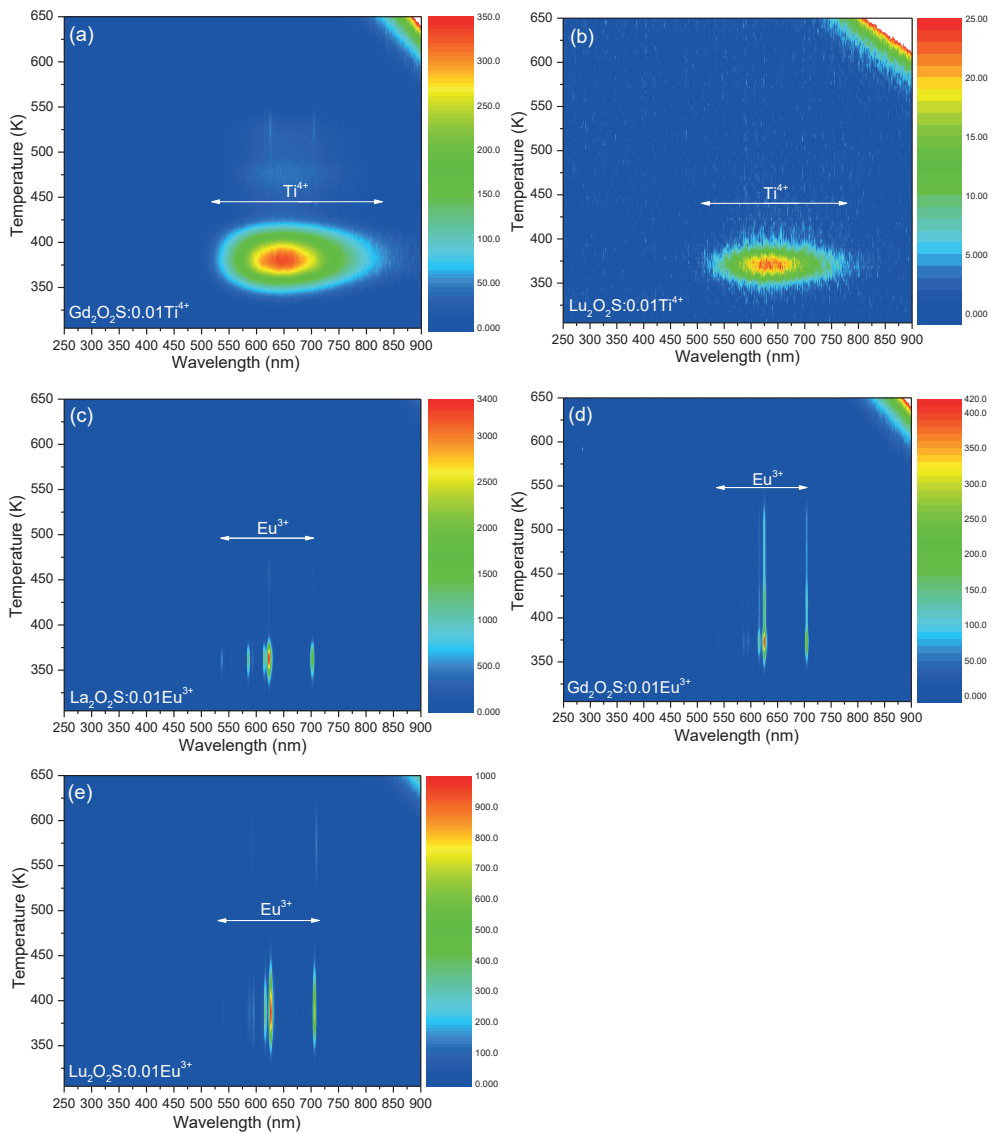Figure S6.4. Thermoluminescence emission spectra of (a) $Gd_2O_2S:0.01Ti^{4+}$, (b) $Lu_2O_2S:Ti^{4+}$, (c) $La_2O_2S:0.01Eu^{3+}$, (d) $Gd_2O_2S:0.01Eu^{3+}$ and (e) $Lu_2O_2S:0.01Eu^{3+}$. The heating rate for all of these samples is 1 K/s after exposure to gamma rays from a ^{60}Co source up to 1.6 kGy.

Figure S6.5. Thermal-quenching curve of $Y_2O_2S:0.01Ce^{3+}$. The sample was excited by 470 nm irradiation from the XE lamp with a monochromator. The Black squares are measured and the red curve is fitted with Eq. 1.
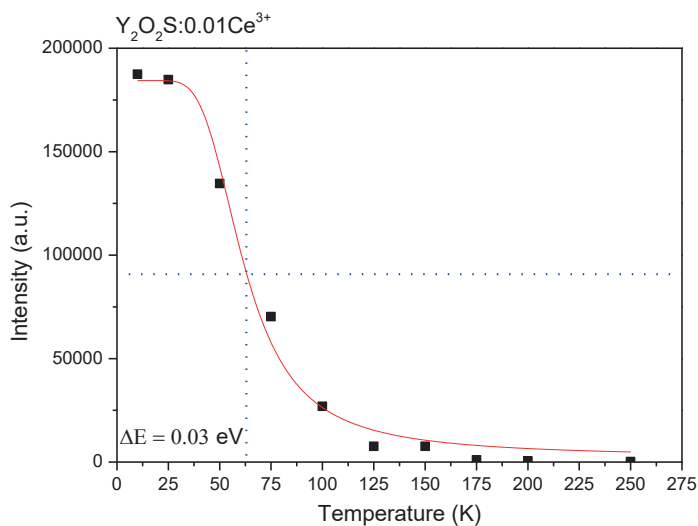

Figure S6.6. Thermal-quenching curve of $Lu_2O_2S:0.01Ce^{3+}$. The sample was excited by 470 nm irradiation from the XE lamp with a monochromator. The Black squares are measured and the red curve is fitted with Eq. 1.
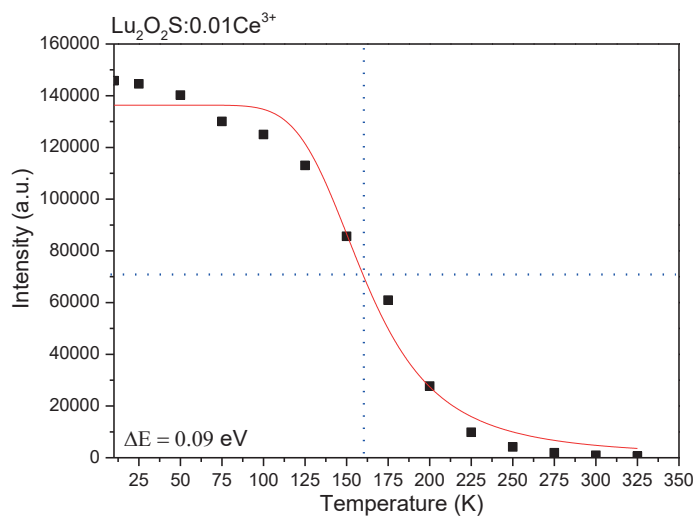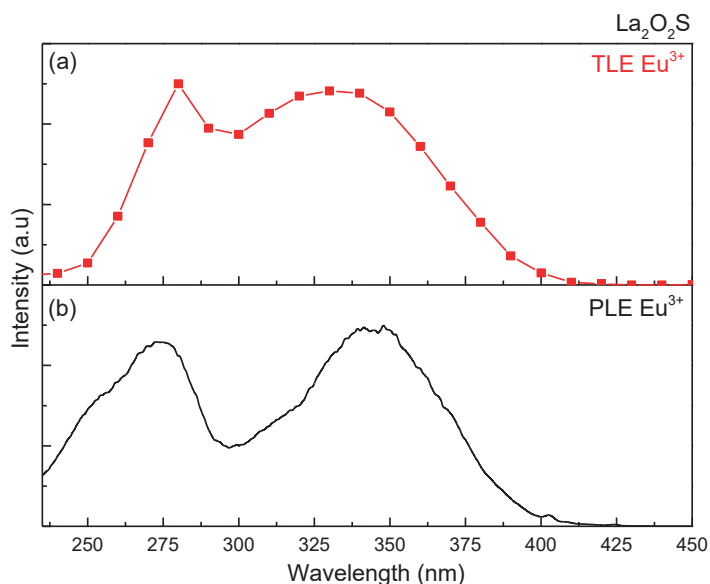
Figure S6.7. Comparison of (a) thermoluminescence excitation (TLE) spectra of La$_2$O$_2$S:0.01Eu^{3+} and (b) photoluminescence excitation (PLE) spectrum of La$_2$O$_2$S:0.01Eu^{3+} recorded at 625 nm emission. The sample has been excited by a Xe lamp at different wavelengths ranging from 225 to 450 nm during 600 s before glow cure recording. The thermoluminescence excitation spectra were obtained by plotting the integrated TL from 300 to 600 K as function of the excitation wavelength. The heating rate for TL readout is 1 K/s and the wavelength step is 10 nm. The sample was excited at room temperature.

Figure S6.8. Comparison of (a) thermoluminescence excitation (TLE) spectra of $Gd_2O_2S{:}0.01Eu^{3+}$, (b) photoluminescence excitation (PLE) spectrum of $Gd_2O_2S{:}0.01Eu^{3+}$ recorded at 625 nm emission, (c) thermoluminescence excitation (TLE) spectra of $Gd_2O_2S{:}0.01Ti^{4+}$ and (d) photoluminescence excitation (PLE) spectrum of $Gd_2O_2S{:}0.01Ti^{4+}$ recorded at 605 nm emission. The samples have been excited by a Xe lamp at different wavelengths ranging 225 nm to 450 nm during 600 s before glow curve recording. The thermoluminescence excitation spectra were obtained by plotting the integrated TL from 300 to 600 K as function of the excitation wavelength. The heating rate for TL readout is 1 K/s and the wavelength step is 10 nm. The sample was excited at room temperature.
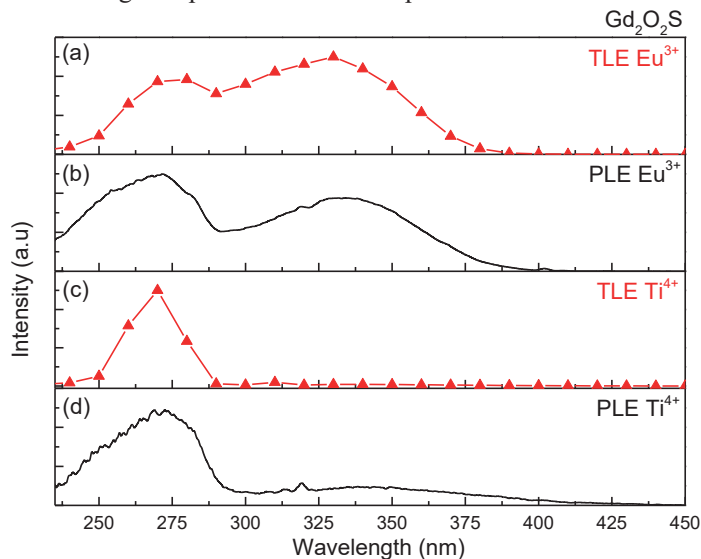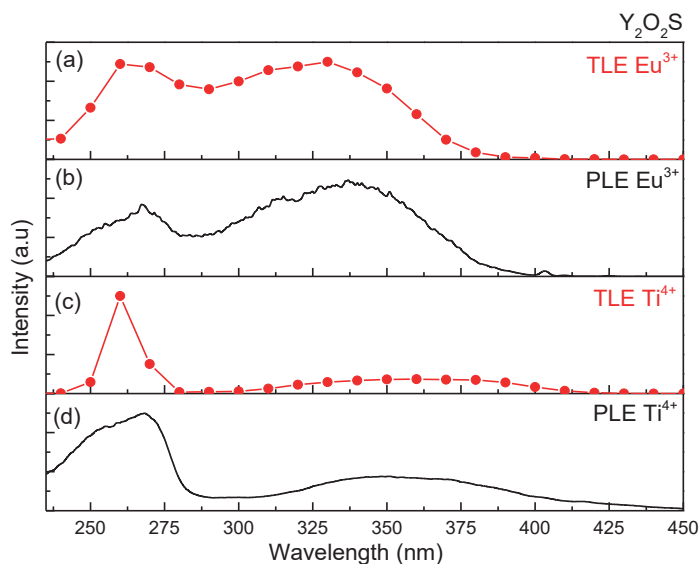

Figure S6.9. Comparison of (a) thermoluminescence excitation (TLE) spectra of $Y_2O_2S{:}0.01Eu^{3+}$, (b) photoluminescence excitation (PLE) spectrum of $Y_2O_2S{:}0.01Eu^{3+}$ recorded at 625 nm emission, (c) thermoluminescence excitation (TLE) spectra of $Y_2O_2S{:}0.01Ti^{4+}$ and (d) photoluminescence excitation (PLE) spectrum of $Y_2O_2S{:}0.01Ti^{4+}$ recorded at 615 nm emission. The samples have been excited by a Xe lamp at different wavelengths ranging 225 to 450 nm during 600 s before glow curve recording. The thermoluminescence excitation spectra were obtained by plotting the integrated TL from 300 to 600 K as function of the excitation wavelength. The heating rate for TL readout is 1 K/s and the wavelength step is 10 nm. The sample was excited at room temperature.
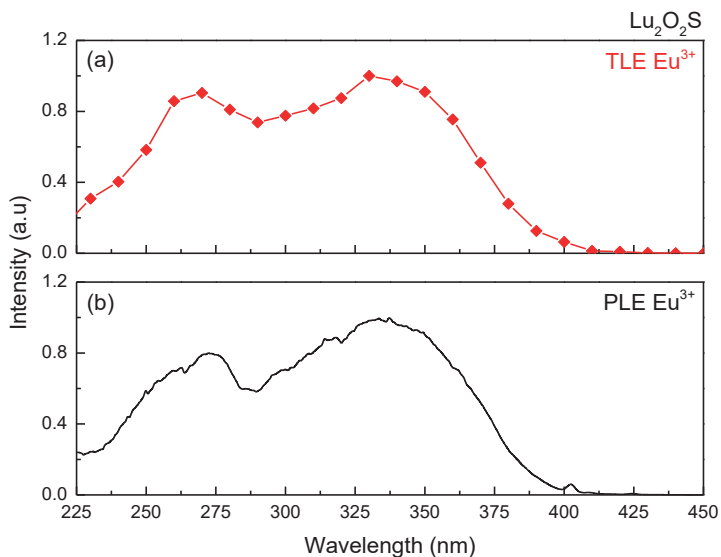
Figure S6.10. Comparison of (a) thermoluminescence excitation (TLE) spectra of $Lu_2O_2S{:}0.01Eu^{3+}$ and (b) thermoluminescence excitation (TLE) spectra of $Lu_2O_2S{:}0.01Eu^{3+}$ recorded at 625 nm. The sample has been excited by a Xe lamp at different wavelengths ranging from 225 to 450 nm during 600 s before glow curve recording. The thermoluminescence excitation spectra were obtained by plotting the integrated TL from 300 K to 600 K as function of the excitation wavelength. The heating rate for TL readout is 1 K/s and the wavelength step is 10 nm. The sample was excited at room temperature.
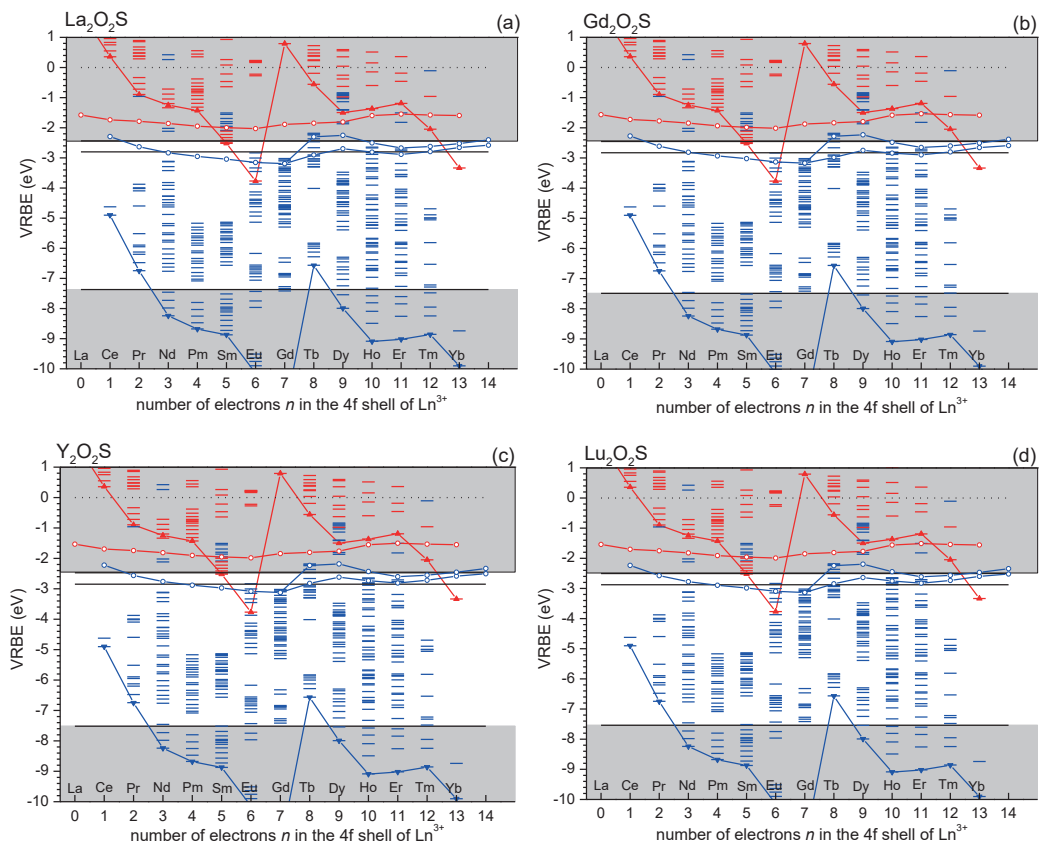
Figure S6.11. The energy level diagrams of (a) La$_2$O$_2$S, (b) Gd$_2$O$_2$S, (c) Y$_2$O$_2$S and (d) Lu$_2$O$_2$S.

Table S6.1. The lattice parameters for La_2O_2S, Gd_2O_2S, Y_2O_2S and Lu_2O_2S host lattice.

Sample	Volume (nm^3)	Bond Type	Bond Length (nm)
La_2O_2S	0.0987	La-O	0.2414 x 3, 0.2461
		La-S	0.3041 x 3
Gd_2O_2S	0.0857	Gd-O	0.2350 x 3, 0.2153
		Gd -S	0.2910 x 3
Y_2O_2S	0.0813	Y-O	0.2265 x 3, 0.2313
		Y -S	0.2846 x 3
Lu_2O_2S	0.0772	Lu-O	0.2222 x 3, 0.2285
		Lu -S	0.2799 x 3

7

Summary

In this thesis, two different charge carrier trapping and detrapping processes are investigated: (1) electron trapping and electron release; (2) hole trapping and hole release. Both of these two processes can be used to "deliberate design" afterglow phosphors or storage materials.

The "electron trapping and electron release" model is discussed in Chapter 3, Chapter 4 and the first part of Chapter 5 in detail. In these chapters, Ce^{3+} is the recombination center while the other lanthanide codopants (such as: Pr^{3+}, Er^{3+}, Nd^{3+}, Ho^{3+}, Dy^{3+}, and Tm^{3+}) act as electron trapping centers and for each lanthanide codopant there is a different trap depth.

In this model, the position of the CB bottom is crucial for afterglow properties. For example, in $Sr_3Al_xSi_{1-x}O_5:Ce^{3+},Dy^{3+}$ (Chapter 3), the CB bottom is too far above the Ce^{3+} $5d_1$ excited state that the thermal ionization of Ce^{3+} $5d_1$ excited state electron cannot take place at room temperature. Therefore only the electrons in higher 5d excited states of Ce^{3+} can be ionized into the CB and fill the traps, resulting that the material can only be charged by UV light at room temperature. On the other hand, $(Sr, Ca)_3(Y, Lu)_2Ge_3O_{12}:Ce^{3+}$ (Chapter 4) has a too low-lying CB resulting that most of the divalent lanthanides lowest $4f^n$ levels are in the CB. Only Sm^{3+} as codopant provides a TL glow, while other lanthanides codopants either cannot trap an electron or trap the electron too deep so that the recombination luminescence on Ce^{3+} will be quenched.

The "hole trapping and hole release" model is discussed in detail in Chapter 5 and Chapter 6, which is the first time that the model has been investigated and confirmed.

Chapter 5 reveals that: (1) Ce^{3+}, Pr^{3+} and Tb^{3+} can act as hole trapping centers while Sm^{3+}, Eu^{3+} and Yb^{3+} act as recombination centers in $GdAlO_3$: Ln^{3+},RE^{3+} (Ln=Sm, Eu and Yb, RE= Ce, Pr and Tb); (2) during the TL readout, the holes release earlier than the electrons providing Sm^{3+}, Eu^{3+} and Yb^{3+} 4f-4f characteristic emission; (3) Tb^{4+} and Pr^{4+} related hole trap depth can be adjusted by VB engineering; (4) the hole traps in $LaAlO_3:Eu^{3+},Tb^{3+}$ can be charged by Eu^{3+} charge transfer excitation energy.

The findings of Chapter 5 provided us with a new idea to develop an afterglow phosphor based on the hole trapping and hole release model instead of the more common electron trapping and electron release model. The similarity of Eu^{3+} TLE and PLE spectra of $LaAlO_3$:Eu^{3+},Tb^{3+} proves that we deal with a hole type of transport. This inspired us that Eu^{3+} can be used as a hole recombination center to generate efficient red emission. In order to absorb daylight the TLE should be shifted to wavelengths longer than 300-350 nm, and then the Eu^{3+} charge transfer excitation should be at relatively low energy, indicating that the material should have a high-lying VB.

In Chapter 6, we confirmed the above idea by studying the afterglow mechanism of Y_2O_2S:Eu^{3+},Ti^{4+}. The VRBE diagram reveals that Y_2O_2S has a relative high-lying VB with the VRBE of VB top at around -7.5 eV that explains the relatively low CT excitation energy for Eu^{3+} and Ti^{4+}. The TL measurements show that the Ti^{4+} and Eu^{3+} act as electron trapping centers and hole recombination centers and while host intrinsic defects act as hole trapping centers. The TLE spectra for each Eu^{3+} or Ti^{4+} single doped RE_2O_2S reveal a broad band that coincides with the VB to Eu^{3+} or Ti^{4+} charge transfer excitation, which explains that this material can be charged by sunlight. Based on the above information, we derived that the afterglow mechanism of Y_2O_2S:Eu^{3+},Ti^{4+} is also due to the hole release instead of the more common electron release.

Samenvating

In dit proefschrift worden twee verschillende ladingsinvangst- en ladingsvrijkomstprocessen onderzocht: (1) elektroneninvangst- en elektronenvrijkomstprocessen; (2) gateninvangst- en gatenvrijkomstprocessen. Beide processen kunnen worden gebruikt voor "bewust ontwerp" van nagloeifosforen of opslagmaterialen te ontwerpen.

In hoofdstuk 3, hoofdstuk 4 en het eerste deel van hoofdstuk 5 worden modellen die elektroneninvangst- en elektronenvrijkomstprocessen beschrijven in detail bediscussieerd. In deze hoofdstukken is Ce^{3+} het recombinatiecentrum, terwijl de andere lanthanide-codoteringen (zoals: Pr^{3+}, Er^{3+}, Nd^{3+}, Ho^{3+}, Dy^{3+} en Tm^{3+}) fungeren als elektroneninvangstcentra. Voor elke lanthanide-codotering is er een andere valdiepte.

In dit model is de positie van de bodern vande geleidingsband cruciaal voor nagloeiverschijnselen. Voor $Sr_3Al_xSi_{1-x}O_5{:}Ce^{3+},Dy^{3+}$ (hoofdstuk 3) ligt de bodern vande geleidingsband te ver boven de Ce^{3+} $5d_1$ geëxciteerde toestand. Hierdoor kan de thermische ionisatie van het Ce^{3+} $5d_1$ elektron in de geëxciteerde toestand niet plaatsvinden bij kamer temperatuur. Enkel de elektronen in de hogere 5d geëxciteerde toestanden van Ce^{3+} kunnen geïoniseerd worden naar de geleidingsband en daarmee de elektronvallen vullen. Het materiaal kan dan dus enkel opgeladen worden met UV-licht bij kamertemperatuur. Anderzijds, $(Sr, Ca)_3(Y, Lu)_2Ge_3O_{12}{:}Ce^{3+}$ (hoofdstuk 4) heeft een te laag liggende geleidingsband. Derhalve liggen het merendeel van de laagste divalente lanthanide $4f^n$-niveaus in de geleidingsband. Enkel Sm^{3+} geeft als codotering een thermoluminescentie-gloei (TL-gloei). Dit terwijl andere lanthanide-codoteringen óf geen elektron kunnen invangen óf het elektron te diep invangen waardoor de recombinatieluminescentie op Ce^{3+} zal uitdoven.

Het "gateninvangst-en-vrijkomst-model" wordt uitvoerig behandeld in hoofdstuk 5 en 6 en het is de eerste keer dat dit model onderzocht en bevestigd is.

Hoofdstuk 5 laat zien dat: (1) Ce^{3+}, Pr^{3+} en Tb^{3+} als gateninvangstcentra kunnen dienen, terwijl Sm^{3+}, Eu^{3+} en Yb^{3+} als recombinatiecentra dienen in

GdAlO$_3$:Ln^{3+},RE^{3+} (Ln=Sm, Eu en Yb, RE=Ce, Pr en Tb); (2) tijdens de uitlezing van de TL meting komen de gaten eerder vrij dan de elektronen, wat leidt tot de karakteristieke 4f-4f emissie van Sm^{3+}, Eu^{3+} en Yb^{3+}; (3) de diepte van Tb^{4+}- en Pr^{4+}- gerelateerde gateninvangstcentra kan worden aangepast door middel van valentieband-aanpassing; (4) de gateninvangstcentra in LaAlO$_3$:Eu^{3+},Tb^{3+} kunnen worden gevuld met behulp van de Eu^{3+} ladingsoverdrachtexcitatie-energie.

De resultaten uit hoofdstuk 5 gaven ons een nieuw idee om een nagloeifosfor te ontwikkelen gebaseerd op het model van gaten invangen en loslaten, in plaats van het meer gebruikelijke elektroneninvangst- en elektronenvrijkomstmodel. De overeenkomst tussen de Eu^{3+} TLE- en PLE-spectra van LaAlO$_3$:Eu^{3+},Tb^{3+} leveren het bewijs dat we hier te maken hebben met het type gatentransport. Dit inspireerde ons om Eu^{3+} te gebruiken als gatenrecombinatiecentrum om zo efficiënte rode emissie te genereren. Om daglicht te absorberen, moet de TLE opgeschoven worden naar golflengtes langer dan 300-350 nm, waardoor de Eu^{3+} ladingsoverdrachtexcitatie bij relatief lage energie komt te liggen wat dus aangeeft dat het materiaal een hoog gelegen valentieband (VB) moet hebben.

In hoofdstuk 6 hebben we het bovenstaande idee bevestigd door het nagloeimechanisme van Y$_2$O$_2$S:Eu^{3+},Ti^{4+} te bestuderen. Het VRBE-diagram laat zien dat Y$_2$O$_2$S een relatief hoog gelegen VB heeft, met de top van de VB op ongeveer -7.5 eV t.o.v het vacuumniveau, wat de relatief lage CT excitatie-energie van Eu^{3+} en Ti^{4+} verklaart. De TL metingen tonen aan dat Ti^{4+} en Eu^{3+} fungeren als elektroneninvangst- en gatenrecombinatiecentra, terwijl intrinsieke defecten in het gastrooster zich als gateninvangstcentra gedragen. De TLE-spectra voor iedere RE$_2$O$_2$S, enkelvoudig gedoteerd met Eu^{3+} of Ti^{4+}, hebben een brede band welke overeenkomt met ladingsoverdrachtexcitatie van de VB naar Eu^{3+} of Ti^{4+}. Deze ladingsoverdracht laat zien dat dit materiaal door middel van zonlicht opgeladen kan worden. Op basis van bovenstaande informatie concludeerden we dat het nagloeimechanisme van Y$_2$O$_2$S:Eu^{3+},Ti^{4+} een gevolg is voor vrijkomende gaten, in plaats van het meer voorkomende vrijkomen van elektronen.

Acknowledgments

After an exhausting and boring reading of this thesis, here finally comes the most exciting and probably most readable part: the acknowledgements!

Studying and living in the Netherlands is definitely my unforgettable experience. I have been to the Netherlands in the autumn of 2013 and, until now, it has been almost four years. I really don't know where to start because there are so many people that need to be appreciated.

First of all, I would like to thank my supervisor and promotor Prof. Dr. Pieter Dorenbos, who gave me the chance to study at TUDelft and imported me from China to the Netherlands. I really appreciate his guidance and great support during my whole Ph.D. research period that makes me become more and more independent. Also I need to thank for Dr. Adrie Bos. I believe that he was my daily supervisor for the first two years, after that he retired and now he is enjoying his life somewhere. I appreciate his patience for teaching me the principles and operations of the thermoluminescence setups. Except for that, we also had a lot of fruitful discussions about the mechanism behind the thermoluminescence glow curves.

Secondly, I would like to express my gratitude to the formal technician Mr. John Vlieland and the current two technicians in our group: Mr. Johan de Hass and Mr. Aday Josef. Every time I went to their office, they would know something got wrong with the instruments. I can definitely say that without their support of the equipment, I can never finish my Ph.D.

Thirdly, I need to thank Dr. Anna Dobrowolska. In the beginning of my Ph.D. research, it was her that taught me how to use the setups and how to analyse the data.

Fourthly, thanks go to Dr. Bert Hintzen. I learned plenty much about the crystallography by discussing with him. Although none of these discussions are presented in my Ph.D. thesis, this knowledge could be used in my future career.

Fifthly, I would like to thank our "coffee table group", which is actually combined of our research group (Section Luminescence Materials) and the Bio-Medical Image group: Beien Wang, Evert Merkx, Roy Awater, Weronika Wolszczak, Yuan Chen, etc. We almost had something interesting and new (sometimes was wired) everyday on the coffee table. That makes the life colourful and at least, not boring. On the other hand, I really improved my spoken English skills from the coffee table, which is much more effective (also much cheaper) than all of the English training schools that I had taken.

Very very special thanks for my girlfriend: Miss. REN. We were classmates before and we have been in love for almost four years, and thank you for waiting for me these years. I love you.

最后，发自内心的感谢我的父母，有道是"父母在不远游，游必有方"。作为你们唯一的儿子我感到很骄傲。我爱你们，爸爸妈妈。

Hongde Luo
September 2017
Delft, the Netherlands

List of Publications

Hongde Luo*, Adrie J. J. Bos, and Pieter Dorenbos
Charge Carrier Trapping Processes in RE_2O_2S (RE = La, Gd, Y, and Lu)
J. Phys. Chem. C, 2017, 121 (16), 8760–8769

Hongde Luo*, Lixin Ning, Yuanyuan Dong, Adrie J. J. Bos, and Pieter Dorenbos
Electronic Structure and Site Occupancy of Lanthanide-Doped $(Sr,Ca)_3(Y, Lu)_2Ge_3O_{12}$ Garnets: A Spectroscopic and First-Principles Study
J. Phys. Chem. C, 2016, 120 (50), 28743–28752

Hongde Luo, Adrie J. J. Bos, and Pieter Dorenbos*
Controlled Electron–Hole Trapping and Detrapping Process in $GdAlO_3$ by Valence Band Engineering
J. Phys. Chem. C, 2016, 120 (11), 5916–5925

Hongde Luo*, Adrie J. J. Bos, Anna Dobrowolska, and Pieter Dorenbos
Low-temperature VUV photoluminescence and thermoluminescence of UV excited afterglow phosphor $Sr_3Al_xSi_{1-x}O_5:Ce^{3+},Ln^{3+}$ (Ln = Er, Nd, Sm, Dy and Tm)
Phys. Chem. Chem. Phys, 2015, 17, 15419-15427

Bart Budde, **Hongde Luo**, Pieter Dorenbos, and Erik van der Kolk*
Luminescent properties and energy level structure of $CaZnOS:Eu^{2+}$
Opt. Mater. 2017, 69, 378-381

Curriculum vitae

Hongde LUO was born on 17 November 1987 in Shanghai, China. In July 2013, he obtained his master degree at the Faculty of Applied Chemistry at Shanghai Normal University in China. His master was concluded with a project on "Phosphors for Solid-State Lighting" under the supervision of Prof. Xibin Yu and Dr. Jie Liu.

After graduation, he came to the Netherlands in the autumn of 2013. He joined the group of Fundamental Aspect of Materials and Energy (FAME) at Delft University of Technology and focused on his research on afterglow phosphors that supervised by Prof. Dr. Pieter Dorenbos and Dr. Adrie J.J. Bos. The results of the research are presented in this thesis.